



AN INVESTIGATION OF CAVITY RESONANCE AND ITS  
RELATIONSHIP TO STORE FORCE AND MOMENT LOADING

THESIS

Christopher J. Coley, Captain, USAF

AFIT/GAE/ENY/11-M05

DEPARTMENT OF THE AIR FORCE  
AIR UNIVERSITY

**AIR FORCE INSTITUTE OF TECHNOLOGY**

Wright-Patterson Air Force Base, Ohio

APPROVED FOR PUBLIC RELEASE; DISTRIBUTION IS UNLIMITED.

The views expressed in this thesis are those of the author and do not reflect the official policy or position of the United States Air Force, Department of Defense, or the United States Government.

This material is declared a work of the U.S. Government and is not subject to copyright protection in the United States.

AFIT/GAE/ENY/11-M05

AN INVESTIGATION OF CAVITY RESONANCE AND ITS  
RELATIONSHIP TO STORE FORCE AND MOMENT LOADING

THESIS

Presented to the Faculty  
Department of Aeronautics and Astronautics  
Graduate School of Engineering and Management  
Air Force Institute of Technology  
Air University  
Air Education and Training Command  
In Partial Fulfillment of the Requirements for the  
Degree of Master of Science in Aeronautical Engineering

Christopher J. Coley, B.S.

Captain, USAF

March 2011

APPROVED FOR PUBLIC RELEASE; DISTRIBUTION IS UNLIMITED.

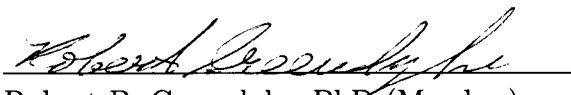
AN INVESTIGATION OF CAVITY RESONANCE AND ITS  
RELATIONSHIP TO STORE FORCE AND MOMENT LOADING

Christopher J. Coley, B.S.  
Captain, USAF

Approved:

  
Maj Andrew J. Lofthouse, PhD (Chairman)

11 Mar 11  
Date

  
Robert B. Greendyke, PhD (Member)

11 Mar 11  
Date

  
Lt Col Richard E. Huffman, PhD (Member)

11 Mar 11  
Date

*Abstract*

A store which is released from an internal bay is subjected to a highly unsteady flowfield which influences the release characteristics for the store. Pressure transducer information is often used to estimate store loading, although no direct correlation between the observed frequencies from the pressure transducers and the store loading has been developed. The relationship between the acoustic modes present in the cavity and the force and moment loading on a store released from a bay are investigated through a CFD study using the OVERFLOW 2.1 solver. The acoustic modes of the cavity are calculated from the pressure fluctuation histories along the cavity ceiling and walls. Empty cavity solutions are compared to the frequencies predicted by the Rossiter equation and to experimental data from the WICS database. Additionally, the cavity pressure fluctuation spectra are compared to the force and moment loading spectra for a store located in the cavity in both the carriage position and the shear layer. It is determined that the presence of a store in the cavity does not alter the fundamental acoustic modes in the cavity. Also, the store force and moment loadings are observed to correlate with the cavity pressure fluctuations.

AFIT/GAE/ENY/11-M05

*To Mom and Dad*

### *Acknowledgements*

First and foremost I would like to thank my advisor, Maj Andrew Lofthouse, for his guidance and support, without which I would have been unable to complete my research. I would also like to thank CDR Neal Kraft for providing insight, acting as a sounding board, and struggling with me in our mutual effort to learn how to use OVERFLOW.

I am particularly grateful to Mr. Shawn Westmoreland and Dr. Robert Nichols, both of whom provided me with grids and other computational tools which aided my research.

I would also like to thank Dr. Scott Sherer, Dr. Robert Tramel, and Dr. Jonathan Dudley, all of whom provided me with assistance at one point or another with questions I had during my research.

Last, but certainly not least, I would like to thank my parents and family for their support and encouragement, and all my friends who provided a necessary balance in my life to counteract the many hours spent working in the lab.

Christopher J. Coley

## *Table of Contents*

|  | Page |
|--|------|
| Abstract . . . . .   | iv   |
| Abstract . . . . .   | v    |
| Acknowledgements . . . . .   | vi   |
| List of Figures . . . . .  | ix   |
| List of Tables . . . . .   | xiv  |
| I. Introduction . . . . .  | 1    |
| II. Background . . . . .   | 5    |
| 2.1 Characterization of Cavity Flow . . . . .                      | 5    |
| 2.2 WICS Program . . . . .   | 8    |
| 2.2.1 WICS Experimental Setup . . . . .                            | 9    |
| 2.2.2 WICS Results . . . . .                                       | 10   |
| 2.3 OVERFLOW 2.1 CFD Solver . . . . .                              | 12   |
| 2.3.1 OVERFLOW 2.1 Capabilities . . . . .                          | 12   |
| 2.3.2 Navier-Stokes Equation Implicit Solution Procedure . . . . . | 13   |
| 2.3.3 Overset Grids . . . . .                                      | 16   |
| 2.4 Signal Processing and Spectral Analysis . . . . .              | 17   |
| III. Methodology . . . . .   | 19   |
| 3.1 Grid Topology and Solver Settings . . . . .                    | 20   |
| 3.2 WICS Cavity Validation . . . . .                               | 27   |
| 3.2.1 Newton Subiteration Study . . . . .                          | 27   |
| 3.2.2 Grid Resolution Study . . . . .                              | 27   |
| 3.2.3 Time Step Sensitivity Study . . . . .                        | 28   |
| 3.3 Cavity with Store in Carriage Configuration . . . . .          | 29   |
| 3.4 Cavity with Store in Shear Configuration . . . . .             | 29   |
| 3.5 Cavity with Store in Forward Shear Configuration . . . . .     | 29   |

|   | Page |
|---|------|
| IV. Results . . . . .   | 30   |
| 4.1 Empty WICS Cavity . . . . .                                     | 30   |
| 4.1.1 Newton Subiteration Study . . . . .                           | 30   |
| 4.1.2 Grid Resolution Study . . . . .                               | 33   |
| 4.1.3 Time Step Sensitivity Study . . . . .                         | 36   |
| 4.1.4 Empty Cavity Validation . . . . .                             | 40   |
| 4.2 Cavity with Store in Carriage Configuration . . . . .           | 49   |
| 4.3 Cavity with Store in Shear Configuration . . . . .              | 64   |
| 4.4 Cavity with Store in Forward Shear Configuration . . . . .      | 80   |
| V. Conclusions . . . . .  | 97   |
| 5.1 Future Work . . . . .   | 99   |
| Appendix A. OVERFLOW Namelist Parameters . . . . .                  | 101  |
| Appendix B. Summary of Computational Expense of Solutions . . . . . | 104  |
| Bibliography . . . . .  | 106  |
| Vita . . . . .  | 108  |

## *List of Figures*

| Figure |   | Page |
|--------|---|------|
| 1.     | Schematic depicting acoustic resonance resulting from grazing cavity flow . . . . .       | 6    |
| 2.     | Depiction of an open cavity . . . . .   | 7    |
| 3.     | Depiction of a closed cavity . . . . .  | 7    |
| 4.     | Top view of plate and cavity setup as mounted in wind tunnel .                            | 10   |
| 5.     | The Hamming Window in the Time Domain . . . . .   | 18   |
| 6.     | Frequency Response of the Hamming Window . . . . .  | 18   |
| 7.     | Depiction of four configurations investigated . . . . .                                   | 20   |
| 8.     | Empty cavity grid system . . . . .  | 21   |
| 9.     | Overhead view of cavity region . . . . .  | 22   |
| 10.    | Location of K12, K16, K17, and K18 transducers on the cavity floor and aft wall . . . . . | 23   |
| 11.    | Location of L01 and L02 pressure probes on the cavity side wall                           | 23   |
| 12.    | Store grid system . . . . .   | 24   |
| 13.    | Cavity with the store in carriage configuration . . . . .                                 | 25   |
| 14.    | Cavity with the store in shear configuration . . . . .                                    | 25   |
| 15.    | Cavity with the store in forward shear configuration . . . . .                            | 25   |
| 16.    | Store pressure probe locations . . . . .  | 26   |
| 17.    | Comparison of three grid resolutions for cavity grid . . . . .                            | 28   |
| 18.    | Newton subiteration sensitivity for the K12 transducer . . . . .                          | 31   |
| 19.    | Newton subiteration sensitivity for the K16 transducer . . . . .                          | 32   |
| 20.    | Newton subiteration sensitivity for the K17 transducer . . . . .                          | 32   |
| 21.    | Newton subiteration sensitivity for the K18 transducer . . . . .                          | 33   |
| 22.    | Grid resolution sensitivity for the K12 transducer . . . . .                              | 34   |
| 23.    | Grid resolution sensitivity for the K16 transducer . . . . .                              | 35   |
| 24.    | Grid resolution sensitivity for the K17 transducer . . . . .                              | 35   |

| Figure |  | Page |
|--------|--|------|
| 25.    | Grid resolution sensitivity for the K18 transducer . . . . .                                     | 36   |
| 26.    | Time step sensitivity for the K12 transducer . . . . .   | 38   |
| 27.    | Time step sensitivity for the K16 transducer . . . . .   | 38   |
| 28.    | Time step sensitivity for the K17 transducer . . . . .   | 39   |
| 29.    | Time step sensitivity for the K18 transducer . . . . .   | 39   |
| 30.    | Pressure time history for K18 transducer location . . . . .                                      | 41   |
| 31.    | Time averaged velocity vectors for the empty cavity (colored by Mach number) . . . . .           | 43   |
| 32.    | SPL spectrum at the K12 transducer location for the empty cavity                                 | 44   |
| 33.    | SPL spectrum at the K16 transducer location for the empty cavity                                 | 44   |
| 34.    | SPL spectrum at the K17 transducer location for the empty cavity                                 | 45   |
| 35.    | SPL spectrum at the K18 transducer location for the empty cavity                                 | 45   |
| 36.    | Pseudo-Schlieren images of empty cavity . . . . .  | 46   |
| 37.    | SPL spectrum at the L01 location for the empty cavity . . . .                                    | 47   |
| 38.    | SPL spectrum at the L02 transducer location for the empty cavity                                 | 48   |
| 39.    | Time averaged velocity vectors for the carriage configuration (colored by Mach number) . . . . . | 50   |
| 40.    | SPL spectrum at the K12 transducer location for the carriage configuration . . . . .             | 51   |
| 41.    | SPL spectrum at the K16 transducer location for the carriage configuration . . . . .             | 52   |
| 42.    | SPL spectrum at the K17 transducer location for the carriage configuration . . . . .             | 52   |
| 43.    | SPL spectrum at the K18 transducer location for the carriage configuration . . . . .             | 53   |
| 44.    | Pseudo-Schlieren images of carriage configuration . . . . .                                      | 54   |
| 45.    | SPL spectrum at the L01 location for the carriage configuration                                  | 55   |
| 46.    | SPL spectrum at the L02 transducer location for the carriage configuration . . . . .             | 55   |

| Figure |  | Page |
|--------|--|------|
| 47.    | Definition of coordinate system . . . . .  | 56   |
| 48.    | Force time history for the store in the carriage configuration . .   | 57   |
| 49.    | Moment time history for the store in the carriage configuration  | 57   |
| 50.    | Pressure coefficient on top and bottom of store in carriage con-<br>figuration . . . . .   | 59   |
| 51.    | Store longitudinal force frequency spectrum (right axis) and K16<br>transducer SPL spectrum (left axis) for carriage configuration . | 60   |
| 52.    | Store vertical force frequency spectrum (right axis) and K16<br>transducer SPL spectrum (left axis) for carriage configuration .     | 61   |
| 53.    | Store pitch moment frequency spectrum (right axis) and K16<br>transducer SPL spectrum (left axis) for carriage configuration .       | 61   |
| 54.    | Store roll moment frequency spectrum (right axis) and K16 trans-<br>ducer SPL spectrum (left axis) for carriage configuration . . .  | 62   |
| 55.    | SPL spectra on store body at $x/L = 0.25$ for carriage configuration   | 63   |
| 56.    | SPL spectra on store body at $x/L = 0.50$ for carriage configuration   | 63   |
| 57.    | SPL spectra on store body at $x/L = 0.75$ for carriage configuration   | 64   |
| 58.    | Time averaged velocity vectors for the shear configuration (col-<br>ored by Mach number) . . . . .                                   | 65   |
| 59.    | SPL spectrum at the K12 transducer location for the shear con-<br>figuration . . . . .   | 66   |
| 60.    | SPL spectrum at the K16 transducer location for the shear con-<br>figuration . . . . .   | 67   |
| 61.    | SPL spectrum at the K17 transducer location for the shear con-<br>figuration . . . . .   | 67   |
| 62.    | SPL spectrum at the K18 transducer location for the shear con-<br>figuration . . . . .   | 68   |
| 63.    | Pseudo-Schlieren images of shear configuration . . . . .   | 69   |
| 64.    | SPL spectrum at the L01 location for the shear configuration .   | 70   |
| 65.    | SPL spectrum at the L02 transducer location for the shear con-<br>figuration . . . . .   | 70   |

| Figure |  | Page |
|--------|--|------|
| 66.    | Force time history for the store in the shear configuration . . . . .  | 71   |
| 67.    | Moment time history for the store in the shear configuration . . . . .   | 72   |
| 68.    | Pressure coefficient on top and bottom of store in shear configuration . . . . .   | 73   |
| 69.    | Store longitudinal force frequency spectrum (right axis) and K16 transducer SPL spectrum (left axis) for shear configuration . . . . . | 75   |
| 70.    | Store vertical force frequency spectrum (right axis) and K16 transducer SPL spectrum (left axis) for shear configuration . . . . .     | 76   |
| 71.    | Store pitch moment frequency spectrum (right axis) and K16 transducer SPL spectrum (left axis) for shear configuration . . . . .       | 76   |
| 72.    | Store roll moment frequency spectrum (right axis) and K16 transducer SPL spectrum (left axis) for shear configuration . . . . .        | 77   |
| 73.    | SPL spectra on store body at $x/L = 0.25$ for shear configuration  | 78   |
| 74.    | SPL spectra on store body at $x/L = 0.50$ for shear configuration  | 78   |
| 75.    | SPL spectra on store body at $x/L = 0.75$ for shear configuration  | 79   |
| 76.    | Time averaged velocity vectors for the forward shear configuration (colored by Mach number) . . . . .                                  | 80   |
| 77.    | SPL spectrum at the K12 transducer location for the forward shear configuration . . . . .  | 82   |
| 78.    | SPL spectrum at the K16 transducer location for the forward shear configuration . . . . .  | 82   |
| 79.    | SPL spectrum at the K17 transducer location for the forward shear configuration . . . . .  | 83   |
| 80.    | SPL spectrum at the K18 transducer location for the forward shear configuration . . . . .  | 83   |
| 81.    | Pseudo-Schlieren images of forward shear configuration . . . . .   | 85   |
| 82.    | SPL spectrum at the L01 location for the forward shear configuration . . . . .   | 86   |
| 83.    | SPL spectrum at the L02 transducer location for the forward shear configuration . . . . .  | 86   |
| 84.    | Force time history for the store in the forward shear configuration  | 87   |

| Figure |  | Page |
|--------|--|------|
| 85.    | Moment time history for the store in the forward shear configuration . . . . .   | 88   |
| 86.    | Pressure coefficient on top and bottom of store in forward shear configuration . . . . .   | 89   |
| 87.    | Store longitudinal force frequency spectrum (right axis) and K16 transducer SPL spectrum (left axis) for forward shear configuration . . . . . | 91   |
| 88.    | Store vertical force frequency spectrum (right axis) and K16 transducer SPL spectrum (left axis) for forward shear configuration . . . . .     | 92   |
| 89.    | Store pitch moment frequency spectrum (right axis) and K16 transducer SPL spectrum (left axis) for forward shear configuration . . . . .       | 92   |
| 90.    | Store roll moment frequency spectrum (right axis) and K16 transducer SPL spectrum (left axis) for forward shear configuration . . . . .        | 93   |
| 91.    | SPL spectra on store body at $x/L = 0.25$ for forward shear configuration . . . . .  | 94   |
| 92.    | SPL spectra on store body at $x/L = 0.50$ for forward shear configuration . . . . .  | 95   |
| 93.    | SPL spectra on store body at $x/L = 0.75$ for forward shear configuration . . . . .  | 95   |

## *List of Tables*

| Table |  | Page |
|-------|--|------|
| 1.    | Nominal flow conditions for WICS $M = 0.95$ tests . . . . .  | 10   |
| 2.    | Comparison of predicted and measured modal frequencies from the WICS test program . . . . .                                  | 11   |
| 3.    | Location of Pressure Probes . . . . .  | 23   |
| 4.    | Location of Store in Carriage, Shear, and Forward Shear Configurations . . . . .   | 24   |
| 5.    | Parameters for Grid Refinement Study of WICS Cavity . . . . .  | 28   |
| 6.    | Mean pressure and standard deviation for each data partition at each transducer location . . . . .                           | 42   |
| 7.    | Summary of store forces and moments in carriage configuration  | 58   |
| 8.    | Average pressure differential, center of pressure, and center of mass for the store in carriage configuration . . . . .      | 59   |
| 9.    | Summary of store forces and moments in shear configuration .   | 72   |
| 10.   | Average pressure differential, center of pressure, and center of mass for the store in shear configuration . . . . .         | 73   |
| 11.   | Comparison of store forces and moments between carriage and shear configurations . . . . .                                   | 74   |
| 12.   | Summary of store forces and moments in forward shear configuration . . . . .   | 88   |
| 13.   | Average pressure differential, center of pressure, and center of mass for the store in forward shear configuration . . . . . | 90   |
| 14.   | Comparison of store forces and moments between shear configurations . . . . .  | 90   |
| 15.   | Summary of Global OVERFLOW (\$GLOBAL) inputs . . . . .   | 101  |
| 16.   | Summary of Global OVERFLOW-D (\$OMIGLB) inputs . . . .   | 101  |
| 17.   | Summary of OVERFLOW DCF (\$DCFGLB) inputs . . . . .  | 101  |
| 18.   | Summary of load balance (\$GROUPS) inputs . . . . .  | 102  |

| Table |  | Page |
|-------|--|------|
| 19.   | Summary of flow parameter (\$FLOINP) inputs . . . . .                          | 102  |
| 20.   | Summary of numerical method selection (\$METPRM) inputs .                      | 102  |
| 21.   | Summary of time accuracy (\$TIMACU) inputs . . . . .                           | 102  |
| 22.   | Summary of smoothing parameter (\$SMOACU) inputs . . . .                       | 102  |
| 23.   | Summary of viscous and turbulence modeling (\$VISINP) inputs                   | 103  |
| 24.   | Computational Cost of Cavity Simulations . . . . .                             | 104  |
| 25.   | Comparison of Computational Cost for Varying Number of Subiterations . . . . . | 104  |
| 26.   | Comparison of Computational Cost for Grid Resolution Study                     | 105  |
| 27.   | Comparison of Computational Cost for Time Step Sensitivity Study . . . . .     | 105  |

# AN INVESTIGATION OF CAVITY RESONANCE AND ITS RELATIONSHIP TO STORE FORCE AND MOMENT LOADING

## I. Introduction

Cavity flows have been the subject of many studies since the 1950s [1]. The grazing flow over cavities is relevant to a wide range of real-world applications, from gas transport systems to the sunroofs of automobiles. The characteristics of cavity flow is an area of interest to the Air Force because it also describes the flow phenomenon experienced in the region of an aircraft weapons bay.

Although the airflow around an aircraft is unsteady, historic practice has been to use quasi-steady techniques wherein the aerodynamic loading on the store are time-averaged. These techniques capture the mean properties of the airflow but neglect the time-varying fluctuations in the flow. Due to the demonstrated success and repeatability of this methodology for externally-carried stores, it has long been accepted that the release of an externally-carried store can be considered a steady-state problem [2]. This assumption does not necessarily apply, however, for the release of internally-carried stores. For aircraft with weapon bays, a shear layer develops across the opening of the cavity. The interaction of the shear layer and its reattachment at the aft wall of the cavity produces acoustic waves which lead to highly turbulent flow in the cavity and shear layer. The influence of the unsteady flow produces unsteady aerodynamic forces on a store being released from the cavity, possibly affecting the trajectory of the store. It has been shown that this unsteady airflow can influence the separation of a store such that differing trajectories can result at different release times, even when all other flight conditions remain constant [3, 4].

Today's and tomorrow's military aircraft are being designed with an increased emphasis on low-observability. This design goal has led designers to resort to internal carriage of weapons in order to reduce radar cross-section. Although internal carriage

of weapons and their release from a bay is nothing new, the increasing shift to smaller, lighter munitions and ranged weapons has introduced a new challenge to the aircraft-store compatibility engineer. Previous weapons were typically larger and heavier and had high moments of inertia that rendered them relatively insensitive to the fluctuating flow present in the region of a weapon bay. Additionally, it was common practice to use high ejector forces in order to release the store at high velocities, minimizing the store's time in the turbulent flow and, thus, minimizing the impact on the trajectory. Modern weapons are more sensitive than previous weapons to the aerodynamic loads they experience as they are released from the aircraft for several reasons [4]:

- Smaller, lighter stores have less inertia and are therefore influenced more by fluctuating aerodynamic loads
- Modern stores are designed to be inherently less stable in order to increase maneuverability
- Stores have relatively larger control surfaces than before, making them more susceptible to the unsteady flow environment
- Many modern stores have non-circular cross-sections, which can induce rolling moments
- The use of active seeker heads and guidance systems lead to attitude constraints and dynamic limits during separation
- Sensitive equipment on board modern weapons oftentimes limit the magnitude of ejector forces that can be used.

Much of the early research in the area of cavity flows focused on the acoustic modes as it related to structural fatigue in the weapon bay. Suppression devices were developed as a result which served to quell the turbulent airflow and hence the vibrations in the bay. As these devices quieted the airflow in the bay, they also served a role in improving store separation characteristics and predictability. Passive and open-loop active suppression devices do not require knowledge of the flow characteristics,

but closed-loop active suppression devices require the measurement or estimation of some flow quantity [1]. As such, an understanding of the acoustic response to cavity flow is necessary in order to design these devices.

In 1970, the Air Force Flight Dynamics Laboratory (AFFDL) conducted a comprehensive wind tunnel test program in order to characterize the aeroacoustic response of cavities both with and without stores present [5]. From this study it was demonstrated that the presence of a relatively small store in a cavity does not greatly affect the vibrational modes observed in the cavity, although this study did observe that a store located in the shear layer close to the leading edge acted as a sort of suppression device. This study looked only at the pressure fluctuations in the cavity and did not look at the aerodynamic forces nor moments on the store. From September 1986 through September 1990, Arnold Engineering Development Center (AEDC), under the Weapons Internal Carriage and Separation program (WICS), developed an aerodynamic database for internal store carriage and jettison [6]. This study characterized pressure fluctuations in cavities of various geometries and took time-averaged store forces and moments for several stores, but did not correlate cavity pressure fluctuations with unsteady loading on the stores.

Current aircraft/store compatibility methodology utilizes time-averaged store forces and moments and flowfield data with a 6-degree of freedom (6-DOF) analysis in order to simulate expected trajectories. The data can come either from wind-tunnel testing or from computational fluid dynamics (CFD). The results from this analysis dictate which release points are conducted in flight test. It is therefore crucial that the analysis can accurately predict the separation characteristics of a store in order to minimize cost of the flight test program and to ensure aircrew safety during flight testing. This requirement drives the need to develop a time-accurate predictive capability for the analysis of cavity-released stores. In doing so, it is important to understand the relationship between the characteristics of the airflow and the resultant trajectories. While it has been assumed that cavity pressure fluctuations correspond to store force and moment loading variations, no direct correlation has been developed.

If it can be determined that there is a known correlation between the vibrational frequencies demonstrated in an empty cavity and the forces and moments on a store in that cavity, then a better predictive capability for store separation analysis can be developed.

The objective of the present research is to develop a greater understanding of the role that the acoustic modes present in a cavity flow have on the aerodynamic forces and moments imposed upon a store released from that cavity. A CFD study is conducted which correlates the cavity unsteady pressure data with store unsteady force and moment loading. The time-accurate solutions for an empty cavity, a cavity with a weapon in the carriage position, and a weapon located in the shear layer are investigated. A generic cavity with a length-to-depth ratio of  $L/D = 4.5$  and a generic weapon are utilized in the study in order to allow for validation with data from the WICS database. The flight condition is  $M = 0.95$ , which represents a typical worst-case point within the flight release envelope. The vibrational modes present in the empty cavity are compared to those in the two cases with the weapon present and with the aerodynamic forces and moments on the body of the store in both cases.

The introduction has laid the framework of this research and the motivation behind it. Chapter II provides background on the physics of the cavity flow phenomenon as well as an overview of previous cavity flow research. This chapter also describes the OVERFLOW solver, which is used in the current research. Chapter III describes the methodology used in this research, detailing the configurations which are examined. Results are located in Chapter IV. Lastly, Chapter V is composed of the conclusions and recommendations for future work.

## II. Background

The present work seeks to correlate the pressure measurements found in cavity flow to the unsteady weapon loads imposed upon a store located in a cavity. A general characterization of cavity flow is provided and a description of the WICS wind tunnel test and its relevant findings are summarized. The OVERFLOW 2.1 solver, which is used to calculate the solutions for this work, is described and its main features outlined. Finally, a brief overview of signal processing, along with a few considerations regarding spectral analysis, are presented.

### 2.1 *Characterization of Cavity Flow*

The grazing flow past a cavity has been studied with great interest as it has applications in areas including, but not limited to automotive components, gas transport systems, and aeronautical systems. The underlying issue of concern is the occurrence of high amplitude pressure oscillations as they lead to unsteady loading on the components within or near the cavity or unwanted levels of noise in the cavity.

A shear layer is produced above the cavity opening when the approaching boundary layer separates at the leading edge of the cavity. The cavity flow is then characterized by the shear layer behavior. Rockwell and Naudascher [7] identified three flow regimes which they labeled fluid-dynamic interactions, fluid-resonant interactions, and fluid-elastic interactions. The fluid-dynamic regime involves shear-layer instability amplification due to feedback with interaction of the shear layer with the aft cavity wall. This phenomenon is depicted in Fig. 1. This interaction is typical in low-speed flow past shallow cavities. The fluid-resonant regime couples the acoustic modes of the cavity and the shear layer over the cavity. In this regime, the cavity oscillations are strongly coupled with wave effects in the cavity. This regime occurs when the frequencies are high enough that the acoustic wavelength is on the order of or smaller than the cavity characteristic length [7]. This interaction is typical in deeper cavities and cavities located in high Mach number flow. The fluid-elastic

regime encompasses flows that are affected by the elastic boundaries of the cavity and are typically encountered when one part of the cavity is being actuated.

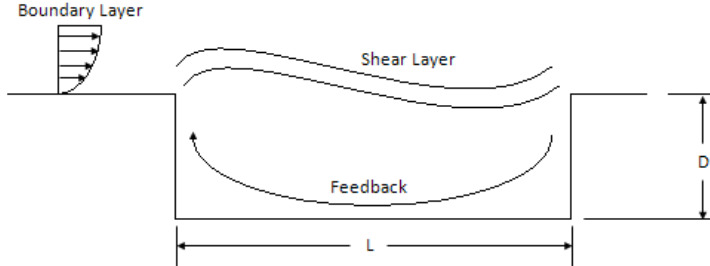


Figure 1: Schematic depicting acoustic resonance resulting from grazing cavity flow

Cavities are typically defined as shallow or deep based on their length-to-depth ratio ( $L/D$ ). Rossiter [8] defines shallow cavities as those having  $L/D > 4$  and deep cavities as those having  $L/D < 4$ , although these definitions are not universal.

At low speeds, the cavity flow can be described as being in the shear-layer mode or wake mode [9]. The shear-layer mode occurs when the shear layer spans the opening of the cavity and stagnates at the aft wall. A cavity in this mode is also known as an *open* cavity. In this classification, the flow can experience both fluid-dynamic and fluid-resonant interactions. The wake mode occurs when the shear layer stagnates somewhere prior to the aft wall (e.g. reattachment with the cavity base). A cavity in this mode is also known as a *closed* cavity. For supersonic flows there can also be interim conditions which are known as *transitionally open* and *transitionally closed*. The two different types of cavity flow are depicted in Figs. 2 and 3. Initially the cut-off between an open and a closed cavity were thought to be determined by the length-to-depth ratio alone. However, various sources throughout the literature cite different values of  $L/D$  as the cut-off between open and closed, for instance:  $L/D < 10$  for open and  $L/D > 13$  for closed [10],  $L/D < 9$  for open and  $L/D > 13$  for closed [11],  $L/D < 3$  for open and  $L/D > 10$  for closed [12]. It is believed that these discrepancies are due to the freestream Mach number and boundary layer thickness, in addition to  $L/D$ , affecting the observed mode [9].

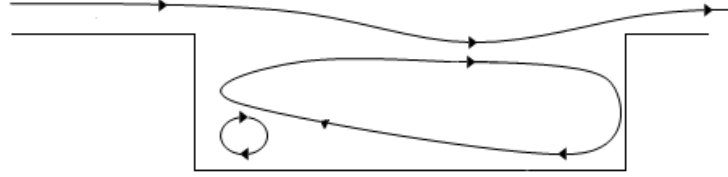


Figure 2: Depiction of an open cavity

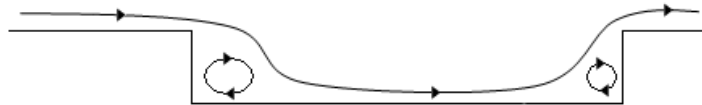


Figure 3: Depiction of a closed cavity

For open cavities, the frequencies of oscillation can be predicted using empirical formulae. For speeds of  $M > 0.4$ , the frequencies can be approximated by the Rossiter equation [8]:

$$f = \frac{U}{L} \frac{m - \alpha}{\frac{1}{\kappa} + M}, \quad (1)$$

where  $U$  is the freestream velocity,  $m$  is the mode number, and Rossiter defined  $\alpha$  and  $\kappa$  experimentally as 0.25 and 0.57, respectively. Note that Eq. (1) only considers longitudinal modes and is therefore a two-dimensional model. In the two-dimensional model, it is assumed that the stagnating flow at the cavity aft wall is deflected at the same frequency as the vortex shedding at the leading edge (although not in phase). In the three-dimensional case, however, the cavity response is influenced by the geometry of the cavity, the condition of the surfaces of the cavity, the contents of the cavity, and the characteristics of the fluid in the cavity. Coupling of the vortex shedding and fluid response is only approximated by the two-dimensional Rossiter model. While the longitudinal modes dominate the flow, it is plausible that lateral and vertical modes also exist [6]. The Rossiter equation assumes a speed of sound equal to the

freestream speed of sound and as a result produces larger errors as the Mach number increases. Heller, et al. [5] modified the Rossiter equation to provide smaller error as Mach number increases. The modified Rossiter equation is

$$f = \frac{U}{L} \frac{\frac{m-\alpha}{\kappa}}{\frac{M}{\sqrt{1+\frac{\gamma-1}{2}M^2}}}, \quad (2)$$

where  $\gamma$  represents the ratio of specific heats. Note that Eqs. (1) and (2) predict the expected frequencies but give no information regarding the amplitude of these frequencies. Additionally, these equations apply only to open cavities, so it must be known which flow regime is present for the cavity in question. Therefore simulation or experimentation are required to completely determine the characteristics of the flow.

The acoustic frequencies in the bay can be related to the time history of the pressure fluctuations  $P(t)$ . This relationship is accomplished by computing the power spectral density (PSD), which describes how the power of  $P(t)$  is distributed with frequency. The PSD is computed from the Fourier transform of the autocorrelation of  $P(t)$ . From the convolution theorem, it can be defined as the squared modulus of the Fourier transform of  $P(t)$  [13]. It is common to report sound pressure on a logarithmic scale relative to the lowest human audible sound. This logarithmic scale is known as the sound pressure level (SPL). Sound pressure level is related to PSD by the following equation:

$$SPL = 10 \log \left( \frac{PSD}{p_{ref}^2} \right), \quad (3)$$

where  $p_{ref} = 2 \times 10^{-5}$  Pa is the value adopted as the minimum audible sound pressure variation.

## 2.2 WICS Program

Arnold Engineering Development Center conducted a wind-tunnel test program from September 1986 through September 1990 with the intention of developing an

aerodynamic database for use in analysis of internal store carriage and jettison. During the course of this program, aerodynamic forces acting on a series of slender missile configurations were measured with the missiles mounted in a spatial grid of locations in and near a generic cavity in a flat plate. The cavity was equipped with a variety of doors and acoustic suppression devices, such as boundary-layer spoilers and aft-bulkhead ramps. Static and fluctuating pressures acting on the plate and cavity surfaces were also measured. The fluctuating pressures were processed into spectra via Fourier transform techniques, and the resonant modes found in the cavity were determined. The experiments were conducted with a variety of cavity geometries at Mach numbers ranging from 0.60 to 5.04 [6]. The data collected during this program has served as a source by which CFD simulations have been validated. Only the experimental setup and results pertaining to the collection of the pressure fluctuation data for the empty cavity are presented here, as they pertain to the present research.

*2.2.1 WICS Experimental Setup.* The cavity in the experiment was constructed by building an opening 4 in wide by 18 in long into a flat plate 16 in wide by 47 in long. The cavity ceiling could be installed at any of several discrete heights between 0 and 4 in. Only 1.25-, 2-, and 4-in heights were used during the tests, providing cavities of length-to-depth ratios of  $L/D = 14.4$ , 9.0, and 4.5, respectively. Fluctuating pressures were measured with differential transducers at up to 45 locations: 7 on the flat plate and 38 on the walls and ceiling of the cavity. Not all transducers were necessarily used in every test. Data was collected at a rate of 10,000 samples/sec. The test configuration is illustrated in Fig. 4.

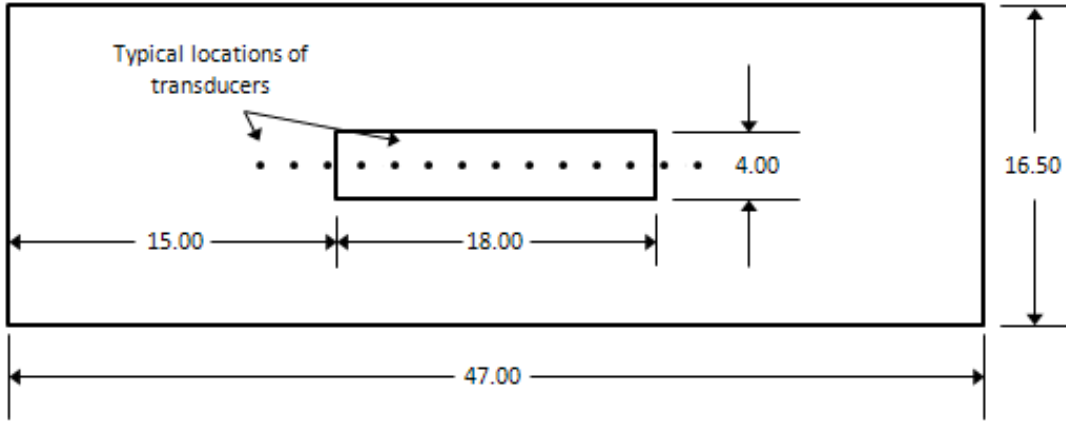


Figure 4: Top view of plate and cavity setup as mounted in wind tunnel

Data were recorded at Mach numbers in the range from 0.60 to 5.04. A nominal unit Reynolds number of  $3 \times 10^6 / ft$  was selected, but unit Reynolds number actually varied during the tests. A full listing of nominal values of the flow conditions can be found in the WICS technical report [6]. The nominal flow conditions for the  $M = 0.95$  cases are listed in Table 1. Note that the case numbering is a convention used here and was not used during the WICS program.

Table 1: Nominal flow conditions for WICS  $M = 0.95$  tests

| Case | $M_\infty$ | $P_t$<br>psf | $T_t$<br>deg R | $V_\infty$<br>ft/sec | $q_\infty$<br>psf | Re<br>1/ft        |
|------|------------|--------------|----------------|----------------------|-------------------|-------------------|
| 1    | 0.95       | 478          | 542            | 998                  | 169               | $1.0 \times 10^6$ |
| 2    | 0.95       | 980          | 545            | 1000                 | 343               | $2.0 \times 10^6$ |
| 3    | 0.95       | 1200         | 550            | 1008                 | 424               | $2.5 \times 10^6$ |
| 4    | 0.95       | 1480         | 551            | 1008                 | 525               | $3.0 \times 10^6$ |

*2.2.2 WICS Results.* Modal frequency predictions for the WICS cavities were made using the modified Rossiter equation with values of  $\alpha$  and  $\kappa$  of 0.28 and 0.56 for the  $L/D = 4.5$  and  $L/D = 9.0$  cavities, respectively. These values were determined during the WICS program to provide superior matching than the values originally posed by Rossiter [6]. Comparisons between the predicted and measured frequencies are presented in Table 2. The modal amplitudes were found to be in the

range of 130 to 170 dB. Note that the  $L/D = 14.4$  cavity is a closed cavity and therefore the modified Rossiter equation does not apply to this case. Additionally, it was reported that no modes were detected during the experiment for this cavity [6]. Of specific note are the results from the  $L/D = 4.5$  cavity at  $M = 0.95$ , since this is the case which is examined in the present research.

Table 2: Comparison of predicted and measured modal frequencies from the WICS test program

| Mach number |      | 0.60  |       | 0.95  |       | 1.20  |       | 1.50  |       | 2.00  |       |
|-------------|------|-------|-------|-------|-------|-------|-------|-------|-------|-------|-------|
| $L/D$       | Mode | Pred. | Meas. |
| 4.5         | 1    | 137   | 137   | 185   | 186   | 210   | 225   | 230   | 244   | 254   | 303   |
|             | 2    | 327   | 352   | 441   | 469   | 502   | 518   | 549   | 586   | 608   | 664   |
|             | 3    | 518   | 547   | 698   | 732   | 794   | 830   | 869   | 938   | 961   | 1,064 |
|             | 4    | 708   | 752   | 954   | 1,016 | 1,087 | 1,025 | 1,188 | 1,152 | 1,314 | 1,436 |
|             | 5    | 898   | 967   | 1,211 | 1,318 | 1,379 | 1,338 | 1,507 | 1,318 | 1,668 | 1,797 |
| 9.0         | 1    | 84    | —     | 113   | —     | 129   | —     | 141   | —     | 155   | —     |
|             | 2    | 274   | 313   | 369   | 400   | 421   | 439   | 460   | 498   | 509   | —     |
|             | 3    | 464   | —     | 626   | 684   | 713   | 762   | 779   | 859   | 862   | 625   |
|             | 4    | 655   | 762   | 883   | 986   | 1,005 | 1,104 | 1,099 | 1,230 | 1,216 | 1,016 |
|             | 5    | 845   | —     | 1,139 | 1,270 | 1,297 | 1,396 | 1,418 | 1,592 | 1,569 | 1,455 |

The results from the WICS experiment have been shown to be reproduceable by CFD simulation. Nichols [14] investigated the flow characteristics of the  $L/D = 4.5$  cavity with  $M = 0.95$  utilizing Detached Eddy Simulation (DES) turbulence models. These solutions were computed using a second-order time, third-order upwind HHLEM [15] space algorithm. These results were in good agreement with the data for the time-averaged pressure, overall sound pressure level, and sound pressure level spectrum. In general, the first four acoustic modes were identifiable in the predictions. In another study, Nichols [16] investigated the ability of Delayed Detached Eddy Simulation (DDES) turbulence models with and without rotation and curvature corrections to accurately predict the flowfield characteristics of both the  $L/D = 4.5$  and  $L/D = 9.0$  cavities. In general, it was found that the DDES simulations provided slightly superior results to those produced by DES, although the rotation and curvature corrections made no significant improvement to the solutions.

## **2.3 OVERFLOW 2.1 CFD Solver**

The present work uses the OVERFLOW 2.1 CFD solver. This code is a three-dimensional time-marching implicit Navier-Stokes code that can also operate in two-dimensional or axi-symmetric mode which utilizes structured overset grids. OVERFLOW 2.1 has several different inviscid flux algorithms and implicit solution algorithms and includes both thin layer and full-viscous terms. The OVERFLOW 2.1 code includes algebraic, one-equation, and two-equation turbulence models, including three DES turbulence models [17]. The code also supports bodies in relative motion and includes a 6-DOF model. Parallelization is possible through both MPI and OpenMP.

*2.3.1 OVERFLOW 2.1 Capabilities.* The following is a partial listing of the capabilities currently included in OVERFLOW 2.1 [18]:

Inviscid flux algorithms:

- 2nd/4th/6th-order central difference with smoothing
- Yee Symmetric TVD
- AUSM+ upwind
- 3rd-order Roe upwind
- 3rd-order HLLC upwind
- 5th-order WENO and WENOM upwind

Implicit solvers:

- ADI Beam-Warming block tridiagonal solver with either central difference or upwind Steger-Warming flux Jacobians
- Steger-Warming 2-factor scheme
- ADI Pulliam-Chaussee scalar pentadiagonal solver
- LU-SGS solver

- D3ADI diagonalized solver
- SSOR solver

Turbulence models:

- Baldwin-Lomax algebraic model with wake model
- Baldwin-Barth 1-equation transport model
- Spalart-Almaras 1-equation transport model
- Spalart-Almaras DES and DDES models
- k- $\omega$  2-equation transport model
- SST 2-equation transport model
- SST DES and SST DDES 2-equation transport models
- SST Multi-Scale (MS) 2-equation transport model
- Wall functions are available for all of the transport turbulence models
- Rotation and curvature corrections are available for the 1- and 2-equation models
- Temperature correction is available for the 2-equation models.

*2.3.2 Navier-Stokes Equation Implicit Solution Procedure.* OVERFLOW 2.1 solves the Navier-Stokes in generalized coordinates. The following treatment is derived from the OVERFLOW 2.1 User's Guide [18]. The Navier-Stokes equations may be written as

$$\frac{\partial \vec{q}}{\partial t} + \frac{\partial \vec{E}}{\partial \xi} + \frac{\partial \vec{F}}{\partial \eta} + \frac{\partial \vec{G}}{\partial \zeta} = 0 \quad (4)$$

where  $q$  is the vector of conserved variables

$$\vec{q} = V \begin{bmatrix} \rho \\ \rho u \\ \rho v \\ \rho w \\ \rho e_0 \end{bmatrix}, \quad (5)$$

where  $V$  represents volume. The linearized Euler implicit form of Eq. (4) including sub-iterations is given by

$$\left[ I + \frac{\Delta t}{(1+\theta)\Delta\tau} + \frac{\Delta t}{1+\theta} (\partial_\xi A + \partial_\eta B + \partial_\zeta C) \right] \Delta q^{n+1,m+1} = \\ - [(q^{n+1,m} - q^n) - \frac{\theta}{1+\theta} \Delta q^n + \frac{\Delta t}{1+\theta} RHS^{n+1,m}]. \quad (6)$$

Here  $\theta = 0$  for first order time differencing and  $\theta = 1/2$  for second order time differencing. An artificial time term  $\left(\frac{\Delta t}{(1+\theta)\Delta\tau}\right)$  has been explicitly added. The pseudo time ( $\Delta\tau$ ) may vary throughout the flow field when a local time step is employed. The artificial time term must converge at each physical time step to assure time accuracy. The explicit viscous and inviscid fluxes are included in the term  $RHS$  given by

$$RHS = \frac{\partial \vec{E}}{\partial \xi} + \frac{\partial \vec{F}}{\partial \eta} + \frac{\partial \vec{G}}{\partial \zeta}. \quad (7)$$

Equation (6) is of the form  $Ax = b$ , where the first bracketed term in (6) is the left hand side matrix  $A$  and the second bracketed term is the vector  $b$ . This system of equations can be solved by inversion of the  $A$  matrix. Direct inversion of the matrix  $A$  requires considerable computational time and memory, so approximations are used to expedite the procedure. Equation (6) can be factored in space as

$$\left[ I + \frac{\Delta t}{1+\theta} \partial_\xi A \right] \left[ I + \frac{\Delta t}{1+\theta} \partial_\eta B \right] \left[ I + \frac{\Delta t}{1+\theta} \partial_\zeta C \right] \Delta q^{n+1,m+1} = \\ - [(q^{n+1,m} - q^n) - \frac{\theta}{1+\theta} \Delta q^n + \frac{\Delta t}{1+\theta} RHS^{n+1,m}] + Error \quad (8)$$

where the factorization error is given by

$$\begin{aligned} \text{Error} = & \left[ \left( \frac{\Delta t}{1+\theta} \right)^2 (\partial_\xi A \partial_\eta B + \partial_\xi A \partial_\zeta C + \partial_\eta B \partial_\zeta C) \right. \\ & \left. + \left( \frac{\Delta t}{1+\theta} \right)^3 (\partial_\xi A \partial_\eta B \partial_\zeta C) \right] \Delta q^{n+1,m+1} \end{aligned} \quad (9)$$

and  $A$ ,  $B$ , and  $C$  are block tridiagonal matrices for structured grids with central difference or first-order spatial upwind implicit flux Jacobians. The  $A$ ,  $B$ , and  $C$  matrices can be decomposed into eigenvalues ( $\Lambda$ ) and eigenvectors ( $X$ ) as

$$\begin{aligned} A &= X_A \Lambda_A X_A^{-1} \\ B &= X_B \Lambda_B X_B^{-1} \\ C &= X_C \Lambda_C X_C^{-1}. \end{aligned} \quad (10)$$

One method to solve the unfactored system of equations in Eq. (6) is to use relaxation procedures. OVERFLOW 2.1 utilizes one such method with the Symmetric Successive Over-Relaxation scheme (SSOR). This scheme can be written as

$$\begin{aligned} \Delta q_{j,k,l}^{mm+1} = & (1 - \Omega) \Delta q_{j,k,l}^{mm} + \Omega \left( \overline{RHS} - \overline{A}_L \Delta q_{j-1,k,l}^{mm-1} - \overline{A}_R \Delta q_{j+1,k,l}^{mm-1} \right. \\ & \left. - \overline{B}_L \Delta q_{j,k-1,l}^{mk1} - \overline{B}_R \Delta q_{j,k+1,l}^{mk2} - \overline{C}_L \Delta q_{j,k,l-1}^{ml1} - \overline{C}_R \Delta q_{j,k,l+1}^{ml2} \right), \end{aligned} \quad (11)$$

where the subscripts  $L$  and  $R$  denote the left and right blocks of the tridiagonal matrices, respectively. The overbar indicates a pre-multiply by the inverse of the diagonal matrix  $A_D + B_D + C_D$  where the subscripts  $D$  denotes the diagonal block of the tridiagonal matrices. The update level of  $\Delta q$  is given by  $mm$ . The scheme uses a forward sweep in  $j$  and symmetric sweeps in  $k$  and  $l$ . For a forward sweep in  $k$  and  $l$ , the updated levels are defined as

$$mk1 = mm + 1, mk2 = mm, ml1 = mm + 1, ml2 = mm. \quad (12)$$

For a backward sweep in  $k$  and  $l$ , the update levels are defined as

$$mk1 = mm, mk2 = mm + 1, ml1 = mm, ml2 = mm + 1. \quad (13)$$

A symmetric sweep consists of a forward and a backward sweep. Multiple symmetric sweeps (typically 10) are performed at each sub-iteration. The relaxation parameter  $\Omega$  is typically set to 0.9.

*2.3.3 Overset Grids.* OVERFLOW 2.1 only supports structured grids. One difficulty that arises from the use of structured grids is in the definition of complex geometry. OVERFLOW 2.1 overcomes this problem through the use of the Chimera, or overset grid, approach. In this approach, the grid system is composed of overlapping structured grids. Various components of the geometry can then be mapped to simple structured grids and each of the components then compiled into one larger grid system. Moving bodies and surfaces can also be easily simulated using overset grids. Here, a background grid or set of grids remain stationary while the grid(s) associated with the moving component(s) are allowed to translate and rotate. The use of overset grids in this case precludes the need to generate a new grid for each time step during the motion.

In an overset grid system, information is passed between grid blocks through interpolation of the flow variables. The overlapping points between which information is passed are known as fringe points and the interpolation between the fringe points must be appropriately weighted. In overset grids it is also possible to define hole points, wherein grid points from one grid might not be used in the solution (e.g. the points of a background grid which reside in the volume of a solid body). Through the Domain Connectivity Function (DCF), OVERFLOW 2.1 processes the grid system and identifies the appropriate hole cutting, definition of fringe points, and grid weighting.

## 2.4 Signal Processing and Spectral Analysis

In order to examine the acoustic modes present in the cavity flow, it is necessary to decompose the pressure time history signal into its constituent frequencies. This decomposition is accomplished through the use of the Fourier transform. The classic Fourier transform is a mathematical operation which decomposes a signal by a basis consisting of sines and cosines [19]. For an infinite, continuous signal  $f(t)$ , the Fourier transform  $F(\omega)$  can be calculated as

$$F(\omega) = \int_{-\infty}^{\infty} f(t) e^{-j\omega t} dt, \quad (14)$$

where  $\omega$  represents frequency,  $t$  denotes time, and  $j$  is defined as  $2\pi i$ .

By necessity, observed signals are finite and discrete. These properties require the use of the discrete Fourier transform (DFT) to process these signals. The processing of finite-duration signals leads to interesting behavior in the spectral analysis. Signals with frequencies other than those of the basis set are not periodic in the observation window, which leads to discontinuities at the boundaries of the observation. The result is that these frequencies lead to non-zero projections across the entire basis set [19]. This phenomenon is known as spectral leakage.

Spectral leakage can be reduced through the use of window functions. Windows are weighting functions applied to the data set in order to reduce the order of the discontinuity at the boundary. The Hamming window is a raised-cosine window designed to minimize side lobe levels. This window is defined as

$$\omega(n) = 0.54 - 0.46 \cos\left(\frac{2\pi}{N}n\right), \quad (15)$$

where  $N$  is the length of the discrete signal and  $n = 0, 1, 2, \dots, N - 1$ . The Hamming window is shown in the time domain in Fig. 5 and in the frequency domain in Fig. 6.

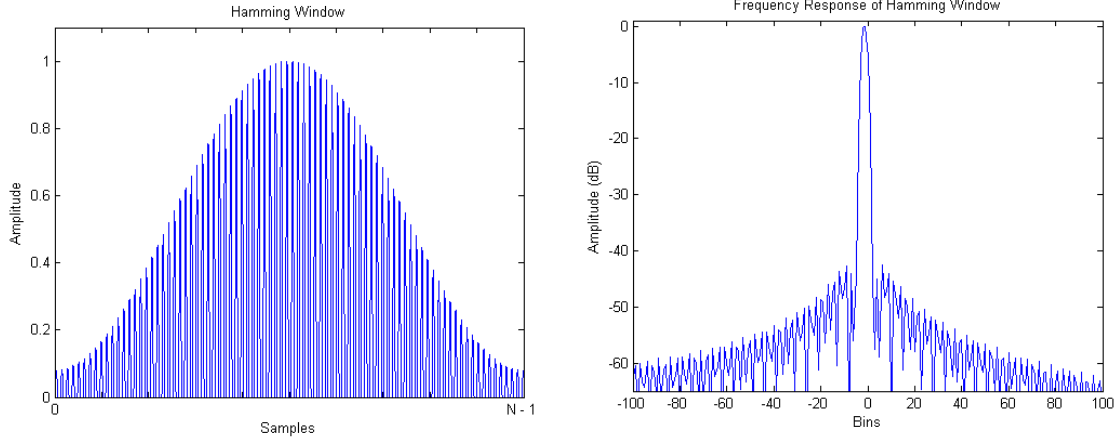


Figure 5: The Hamming Window in the Time Domain

Figure 6: Frequency Response of the Hamming Window

The use of window functions leads to a loss of information near the signal boundaries due to the window having small values in these regions. In order to avoid this loss of data, overlapping partitions can be used. For a fixed signal length, 50% overlap in the partitions is typically used in order to find a balance between minimizing the variation between the partitions and increased computational workload [20]. The Fourier transform of each windowed segment can then be computed and the results averaged to arrive at a final result. This process of partitioning a signal into overlapping segments, windowing each segment, computing the Fourier transform on each segment, and then averaging the values has come to be known as Welch's method [20].

### III. Methodology

A CFD study using the OVERFLOW 2.1 solver is conducted in order to investigate the relationship between acoustic modes in a cavity flow and the aerodynamic forces and moments imposed on a store released from that cavity. The reference case chosen to investigate is a cavity with  $L/D = 4.5$ ,  $M = 0.95$ , and  $Re = 2.5 \times 10^6 ft^{-1}$ . This cavity geometry is selected because it most closely represents the typical geometry of an aircraft weapon bay of the three geometries investigated in the WICS wind-tunnel program. The freestream conditions correspond to Case 3 in Table 1 and represent a worst-case release point.

Four cases are compared: the empty cavity, the cavity with a store in the carriage position, and two configurations of the cavity with a store in the shear layer. These four cases are nominally depicted in Fig. III, where case (a) corresponds to the empty cavity, (b) represents the cavity with the store in carriage position, (c) depicts the cavity with the store in the shear layer directly below the carriage position, and (d) depicts the cavity with the store in the shear layer moved forward towards the leading edge of the cavity. For convenience, these four situations will be referred to as the empty cavity, carriage configuration, shear configuration, and forward shear configuration, respectively. The inclusion of the two shear configurations is to investigate the finding from Heller, et al. [5] that a store located in the shear layer can act as a suppression device if it is sufficiently close to the leading edge of the cavity. This finding is of interest for the current study because if the positioning of the store as it passes through the shear layer affects the cavity dynamics, this can affect the trajectory of the released store.

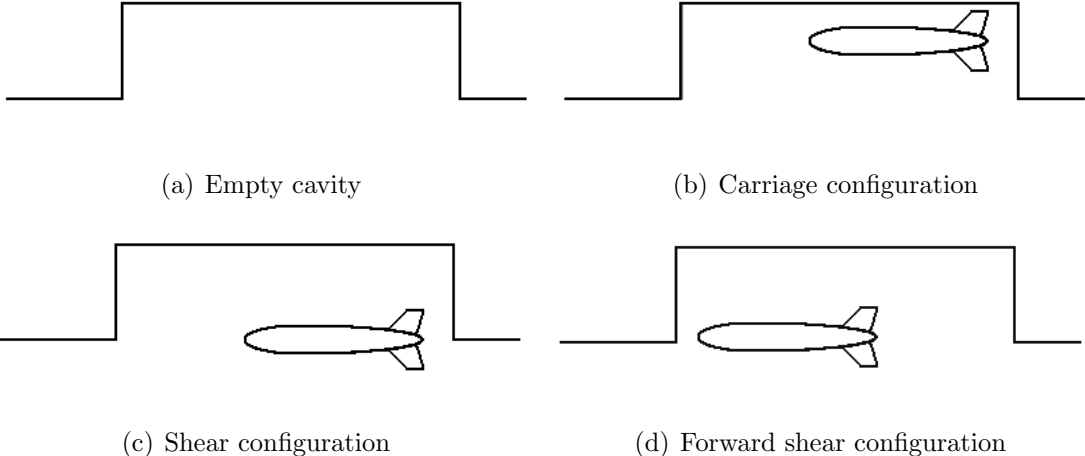


Figure 7: Depiction of four configurations investigated

The time pressure histories at six locations within the cavity are recorded and a spectral analysis conducted on these time histories. Additionally, for the solutions with a store present, time pressure histories at nine locations on the store and store body force and moment coefficients are calculated and a spectral analysis similarly conducted on these data. The longitudinal vibrational modes of the cavity are compared to the results from the WICS wind tunnel test. The CFD derived store pressure, force, and moment data are compared to the predicted cavity vibrational modes from the CFD solutions.

### 3.1 Grid Topology and Solver Settings

The cavity itself is 18 in long by 4 in wide by 4 in deep, matching the dimensions of the WICS cavity. The computational domain extends approximately 45 in ahead of the cavity and 102 in behind. This domain is constructed of 4 separate grids and contains 5.2 million points. The cavity walls are constructed out of one grid while the interior of the cavity is built out of a second grid. This grid extends downward out of the cavity far enough to resolve the shear layer. The cavity grid is 184 x 45 x 90 points, for a total of 745,200 points. The plate which surrounds the cavity, and the volume below this plate, are constructed from a third grid. This grid wraps around the

cavity, leaving a hole in the volume below the cavity. This empty volume necessitates the need for a fourth grid to resolve the volume not captured by the other grids. All bay grids were generated with a wall spacing of  $2 \times 10^{-5}$  inches, resulting in a  $y^+$  on the order of 1. The cavity and store grids were provided by Shawn Westmoreland of Digital Fusion Solutions, Inc., and have been demonstrated to provide accurate results in previous studies [3]. Figure 8 shows the empty cavity grid system. The cavity is represented by the green area (1) and consists of two grids. The blue grid (2) shows the grid which defines the plate which surrounds the cavity. The red grid (3) is the grid which resolves the hole below the cavity which the blue grid does not define. Figure 9 shows a top-down view of the cavity grids. The green grid (1) defines the cavity walls and a short lip around the cavity which mates with the surrounding flat plate. The cavity itself is defined by the black grid (2).

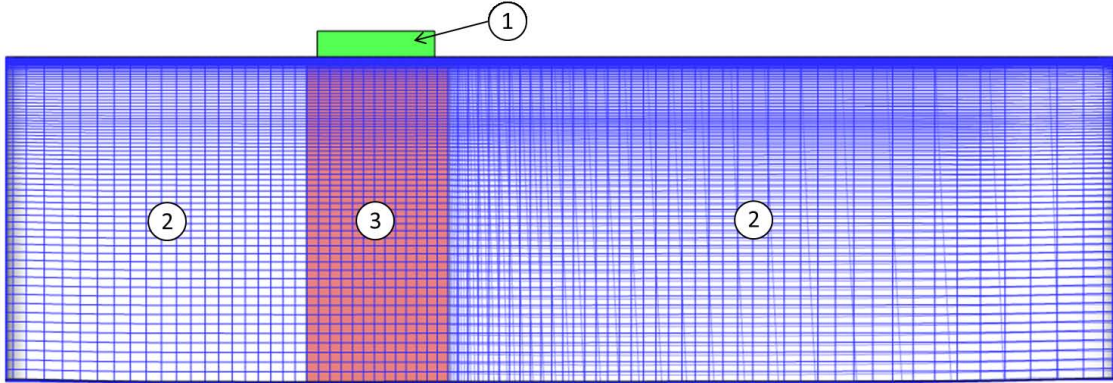


Figure 8: Empty cavity grid system

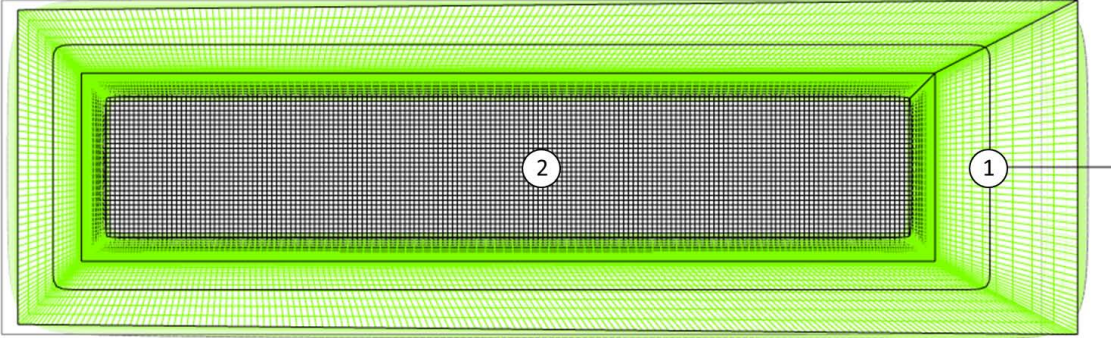


Figure 9: Overhead view of cavity region

Six locations on the cavity ceiling, side wall, and aft wall are designated with the *201* boundary condition in OVERFLOW 2.1, which allows for the time history of the conserved variables at those locations to be recorded. Four of these positions correspond to the K12, K16, K17, and K18 pressure transducers in the WICS wind tunnel test. All of these positions are along the cavity centerline. The K12 and K16 transducers are located on the cavity ceiling and the K17 and K18 transducers are located on the aft wall of the cavity. The K12 transducer corresponds roughly to the center of the cavity and the K16 transducer is nearly at the aft wall. The K17 transducer is roughly located at the mid-height of the aft wall and the K18 transducer is approximately three-quarters height off the ceiling. Two additional positions, L01 and L02, are located 2 in down from the cavity ceiling on the side wall at longitudinal positions which correspond to the K12 and K16 transducer locations, respectively. The pressures at these locations were observed in order to investigate any lateral modes which may be present in the cavity. The pressure probe locations are illustrated in Figs. 10 and 11 and tabulated in Table 3. The pressure histories from these locations are used in the spectral analysis.

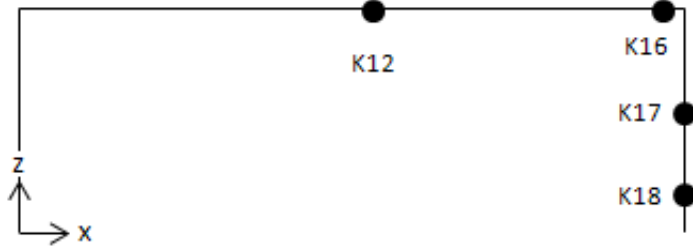


Figure 10: Location of K12, K16, K17, and K18 transducers on the cavity floor and aft wall

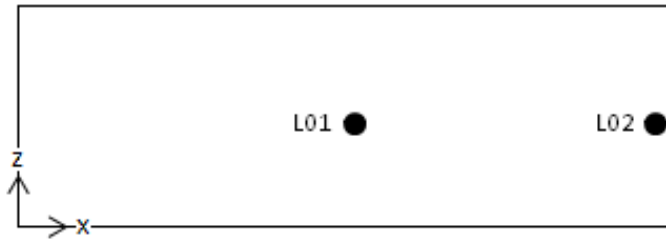


Figure 11: Location of L01 and L02 pressure probes on the cavity side wall

Table 3: Location of Pressure Probes

|     | x (in) | y (in) | z (in) |
|-----|--------|--------|--------|
| K12 | 9.175  | 0.0    | 4.0    |
| K16 | 17.725 | 0.0    | 4.0    |
| K17 | 18.0   | 0      | 1.975  |
| K18 | 18.0   | 0      | 0.725  |
| L01 | 9.175  | 2.0    | 2.0    |
| L02 | 17.725 | 2.0    | 2.0    |

The store of interest is a 1/10th-scale modified Mk-82 class weapon. The overall weapon shape is modelled but detailed features are not included in the model. This is done in order to simplify the work required to grid the store. Since the study seeks to determine the general relationships between the empty cavity flow and flow with a store present, and not a store-specific solution, this compromise is acceptable. The surface and volume meshes for the store are overly dense with the longitudinal grid

spacing never exceeding 0.075 in. Altogether, the store grid system contains 19 grids and consists of 4.3 million grid points. The store grid system is shown in Fig. 12.

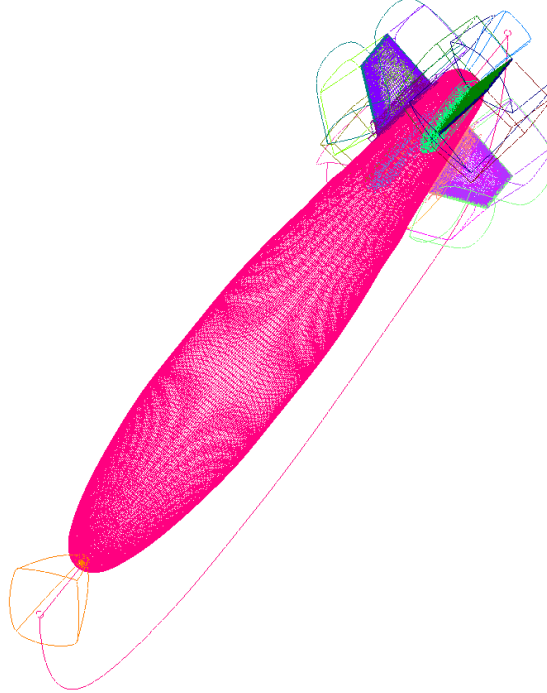


Figure 12: Store grid system

Three cases are run with the store present: the cavity with the store in the carriage position and two configurations with the cavity with the store in the shear layer. The exact positioning of the store in these three locations are presented in Table 4, where the coordinate defines the location of the nose of the store. These three situations are shown in Figs. 13 through 15. The flow direction in Figs. 13 through 15 is from left to right.

Table 4: Location of Store in Carriage, Shear, and Forward Shear Configurations

|                             | x (in) | y (in) | z (in) |
|-----------------------------|--------|--------|--------|
| Carriage Configuration      | 6.0    | 0.0    | 2.2    |
| Shear Configuration         | 6.0    | 0.0    | 0.0    |
| Forward Shear Configuration | 2.0    | 0.0    | 0.0    |

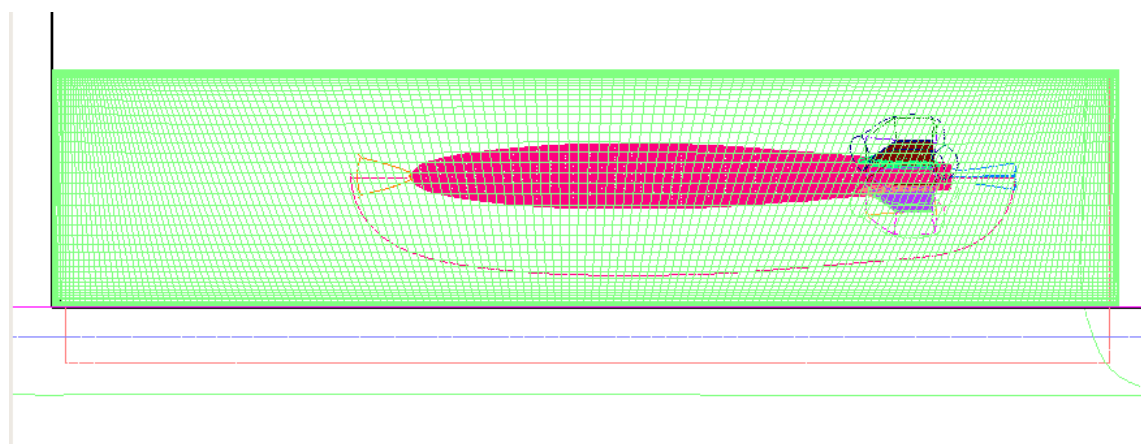


Figure 13: Cavity with the store in carriage configuration

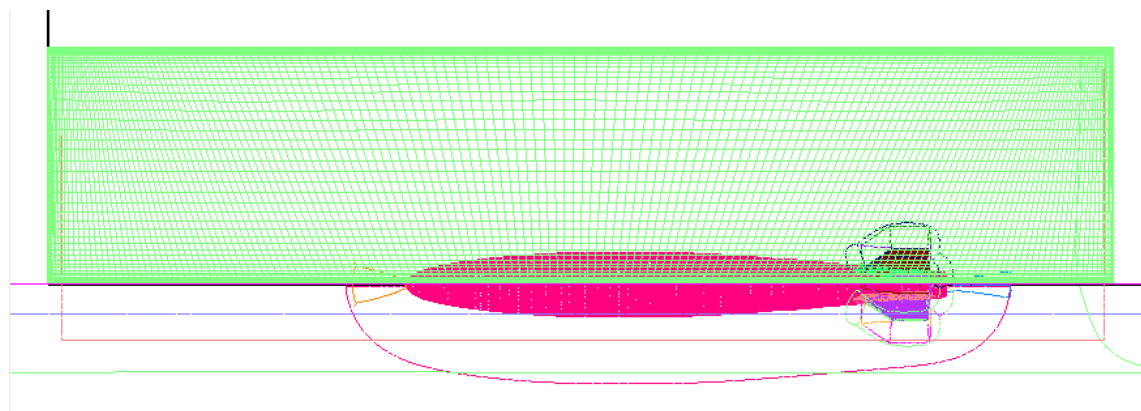


Figure 14: Cavity with the store in shear configuration

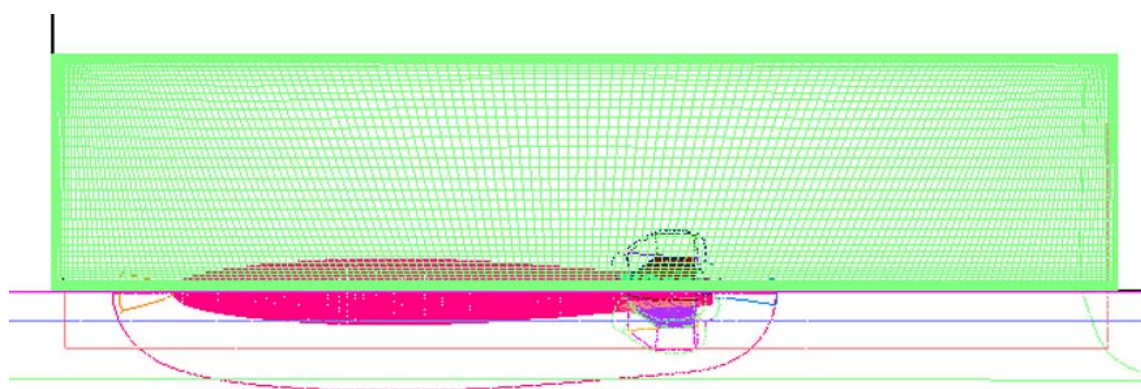


Figure 15: Cavity with the store in forward shear configuration

Since the force and moment data represent the forces and moments acting on the total store, pressure histories are recorded at nine locations on the store in order to provide insight on the contributions to the store forces and moments. Time pressure histories are recorded at the top, side, and bottom of the store at each of three longitudinal positions:  $x/L = 0.25$ ,  $x/L = 0.5$ , and  $x/L = 0.75$ . These positions are shown in Fig. 16.

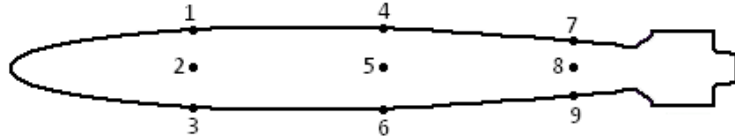


Figure 16: Store pressure probe locations

All solutions are computed in OVERFLOW 2.1 unsteady flow solver. OVERFLOW 2.1 is run using 1st order time with the 5th order spatial upwind Mapped Weighted Essentially Non-Oscillating (WENOM) inviscid flux algorithm. A SSOR procedure is used to solve the unfactored solution matrix. The SST-DDES turbulence model is used. Boundary conditions are established within the domain to simulate a leading plate length of 15 in, corresponding to the WICS experimental setup. A time step of  $dt = 1.6 \times 10^{-5}$  s is used in order to capture the unsteadiness of the flow and five Newton subiterations are used between time steps. Nichols [14] has demonstrated this time step sufficiently resolves the flow structures of interest for this cavity. The choice of Newton subiterations is based upon the result of sensitivity studies, which are discussed further in the discussion of the WICS cavity validation. Grid resolution effects are also investigated.

The calculations are run 10,000 iterations and the final 8,192 time steps are analyzed. Time-averaged data is collected beginning with the 1,000th iteration. This allows the simulation sufficient time for the transients associated with the initialization of the problem to be calculated out of the solution, resulting in a physically realistic solution. At 1,000 iterations, the solution is statistically stationary, which is

shown in the results in Chapter IV. The computational spectral results are computed using Welch's method with 50% overlap and a Hamming window applied to each data set. This technique results in three data sets of 4,096 samples each. The total computational time analyzed is 0.13 s and the time length for each window is 0.066 s. This time period represents about 30 cycles of the predominant 460-Hz frequency in each window.

### ***3.2 WICS Cavity Validation***

A solution for the empty cavity is calculated and validated against the data from the WICS wind tunnel test. This validation is accomplished in order to establish the proper solver settings which are used in this study. Studies are conducted to determine the solution's sensitivity to number of Newton subiterations, grid resolution and selection of time step.

*3.2.1 Newton Subiteration Study.* A Newton subiteration study is conducted to determine the proper number of subiterations necessary to converge the solution at each time step. This study is conducted using the medium grid and a time step of  $1.6 \times 10^{-5}$  s. Solutions are computed using 0, 1, 5, and 10 Newton subiterations and are compared.

*3.2.2 Grid Resolution Study.* A true grid independence study cannot be performed for time-accurate solutions which exhibit turbulent structures because as the grid is refined, the solution will resolve smaller scale turbulent structures. This process will continue until the grid is refined below the Komologrov scales, resulting in a Direct Numerical Simulation (DNS) [14]. Grid resolution effects are studied, however, to ensure that the solution resolves at least the turbulent structures of interest. This study is accomplished by increasing and decreasing the refinement of the cavity grid only. Adjusting only the cavity grid allows for the resolution of the cavity to be adjusted without affecting the wall spacing on the cavity. The details of

the three grids used are presented in Table 5. The centerline plane of the three grids are shown in Fig. 17. The grid resolution study was performed with  $dt = 1.6 \times 10^{-5}$ .

Table 5: Parameters for Grid Refinement Study of WICS Cavity

|        | Total Points | Grid Dimensions | $\Delta x_{max}$ (in) | $\Delta y_{max}$ (in) | $\Delta z_{max}$ (in) |
|--------|--------------|-----------------|-----------------------|-----------------------|-----------------------|
| Coarse | 223,200      | 124 x 30 x 60   | 0.15                  | 0.15                  | 0.30                  |
| Medium | 745,200      | 184 x 45 x 90   | 0.10                  | 0.10                  | 0.20                  |
| Fine   | 2,049,600    | 244 x 70 x 120  | 0.08                  | 0.06                  | 0.15                  |

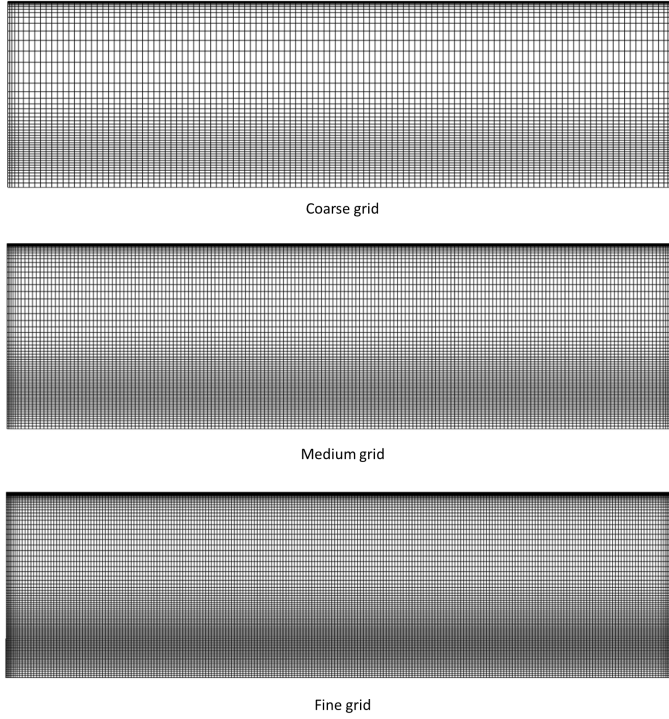


Figure 17: Comparison of three grid resolutions for cavity grid

*3.2.3 Time Step Sensitivity Study.* A time step study is conducted using the medium grid. Three solutions are run with time steps of  $dt = 8.0 \times 10^{-6}$ ,  $dt = 1.6 \times 10^{-5}$ , and  $dt = 4.0 \times 10^{-5}$  s, which correspond to time steps that were investigated by Nichols [14]. The three solutions are compared to the WICS experimental data.

### ***3.3 Cavity with Store in Carriage Configuration***

With the solution for the empty cavity validated, a solution for the cavity with the store in the carriage configuration is computed. This solution is run on the medium grid with  $dt = 1.6 \times 10^{-5}$  s and five Newton subiterations. The location of the store in the carriage configuration is described above.

### ***3.4 Cavity with Store in Shear Configuration***

One solution for the cavity with the store in the shear configuration is computed. This solution is run on the medium grid with  $dt = 1.6 \times 10^{-5}$  s and five Newton subiterations. The location of the store in the shear configuration is described above.

### ***3.5 Cavity with Store in Forward Shear Configuration***

One solution for the cavity with the store in the forward shear configuration is computed. This solution is run on the medium grid with  $dt = 1.6 \times 10^{-5}$  s and five Newton subiterations. The location of the store in the forward shear configuration is described above.

## IV. Results

Several CFD simulations were conducted in order to investigate the cavity acoustic modes and their relation to store and moment loading. First, the simulation setup was validated by running empty cavity solutions and comparing the results to the WICS experimental data. Once a set of inputs were determined which provide an acceptable match between the empty cavity simulation and WICS data, three solutions involving the cavity and a store were computed. For these three solutions, the pressure fluctuations along the cavity ceiling and walls are compared to the force and moment loading and pressure fluctuations on the store. An overview of the computational expense of the main solutions are presented in Table 24 in Appendix B. The results of the empty cavity validation and the three solutions with the store are presented next.

### 4.1 Empty WICS Cavity

The empty cavity solution was first validated against the WICS experimental data. In order to determine the proper simulation parameters, studies investigating the solutions' sensitivity to number of Newton subiterations used, grid resolution, and selection of time step were conducted. The empty cavity solution was computed and compared to the WICS experimental data. Additionally, the sidewall pressure fluctuations were analyzed and compared to those on the cavity ceiling and aft wall in order to investigate the existence of any lateral modes.

*4.1.1 Newton Subiteration Study.* In order to ensure the solution is fully converged at each physical time step, a Newton subiteration study was conducted. Solutions using zero, one, five, and ten Newton subiterations were computed and compared. In OVERFLOW 2.1, specifying zero subiterations calculates the solution once for each time step but allows for the specification of using either a first- or second-order time accurate solution. In this study a first-order time accurate solution was used due to instability with the second-order accurate solution. The solutions were run at a time step of  $dt = 1.6 \times 10^{-5}$  s. The computational expense for each of these solutions are presented in Table 25 in Appendix B.

The SPL spectra for the four cases are shown in Figs. 18 through 21. The dashed lines indicate the frequencies of the first four modes as predicted by the Rossiter equation. The WICS data is plotted in the solid black line. Note that WICS data was not available for the K17 location. The solution shows good prediction of the modal frequencies with at least five Newton subiterations. The solutions between five and ten Newton subiterations do not show a remarkable change in the prediction of the frequencies nor amplitudes of the peaks. From these results, it was decided to use five subiterations for the current research.

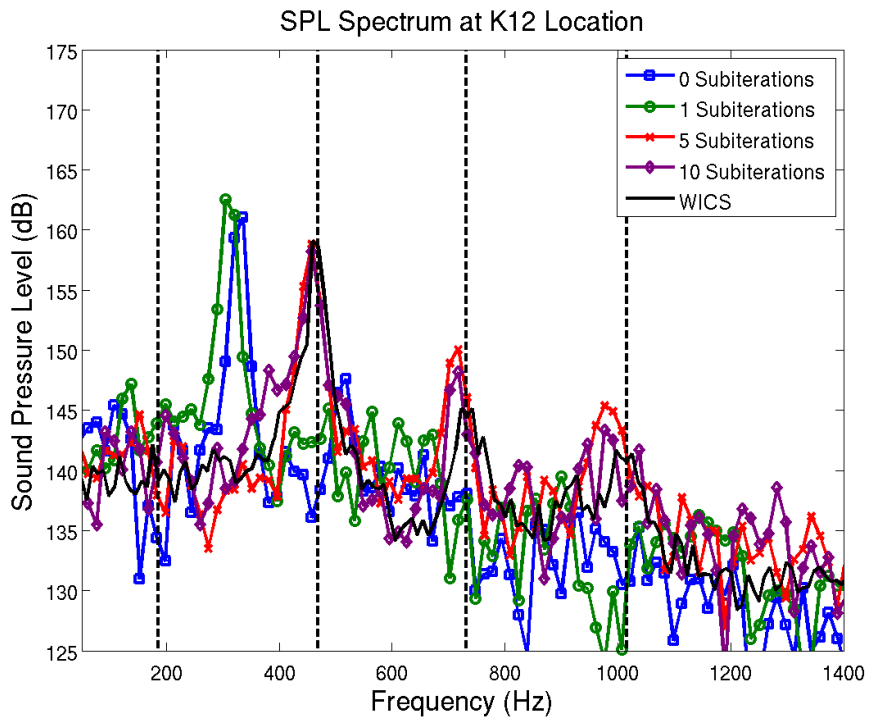


Figure 18: Newton subiteration sensitivity for the K12 transducer

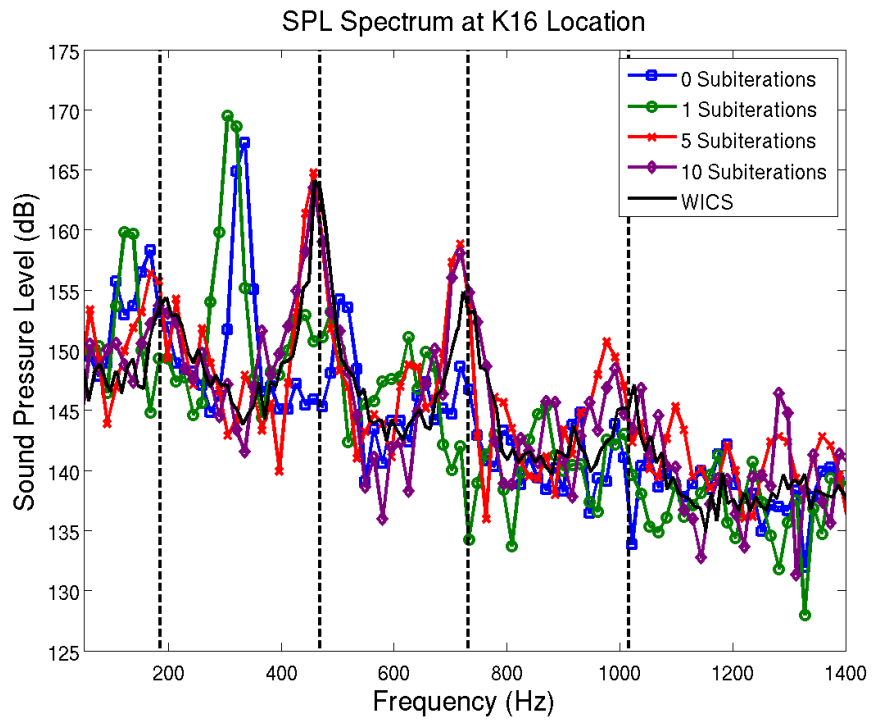


Figure 19: Newton subiteration sensitivity for the K16 transducer

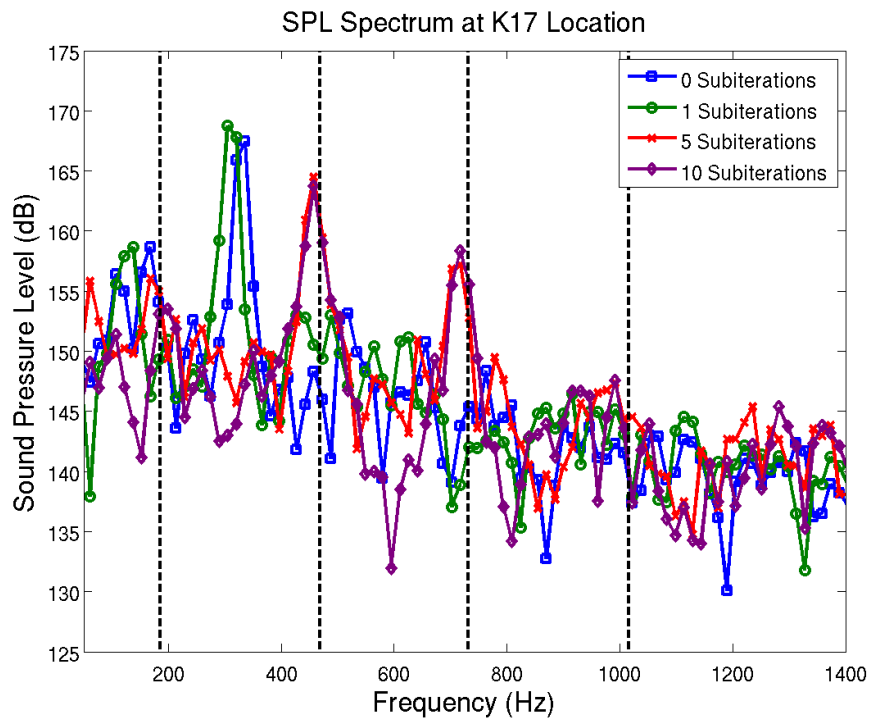


Figure 20: Newton subiteration sensitivity for the K17 transducer

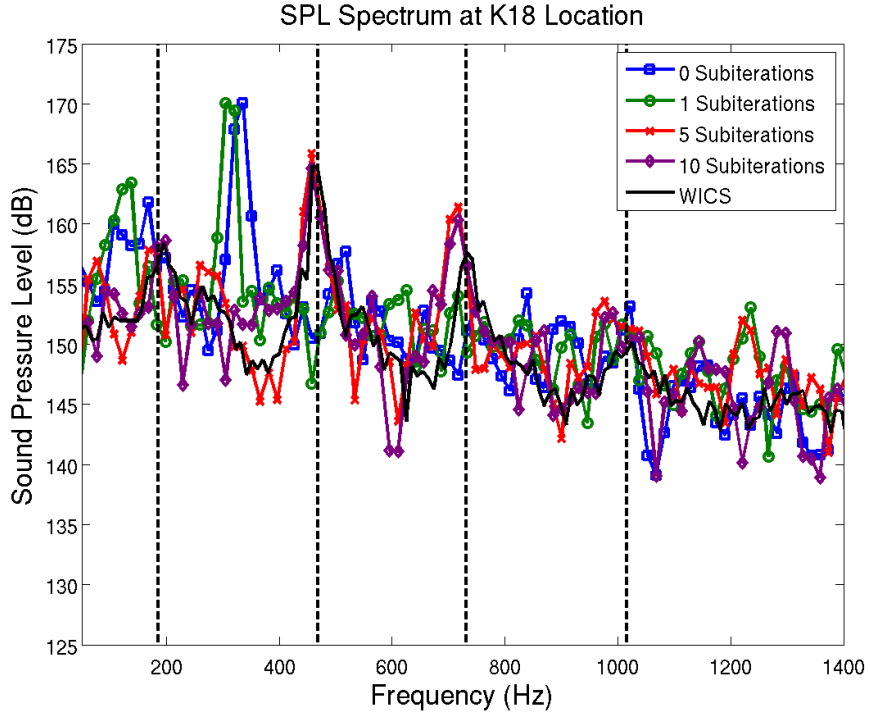


Figure 21: Newton subiteration sensitivity for the K18 transducer

*4.1.2 Grid Resolution Study.* Grid resolution effects were investigated. Three solutions with varying levels of refinement in the cavity grid were computed. The computational expense for each of these solutions are presented in Table 26 in Appendix B.

The sound pressure levels at the four transducer locations for each of the three grids are presented in Figs. 22 through 25. In general, all three grids present the same solution, predicting the frequency of the same frequencies for the first four cavity modes, although the amplitudes do not all agree. There are two notable differences between the grids in the data. First, at the K12 transducer location, the coarse grid over-predicts the overall sound levels, especially at the low frequencies. Secondly, at the K16 transducer location, the fine grid under-predicts the sound levels at low frequencies. It is believed that this is the result of changing the resolution of only the cavity grid affecting the matching of cell sizes at the boundaries between grids. The medium grid agrees in overall sound levels at all locations. From these data, it

is clear that all three grids are refined sufficiently to resolve the turbulent scales of interest. Due to the good agreement of sound levels across all transducer locations, the medium grid provides the best solution for the WICS cavity validation.

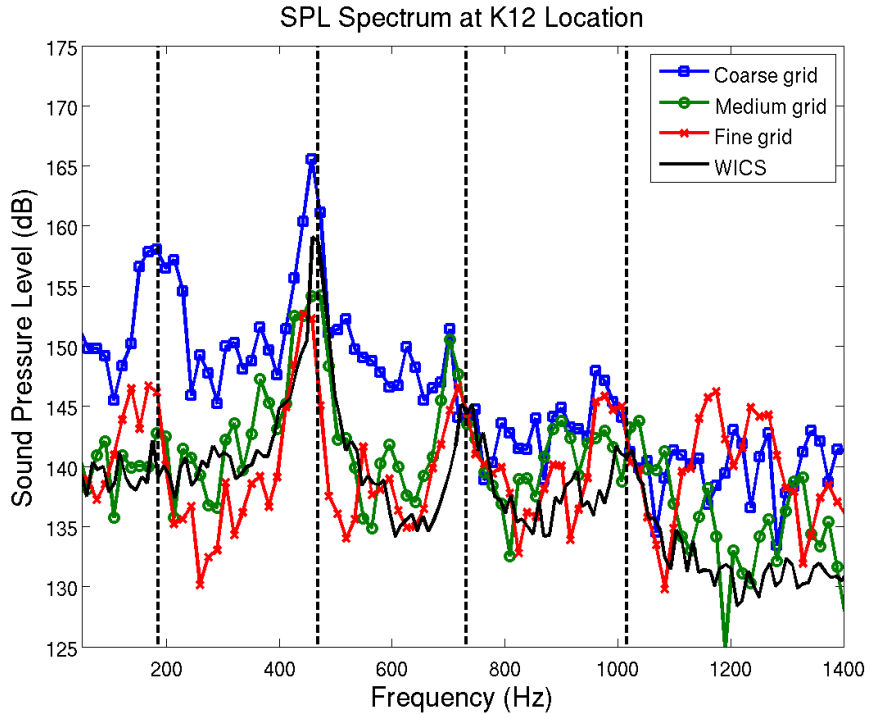


Figure 22: Grid resolution sensitivity for the K12 transducer

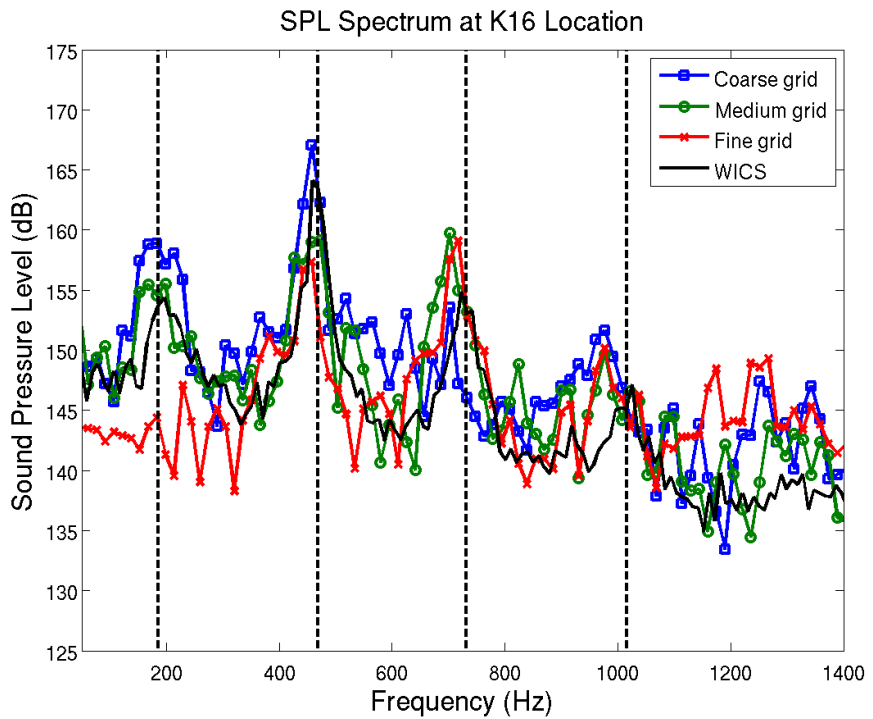


Figure 23: Grid resolution sensitivity for the K16 transducer

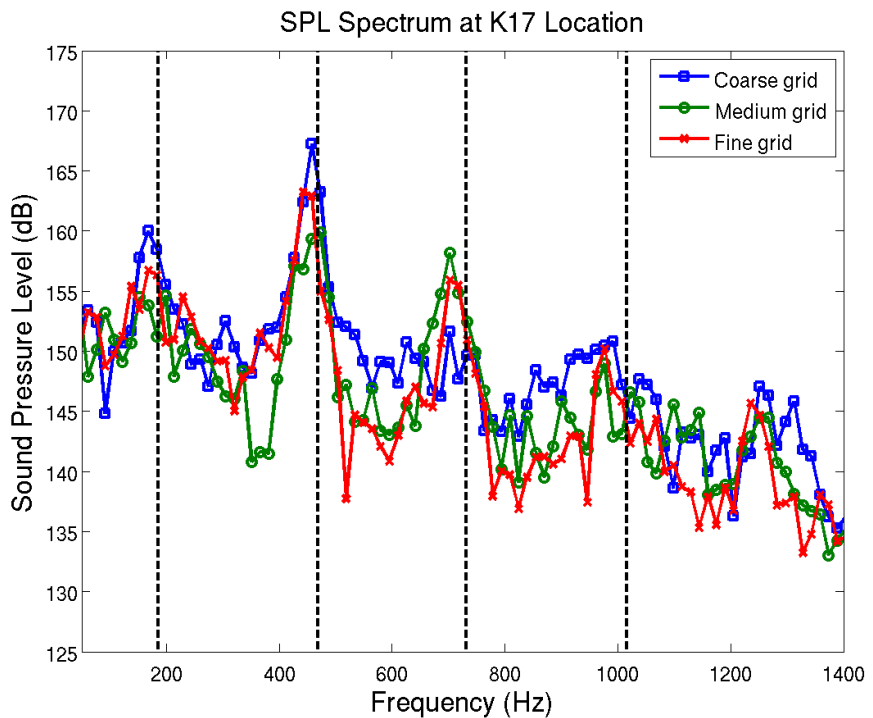


Figure 24: Grid resolution sensitivity for the K17 transducer

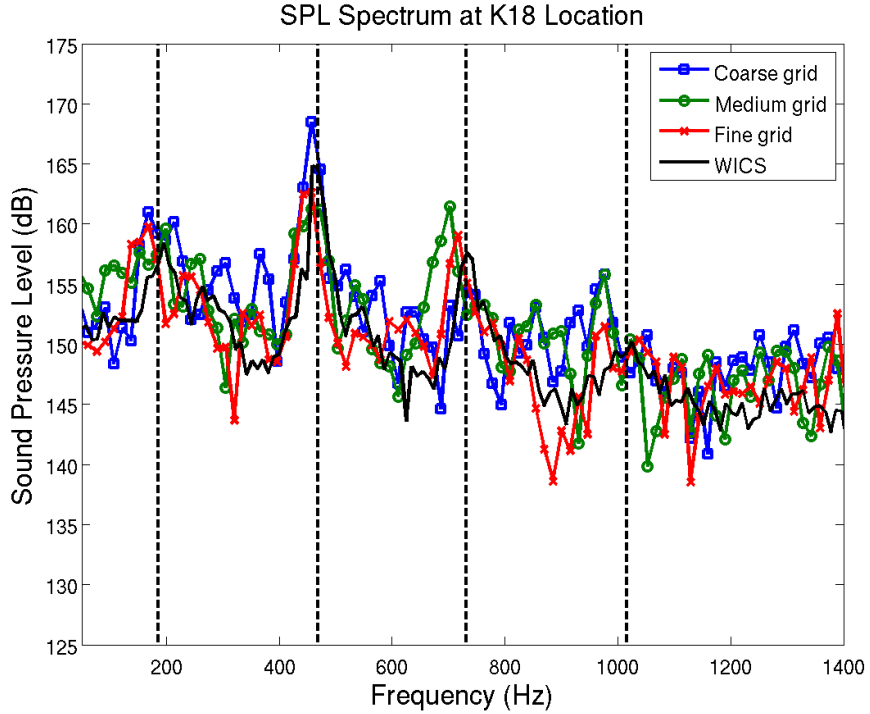


Figure 25: Grid resolution sensitivity for the K18 transducer

**4.1.3 Time Step Sensitivity Study.** The sensitivity of the solution to selection of time step was investigated. Solutions using time steps of  $dt = 8.0 \times 10^{-6}$ ,  $dt = 1.6 \times 10^{-5}$ , and  $dt = 4.0 \times 10^{-5}$  s were computed and compared. These solutions were all computed using five Newton subiterations. The computational expense for each of these solutions are presented in Table 27 in Appendix B.

The SPL spectra for the three cases are shown in Figs. 26 through 29. At the larger time step, the predicted frequencies shift to the left and the solution predicts frequencies that are lower than the experimental data. As the time step is decreased, the simulation is better able to capture the periodic motion and the frequency is better predicted. It is possible that this solution could be made more accurate if more subiterations were used, although this was not examined. The middle time step provides a good prediction of the first two modes but slightly under-predicts the frequency of the higher modes. The smaller time step fully captures the periodic motion and accurately predicts the frequency of all four modes, however this solution

shows a smoothing of the frequency spectrum. This smoothing is a result of a lack of frequency data due to using small data sets. Since each of these three solutions were run for the same number of time steps, the simulation physical time is decreased as the time step is decreased. The simulation with the largest time step spans 0.328 s, which includes 151 cycles at the predominant frequency of 460 Hz, whereas the simulation with the smallest time step spans only 0.066 s, representing only 30 cycles at 460 Hz. In order to provide a more robust solution with better-defined peaks, the solution at the smallest time step needs to be run for a much longer physical time in order to capture more cycles of the periodic motion. Based on a rule of thumb of having at least 60 cycles, the smallest time step would need to be run for twice as long as was run here. It is possible that some economy could be gained from using the small time step, however, if it results in being able to compute an accurate solution using fewer subiterations, but this was not investigated. Although the medium time step slightly under-predicts the third and fourth modes, it provides an acceptable balance between accuracy and computational cost, and the time step  $dt = 1.6 \times 10^{-6}$  s was chosen for all of the following solutions.

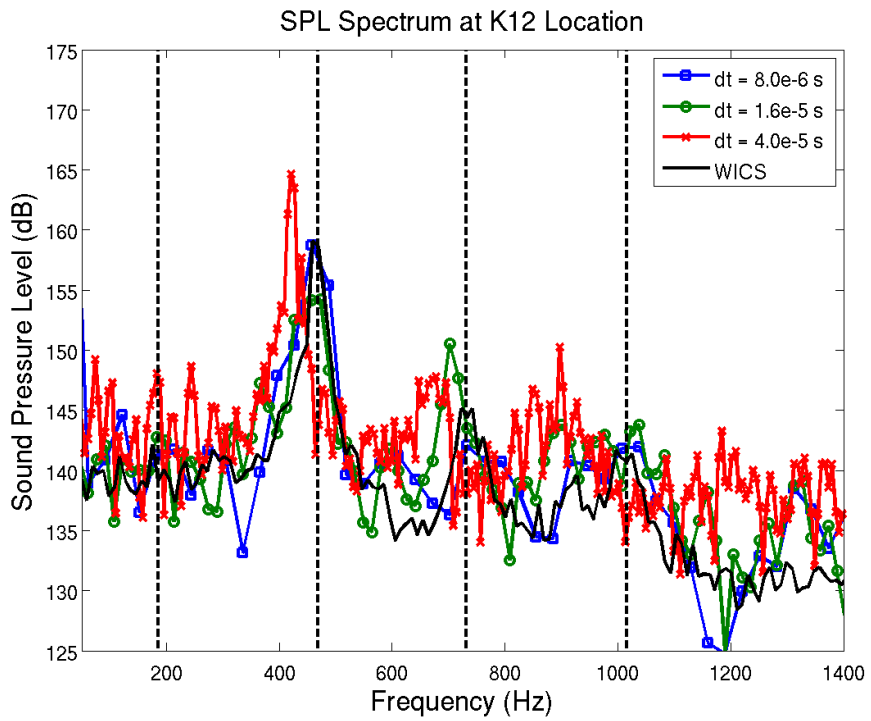


Figure 26: Time step sensitivity for the K12 transducer

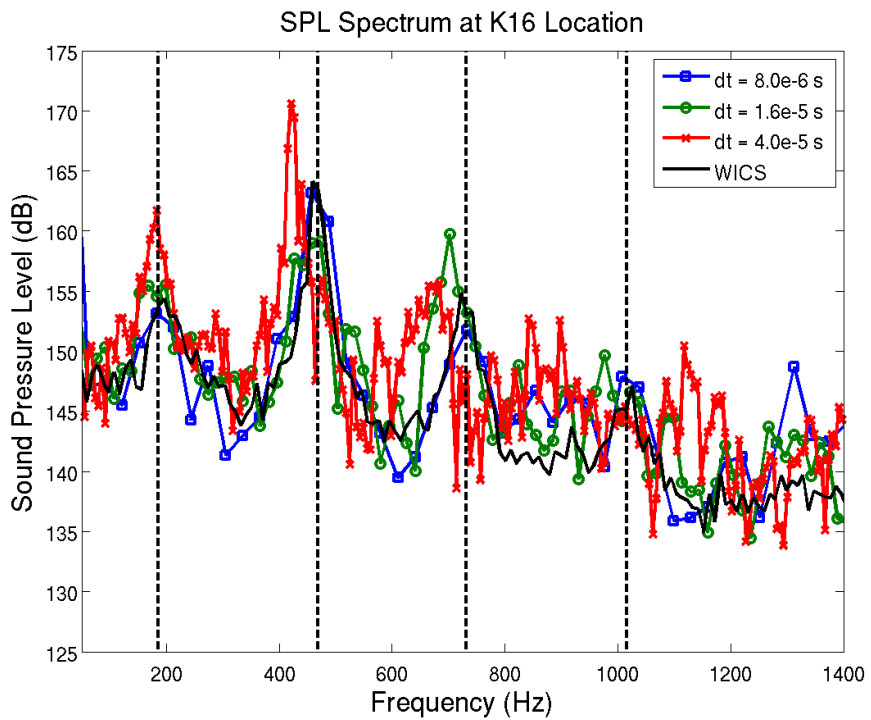


Figure 27: Time step sensitivity for the K16 transducer

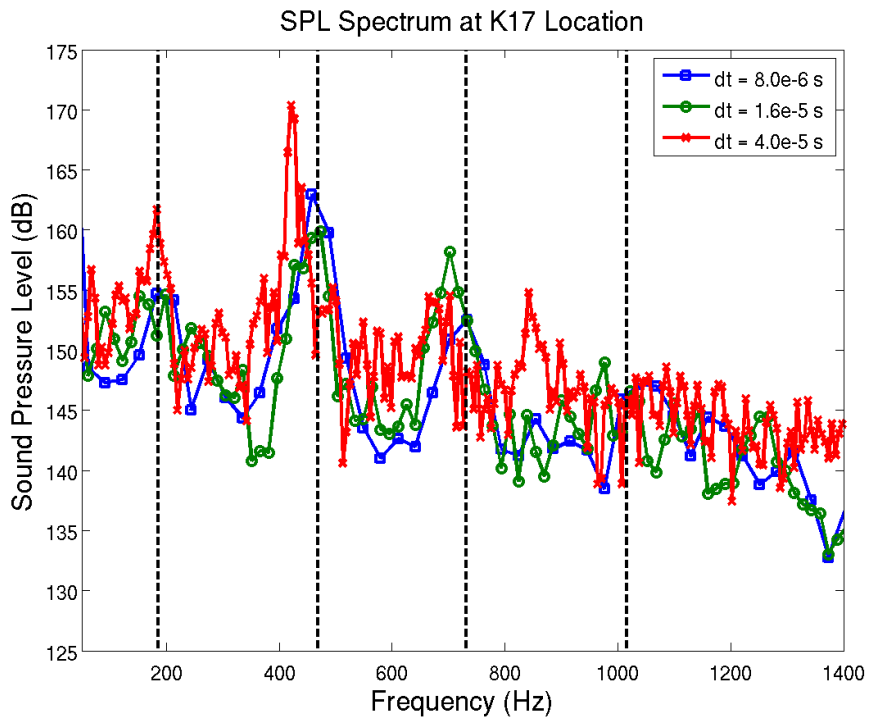


Figure 28: Time step sensitivity for the K17 transducer

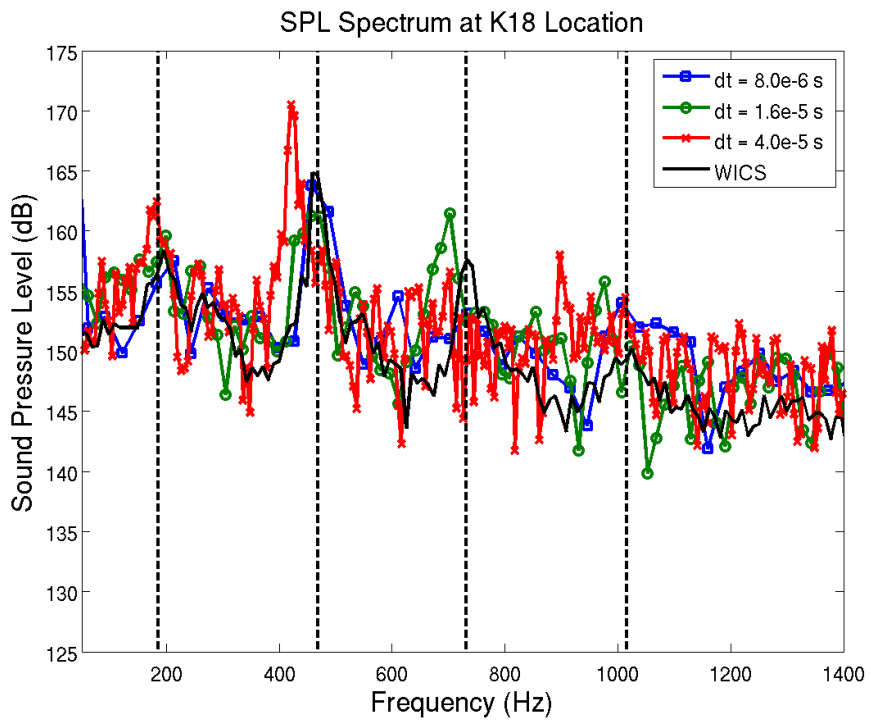


Figure 29: Time step sensitivity for the K18 transducer

*4.1.4 Empty Cavity Validation.* From the sensitivity studies, a set of parameters were selected which provided good agreement with the WICS data: the medium grid, time step of  $dt = 1.6 \times 10^{-5}$  s, and five Newton subiterations. The empty bay solution was run with these settings and the results directly compared to the WICS data. The pressure data for the K18 transducer is plotted against time in Fig. 30. All the pressure probe locations exhibit similar pressure histories. The assumption set forth by Nichols [14] that demonstrating that a time-accurate solution is statistically stationary is a sufficient condition for demonstrating convergence is also assumed here. It can be shown that the solution is statistically stationary by observing that the statistics for each data partition do not change. The mean pressure and the standard deviation for each data set for each transducer location are tabulated in Table 6. The percentages below each entry indicates the percent variation of that parameter from the mean value between data sets. None of the mean pressures for a data partition at a given transducer location vary by more than 1.5% from the mean for all of the data. The standard deviations are within 14% for all of the data sets but are within 10% for all but two of the data sets. These variations are sufficiently small such that the statistics may be considered as invariant with time.

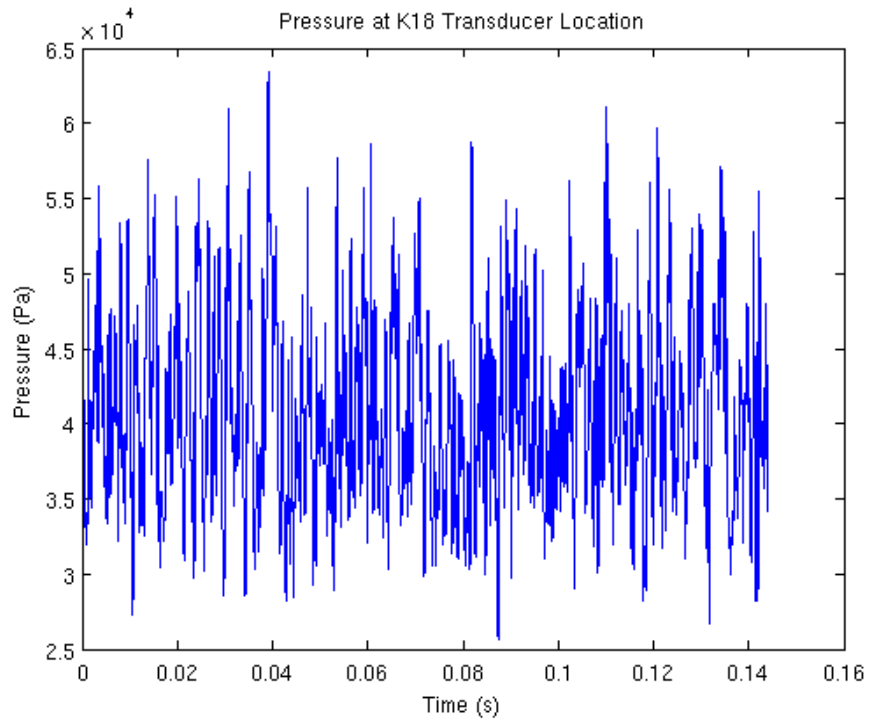


Figure 30: Pressure time history for K18 transducer location

The time averaged velocity vectors along the cavity centerline are shown in Fig. 31. They are colored by Mach number. The mean flow consists of the shear layer, which begins as the boundary layer at the upstream edge of the cavity and spreads as it travels downstream. Upon approaching the aft wall of the cavity, part of the shear layer flows upward and out of the cavity, continuing downstream while the rest stagnates on the aft wall and then circulates inside the cavity.

Table 6: Mean pressure and standard deviation for each data partition at each transducer location

| Transducer              | K12    |         |        |
|-------------------------|--------|---------|--------|
| Mean pressure (Pa)      | 31,787 | 31,874  | 31,875 |
|                         | -0.09% | 0.18%   | -0.09% |
| Standard deviation (Pa) | 1,959  | 1,596   | 1,991  |
|                         | 5.99%  | -13.68% | 7.70%  |
| Transducer              | K16    |         |        |
| Mean pressure (Pa)      | 39,174 | 39,036  | 39,104 |
|                         | 0.18%  | -0.18%  | -0.00% |
| Standard deviation (Pa) | 4,240  | 3,716   | 4,251  |
|                         | 4.20%  | -8.67%  | 4.48%  |
| Transducer              | K17    |         |        |
| Mean pressure (Pa)      | 36,674 | 36,591  | 37,395 |
|                         | -0.58% | -0.80%  | 1.38%  |
| Standard deviation (Pa) | 4,129  | 3,495   | 4,362  |
|                         | 3.35%  | -12.52% | 9.18%  |
| Transducer              | K18    |         |        |
| Mean pressure (Pa)      | 40,723 | 40,354  | 40,647 |
|                         | 0.37%  | -0.57%  | 0.18%  |
| Standard deviation (Pa) | 6,463  | 5,882   | 6,092  |
|                         | 5.16%  | -4.29%  | -0.87% |

The SPL spectra for the four transducer locations are shown in Figs. 32 through 35. For the K12, K16, and K18 locations, the WICS experimental data is plotted alongside the CFD data. No WICS data for the K17 transducer location was available. Again, the dashed lines indicate the frequencies of the first four modes as predicted by the Rossiter equation. All of the results show very good matching in predicting the frequency of the first two modes, although the amplitude of the second mode at 460 Hz is underpredicted by approximately 5 dB at every transducer location. Note that there is no presence of the first mode at the K12 location in either the CFD solution or the WICS experimental data. The third and fourth modes are present but are slightly misplaced. The CFD solutions predict the third mode at 702 Hz, which is 30 Hz lower than the WICS data. Additionally, the CFD solution overpredicts the amplitude of this peak by approximately 5 dB. At all four transducer locations there is a peak that corresponds to the fourth mode at 1025 Hz, although in all four locations, this peak

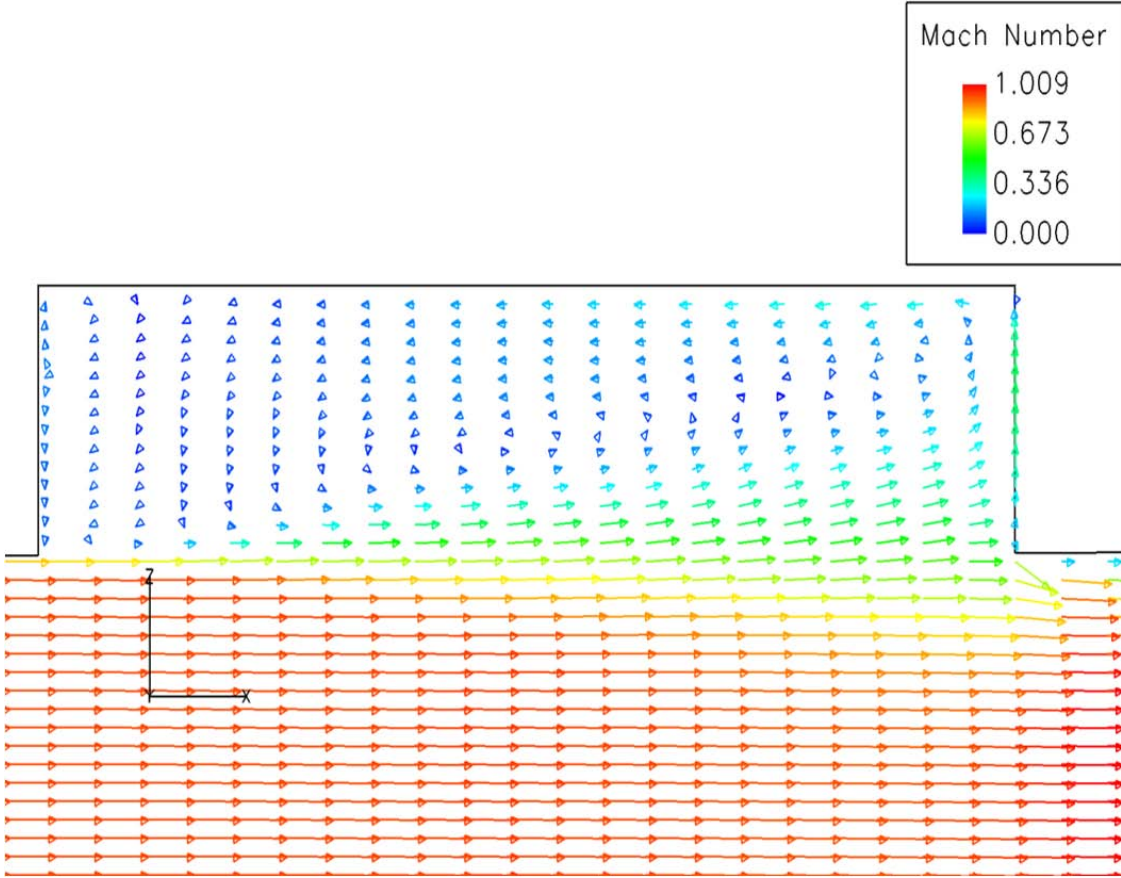


Figure 31: Time averaged velocity vectors for the empty cavity (colored by Mach number)

resides near several other peaks of the same or greater magnitude, making it unclear if it truly represents the fourth mode. The K18 location shows a peak at 976 Hz which, considering the downward shift of the third mode, could possibly represent the fourth mode. The other three locations have a corresponding peak at this frequency, although it is not as dominant in the K12, K16, nor K17 locations as it is in the K18 location. The overall broadband levels of noise correspond well with the WICS data.

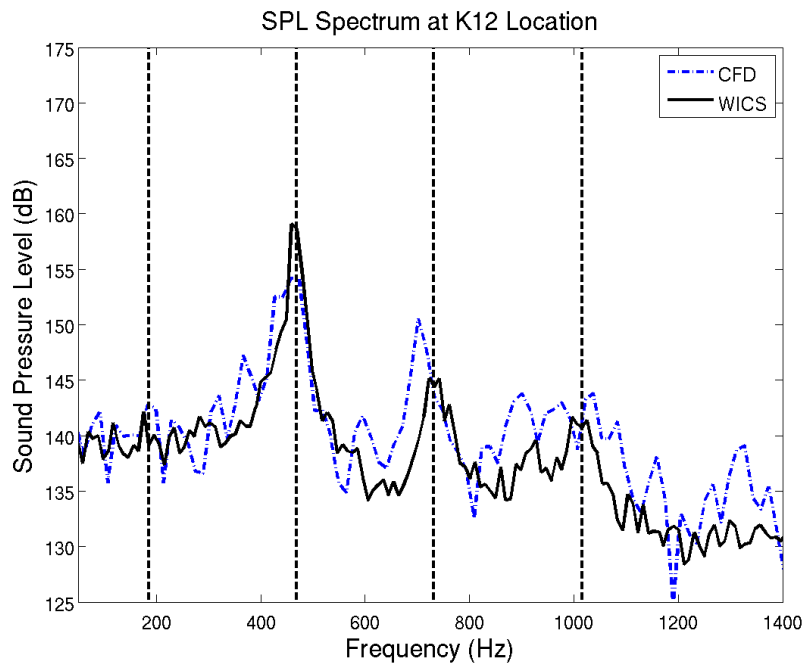


Figure 32: SPL spectrum at the K12 transducer location for the empty cavity

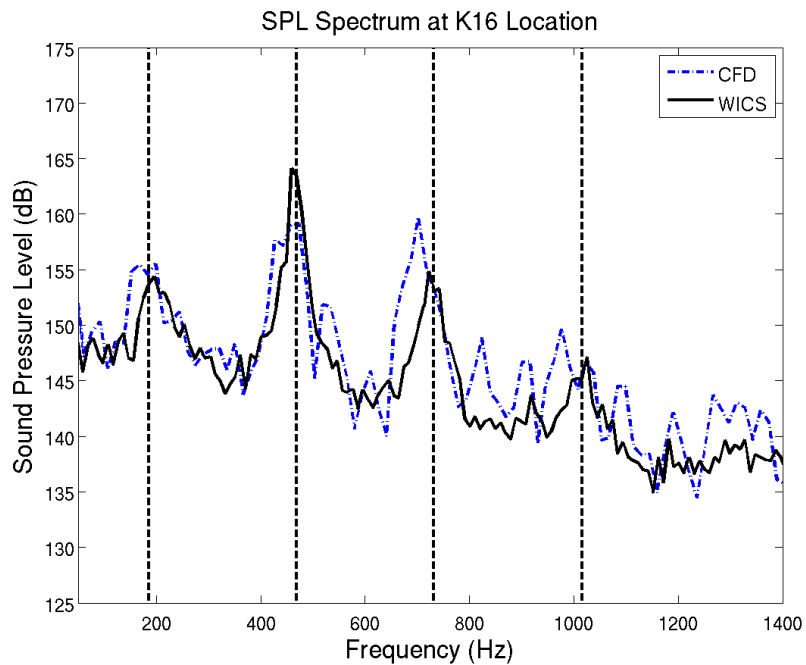


Figure 33: SPL spectrum at the K16 transducer location for the empty cavity

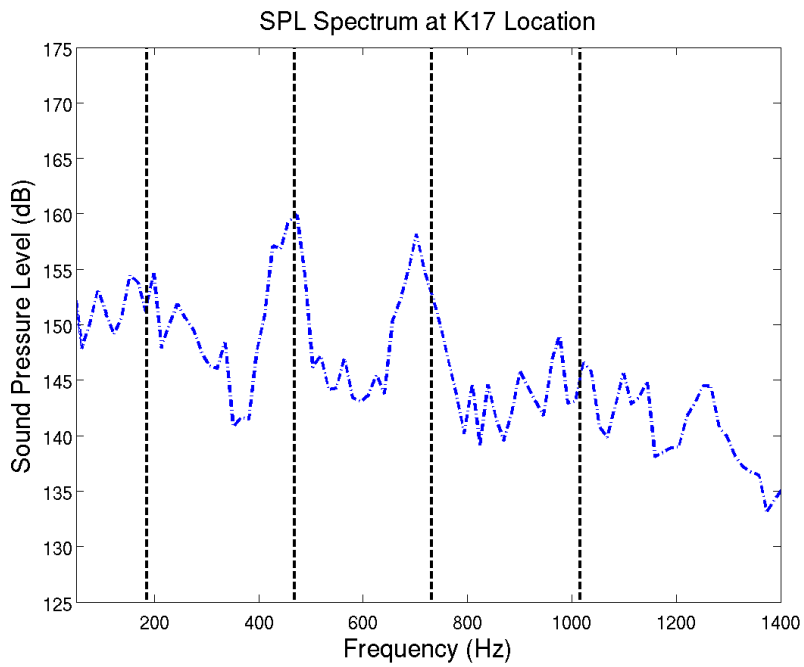


Figure 34: SPL spectrum at the K17 transducer location for the empty cavity

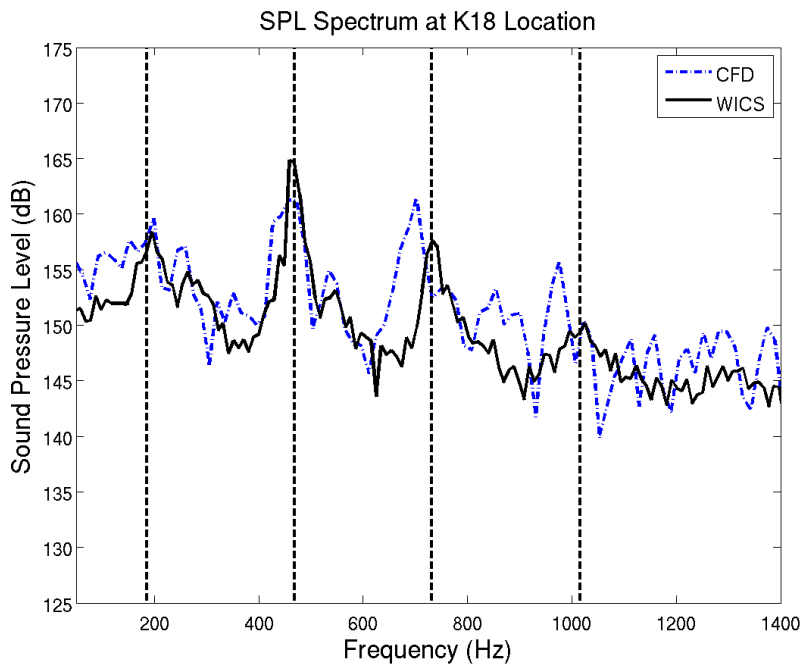


Figure 35: SPL spectrum at the K18 transducer location for the empty cavity

Pseudo-Schlieren images calculated from the pressure data along the centerline of the empty cavity are shown in Fig. 36. The images are taken starting at an arbitrary time  $t$  with snapshots at  $4.8 \times 10^{-4}$  s intervals, representing one-quarter of a cycle for the predominant cavity mode of 460 Hz. The pseudo-Schlieren images clearly show the development of the approaching boundary layer into turbulent structures which travel downstream and interact with the aft wall.

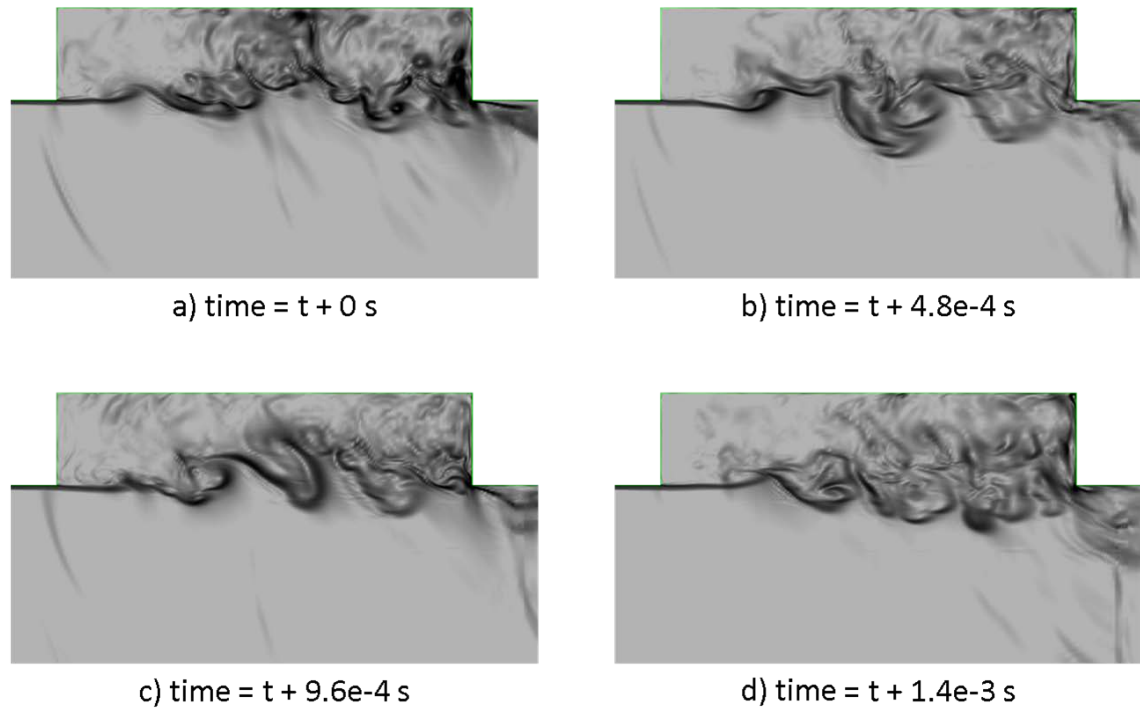


Figure 36: Pseudo-Schlieren images of empty cavity

The SPL spectra for the sidewall locations are plotted in Figs. 37 and 38. The vertical dashed lines correspond to the frequencies of the first four longitudinal modes as predicted by the Rossiter equation. These are not plotted against any WICS transducer data since the experiment did not take any sidewall pressure data. At the L01 location, the second, third, and fourth modes are clearly present, but the first mode is indistinguishable. The lack of a first mode coincides with the lack of a 195 Hz peak at the K12 transducer location, which resides at the same longitudinal distance in the cavity. At the L02 location, all four longitudinal modes are present. Similar trends are seen on the sidewall locations as with the four transducer locations: the second and third modes show peaks at roughly the same amplitudes, the third mode is predicted at 702 Hz, and the location of the fourth mode is ambiguous, with peaks present at 976 Hz and 1025 Hz. In general, the sidewall pressure spectra at each location matches the frequency content of the transducer at the corresponding longitudinal location, although the amplitude of the signal on the sidewalls is reduced from those on the cavity ceiling.

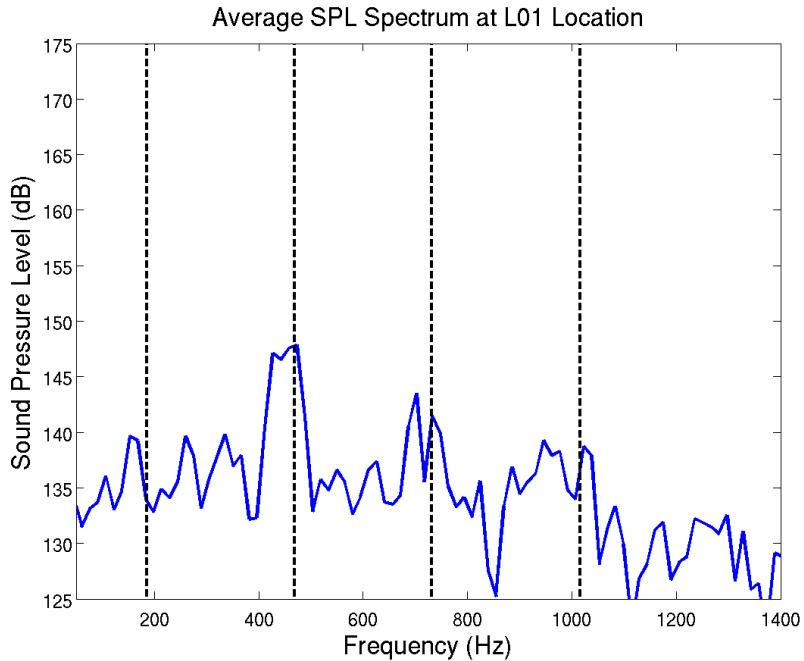


Figure 37: SPL spectrum at the L01 location for the empty cavity

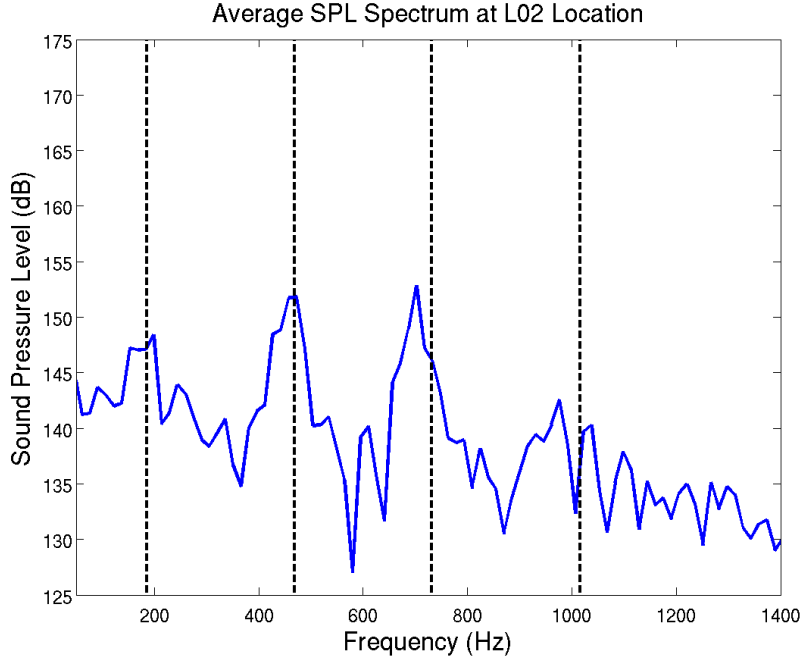


Figure 38: SPL spectrum at the L02 transducer location for the empty cavity

The turbulence in the cavity flow is dictated by the shedding of vortices from the shear layer and the fluid response to the downstream stagnation of these structures. The feedback loop occurs when signals from the aft wall stagnation travel upstream and back to the leading edge. This process can essentially be mapped within the volume of the cavity. As such, varying longitudinal positions within the cavity experience different portions of the cavity flow phenomenon. Since the longitudinal modes dominate the flow, the main direction of travel for the signals are in the streamwise directions, which explains why the pressure probes at corresponding longitudinal locations exhibit similar frequency response. Since the sidewalls essentially represent planes that are parallel with the dominant flow mechanism, the pressure fluctuations along the sidewalls are not as extreme as for the ceiling and aft walls, which lie in planes that are normal to the flow. The lack of any additional peaks in the sidewall pressure data indicate that there are no significant transverse waves traveling within the cavity. As such, there is no evidence of any lateral modes, and it is confirmed here that the longitudinal modes dominate the flow.

The CFD solution is validated against the WICS experimental data, showing good prediction of the frequency and magnitudes of the first and second modes. The solution shows reasonable agreement with the prediction of the third and fourth modes, although the amplitude of the third mode is overpredicted. There is no evidence of any lateral or vertical modes from the sidewall pressure fluctuation data. It has been shown that the CFD solution with the settings shown here produce reasonable agreement with the experimental data.

## 4.2 *Cavity with Store in Carriage Configuration*

With the solver settings validated against the WICS data, the solutions for the carriage, shear, and forward shear configurations were computed. The results for the carriage configuration are presented here.

The time averaged velocity vectors along the cavity centerline are shown in Fig. 39. They are colored by Mach number. The flow looks very similar to the empty cavity scenario. As in the empty cavity flow, the shear layer spreads as it travels downstream, with part of the shear layer flowing upward and out of the cavity at the aft wall and the rest stagnating and then circulating inside the cavity. The flow circulates around the cavity, providing a very similar profile to what was observed in the empty cavity, although the flow between the top of the store and the cavity ceiling is accelerated due to the geometry here being restricted.

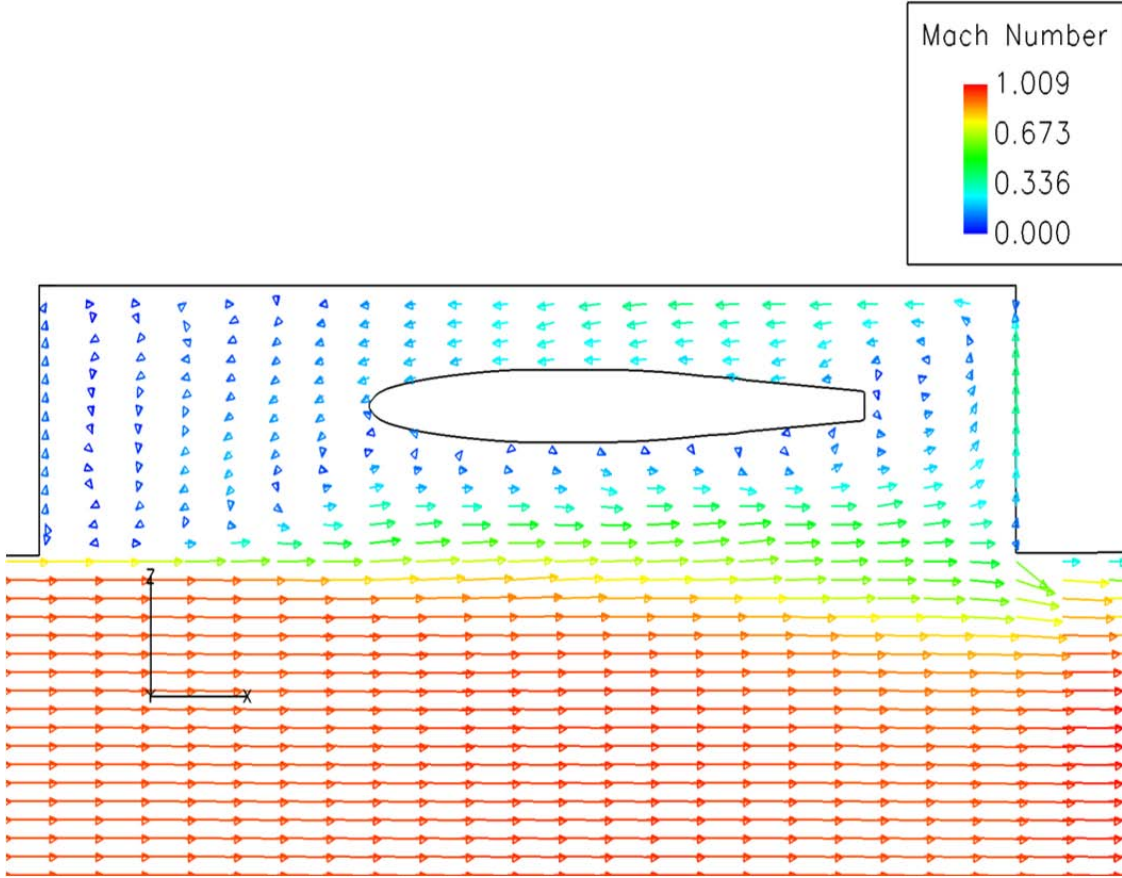


Figure 39: Time averaged velocity vectors for the carriage configuration (colored by Mach number)

The SPL spectra for the four transducer locations are plotted against the empty cavity results in Figs. 40 through 43. The vertical dashed lines correspond to the frequencies of the first four modes as observed in the WICS experimental data. At all four transducer locations, the carriage configuration shows good agreement with the empty cavity data in frequency and amplitude prediction. The one discrepancy is in the third mode, where the carriage configuration shows a peak at 732 Hz, which corresponds with the location of the third peak in the WICS data and not the third peak that was predicted in the empty cavity solution. This slight shift of one peak is not indicative of a store effect on the acoustic response. It appears that the presence of the store in the carriage position does not have a significant effect on the fluid

response in the cavity. This observation was expected since this was one of the key findings from the AFFDL wind tunnel test [5].

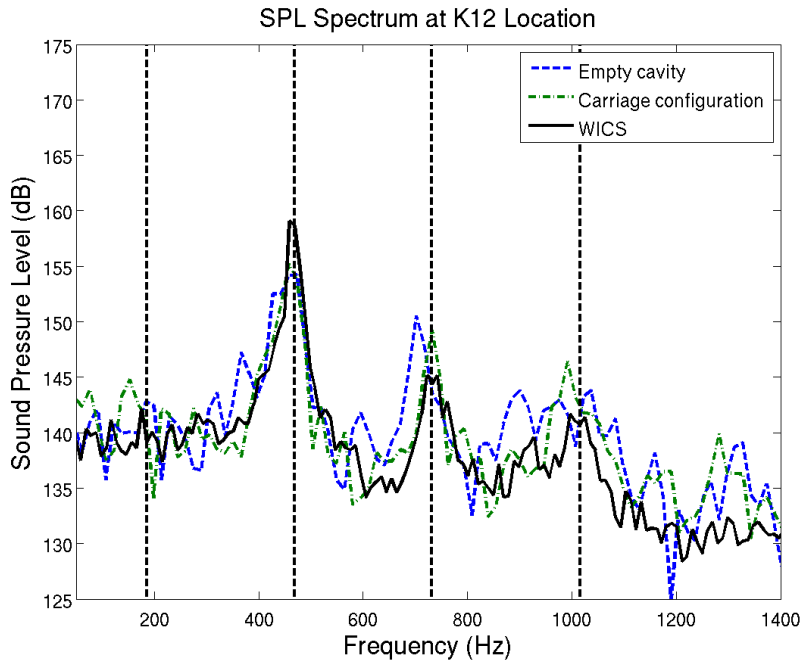


Figure 40: SPL spectrum at the K12 transducer location for the carriage configuration

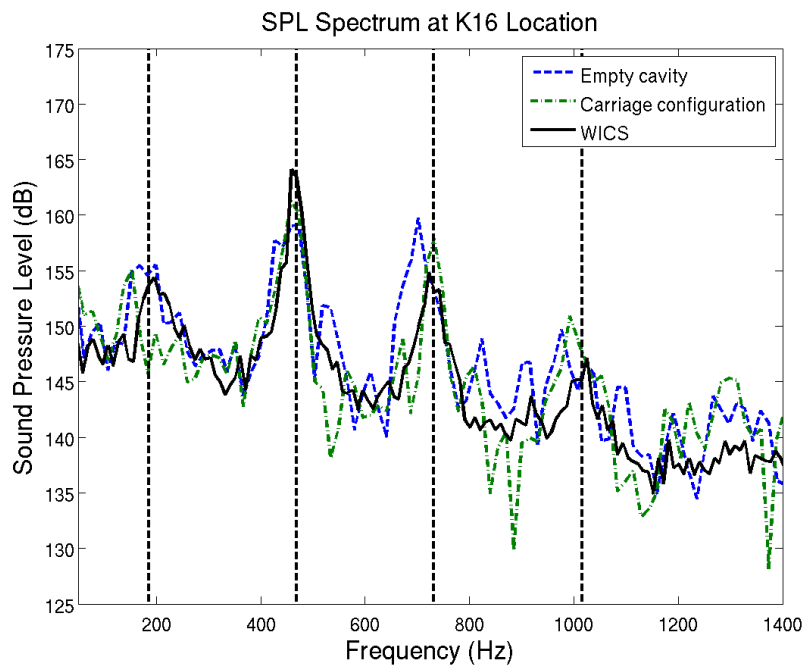


Figure 41: SPL spectrum at the K16 transducer location for the carriage configuration

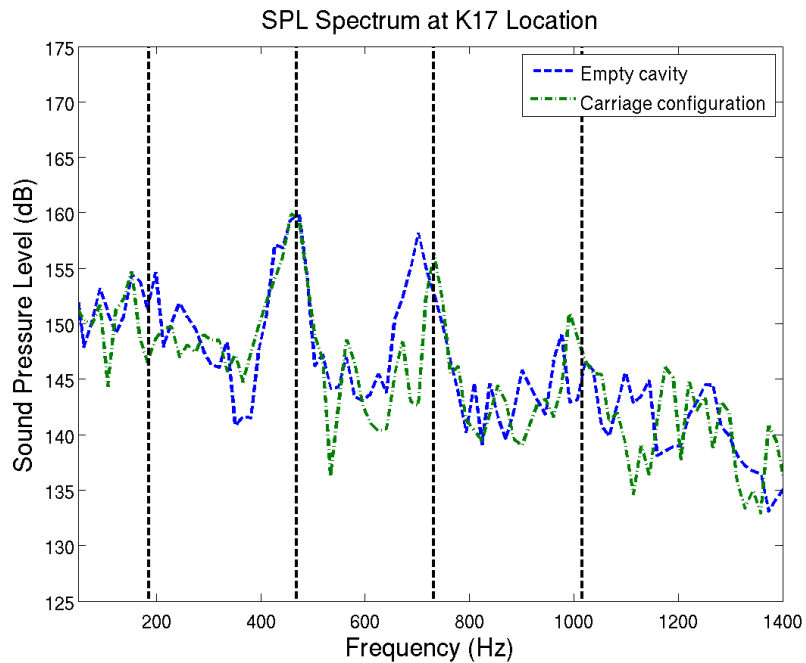


Figure 42: SPL spectrum at the K17 transducer location for the carriage configuration

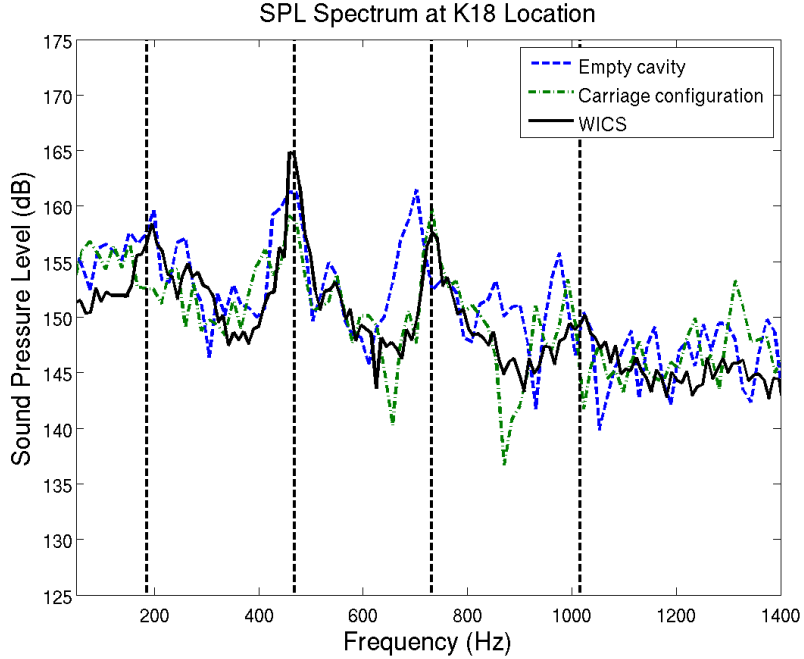


Figure 43: SPL spectrum at the K18 transducer location for the carriage configuration

Pseudo-Schlieren images from the centerline of the cavity are shown in Fig. 44. The images are taken starting at an arbitrary time  $t$  with snapshots at  $4.8 \times 10^{-4}$  s intervals, representing one-quarter of a cycle for the predominant cavity mode of 460 Hz. The presence of the store does not interfere with the vortex shedding process and downstream stagnation. The store is located far enough up in the cavity that the shear layer passes below it. A comparison of Figs. 36 and 44 shows a very similar overall shape to the structure in the shear layer.

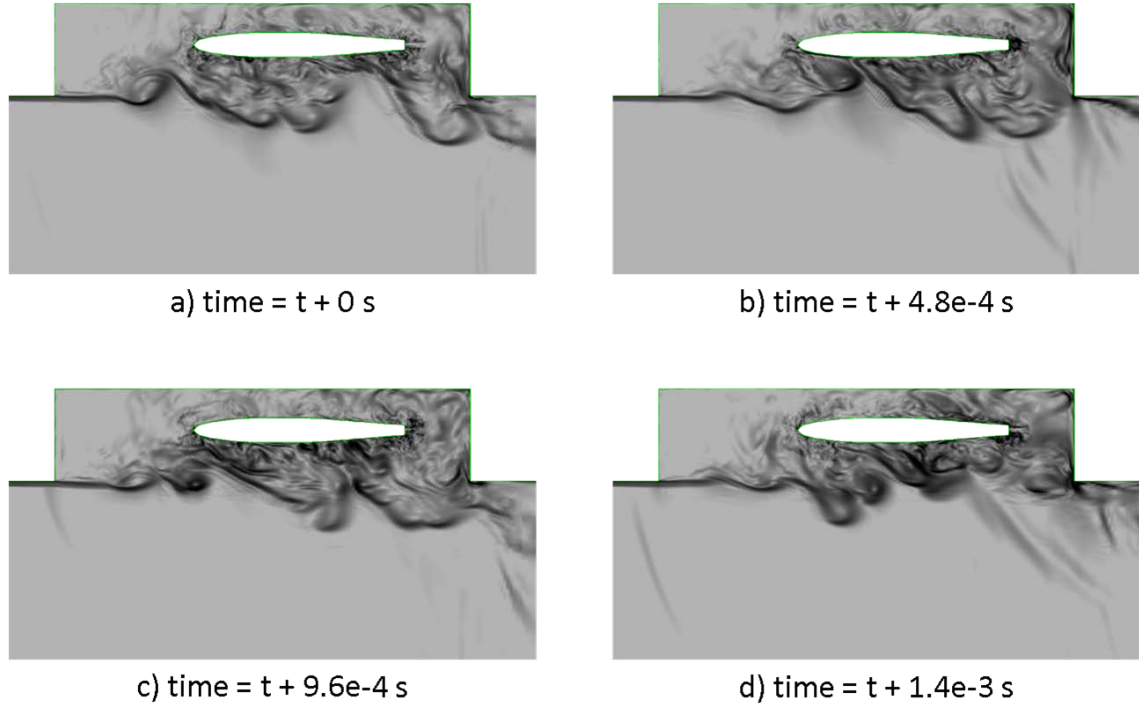


Figure 44: Pseudo-Schlieren images of carriage configuration

The SPL spectra for the sidewall locations are plotted in Figs. 45 and 46. Again, these results are plotted against the spectra from the empty cavity. The same trends which were observed for the transducer locations are evident for these cases as well, including the shift of the third peak in the solution for the carriage configuration and the decreased overall sound levels. As with the empty cavity, the only modes present are the longitudinal modes which are observed along the cavity centerline and which are predicted by the Rossiter equation.

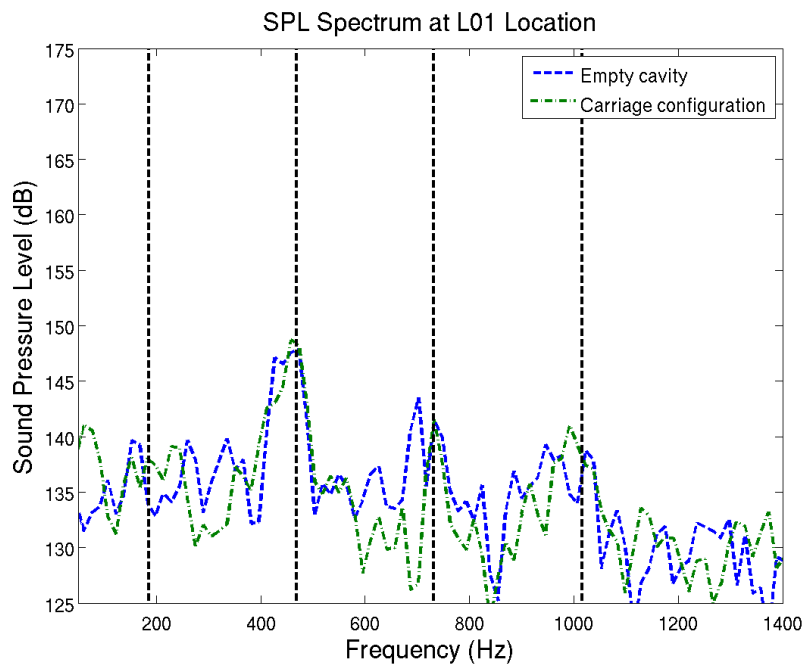


Figure 45: SPL spectrum at the L01 location for the carriage configuration

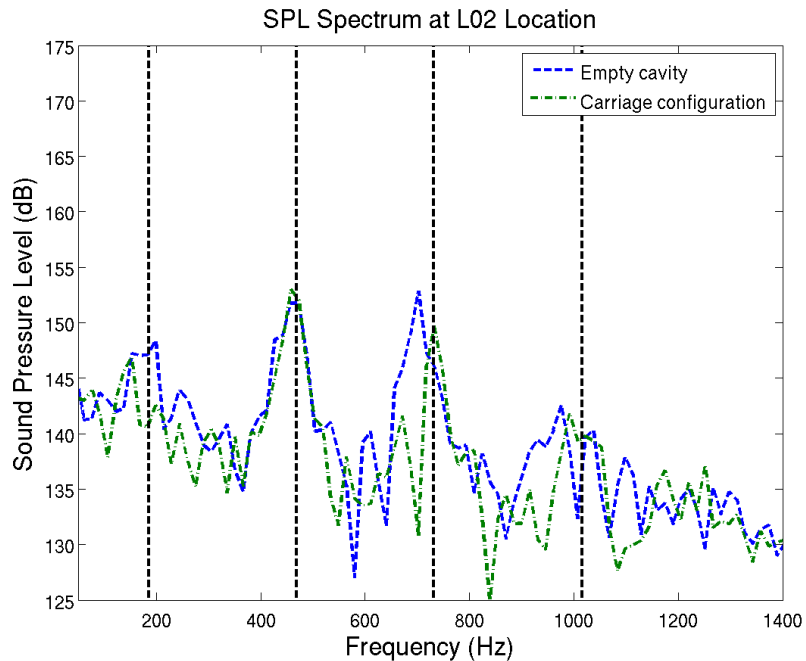


Figure 46: SPL spectrum at the L02 transducer location for the carriage configuration

The force and moment histories on the store are plotted against time in Figs. 48 and 49. The coordinate system is defined as illustrated in Fig. 47. The system is a right-handed system such that the y-axis points into the page. The mean and standard deviation for each of the forces and moments are summarized in Table 7. The dominant force on the store is the longitudinal force imposed on the store. There is also a significant force in the vertical direction. There is essentially no lateral force on the store. It is of note that the dominant moment is a pitch-up moment. While a pitch-up behavior has been observed and well-documented for some cavity-released stores, this behavior is often attributed to the interaction of the store with the shear layer. These data suggest, however, that the store is subjected to a pitch-up moment from the time of release. There is also a fluctuating roll moment, although this is centered about the x-axis. There is effectively no yaw moment present on the store.

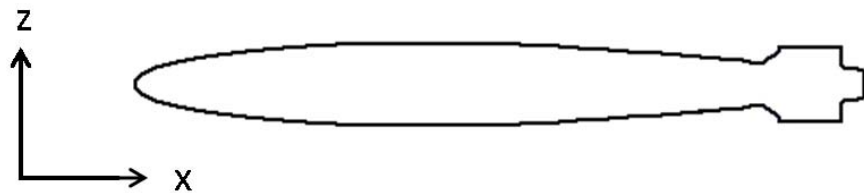


Figure 47: Definition of coordinate system

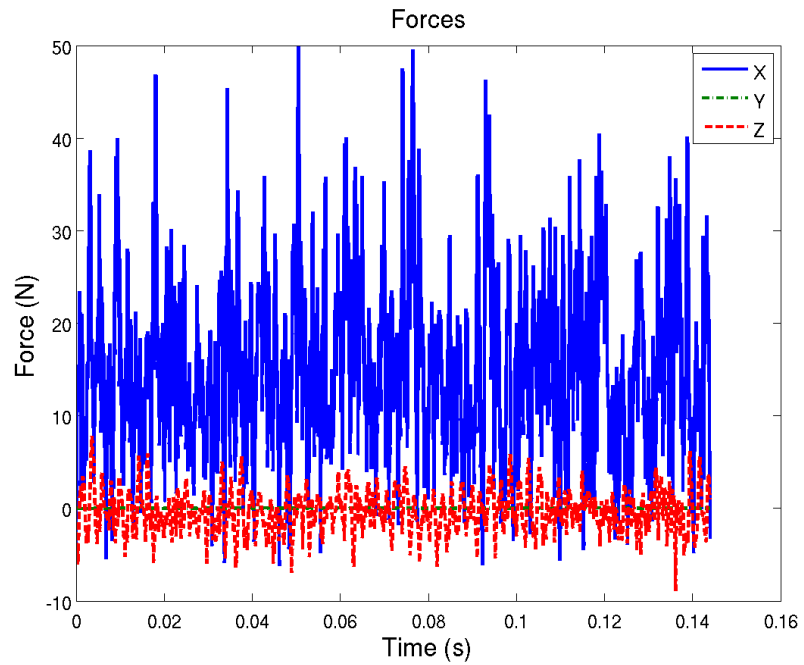


Figure 48: Force time history for the store in the carriage configuration

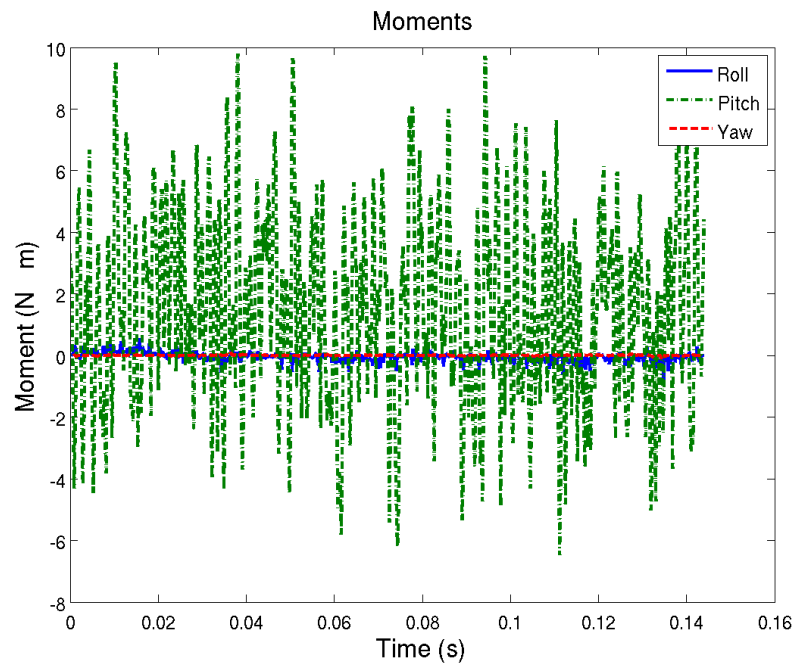


Figure 49: Moment time history for the store in the carriage configuration

Table 7: Summary of store forces and moments in carriage configuration

|                    | Mean Value | Standard Deviation |
|--------------------|------------|--------------------|
| Longitudinal force | 14.00 N    | 9.33 N             |
| Lateral force      | 0.01 N     | 0.01 N             |
| Vertical force     | -0.55 N    | 2.23 N             |
| Roll moment        | -0.04 N-m  | 0.12 N-m           |
| Pitch moment       | 1.16 N-m   | 2.98 N-m           |
| Yaw moment         | 0.00 N-m   | 0.01 N-m           |

The time-averaged pressure coefficient along the top and bottom of the store are presented in Fig. 50. There is an overwhelming negative pressure acting on the majority of the store. The pressure along the top of the store steadily increases from  $x/L = 0.0$  to  $x/L = 0.7$ . Over this same span, the pressure along the bottom of the store oscillates but displays a slight overall decrease in pressure. Aft of  $x/L = 0.7$ , interference with the fins on the store creates a sharp increase in pressure, although there maintains a pressure differential between the top and bottom. From the pressure distribution, the center of pressure can be calculated. Table 8 summarizes the average pressure coefficient differential (taken as the pressure coefficient on the top of the store minus the pressure coefficient on the bottom of the store), the center of pressure, and the store's center of mass. From the definition of the pressure coefficient differential used here, a positive value indicates a net force downward on the store. The pitch-up behavior can thus be explained: the net pressure differential creates a downward force which acts at a point on the store which is aft of the center of mass, resulting in a pitch-up moment. Note that with the center of pressure aft of the center of gravity, the store is stable.

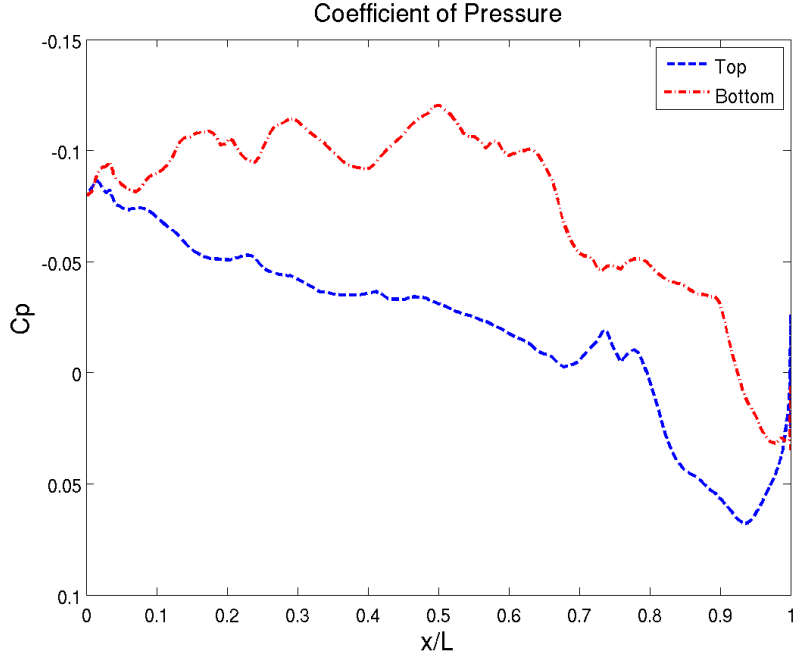


Figure 50: Pressure coefficient on top and bottom of store in carriage configuration

Table 8: Average pressure differential, center of pressure, and center of mass for the store in carriage configuration

| Average Pressure Differential<br>$C_{P,top} - C_{P,bottom}$ | Center of Pressure<br>x/L | Center of Mass<br>x/L |
|---|---------------------------|-----------------------|
| 0.041   | 0.569                     | 0.459                 |

The longitudinal and vertical force spectra are plotted alongside the K16 transducer spectrum in Figs. 51 and 52. The K16 transducer was selected because it showed the best prediction of the first four acoustic modes. Note that the longitudinal and vertical forces are plotted on different scales and differ by about two orders of magnitude. The force spectra are plotted on a logarithmic scale in order to match the scaling with the cavity ceiling SPL. The force spectra show a very strong correlation to the pressure fluctuations on the cavity ceiling. The first four modes as observed on the cavity ceiling are also apparent in the store forces. The relative amplitudes of the peaks from the broadband noise levels also correlate. The pitch and roll moment spectra are also plotted alongside the K16 transducer spectrum in Figs. 53 and 54.

As with the force spectra, the moment spectra are plotted on a logarithmic scale. As with the forces, note that the pitch and roll moments are plotted on different scales and differ by about three orders of magnitude. The pitch moment spectrum shows a very strong correlation to the K16 SPL spectrum. The modal frequencies and the peak relative amplitudes match very well with the K16 SPL. The roll moment spectrum does not show any correlation to the K16 spectrum. None of the cavity modes are present in the roll moment data. There is one peak in the roll moment spectrum which corresponds to the third mode, but its amplitude does not distinguish it from the broadband noise.

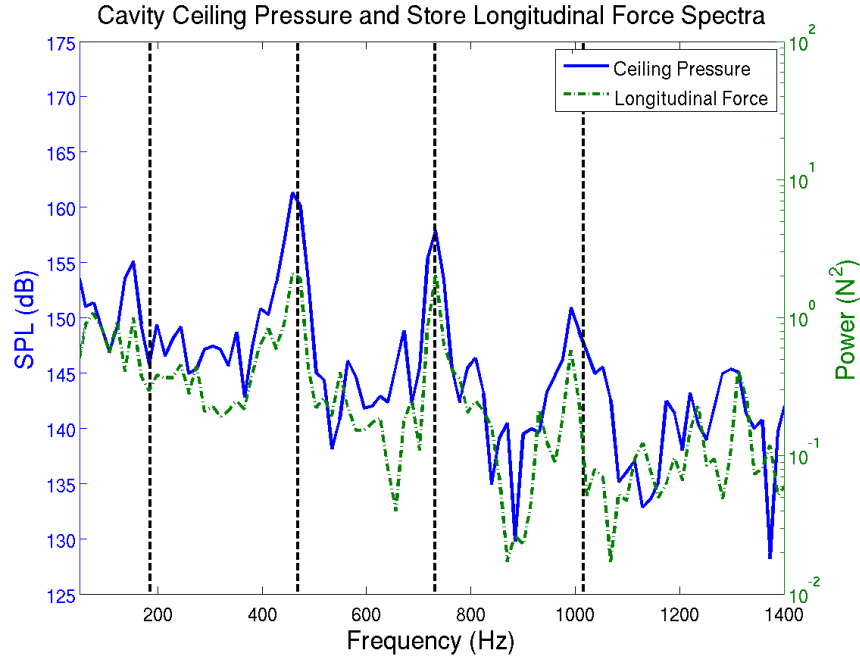


Figure 51: Store longitudinal force frequency spectrum (right axis) and K16 transducer SPL spectrum (left axis) for carriage configuration

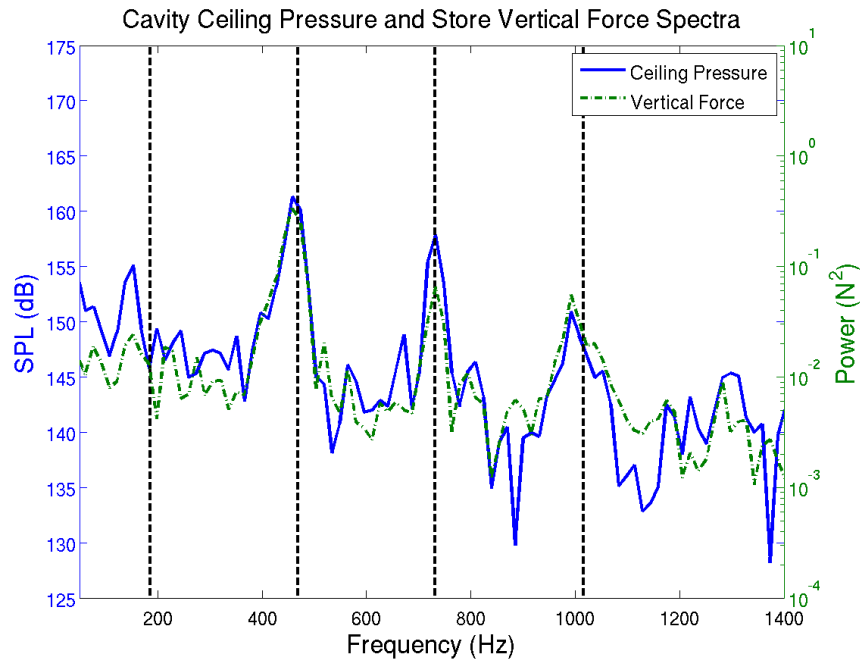


Figure 52: Store vertical force frequency spectrum (right axis) and K16 transducer SPL spectrum (left axis) for carriage configuration

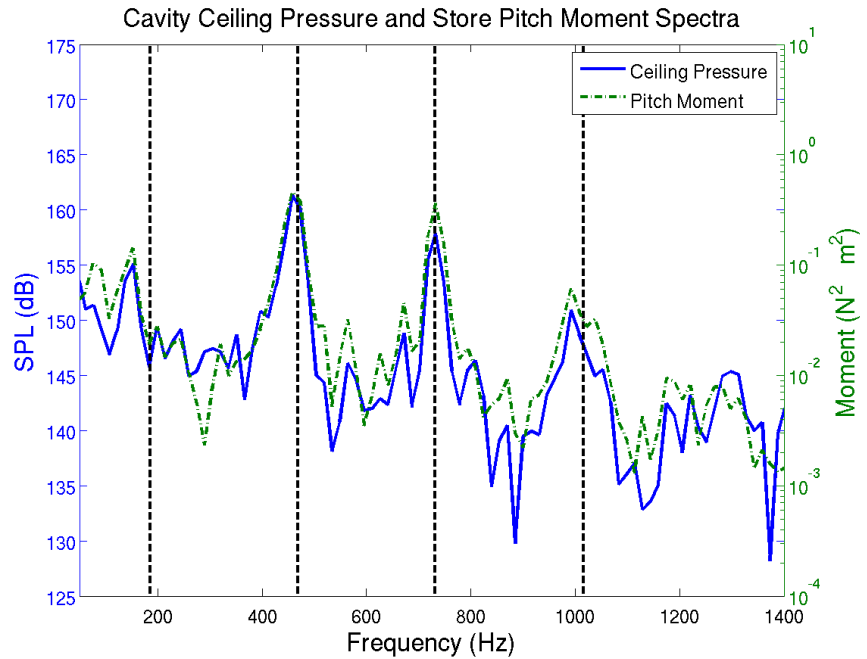


Figure 53: Store pitch moment frequency spectrum (right axis) and K16 transducer SPL spectrum (left axis) for carriage configuration

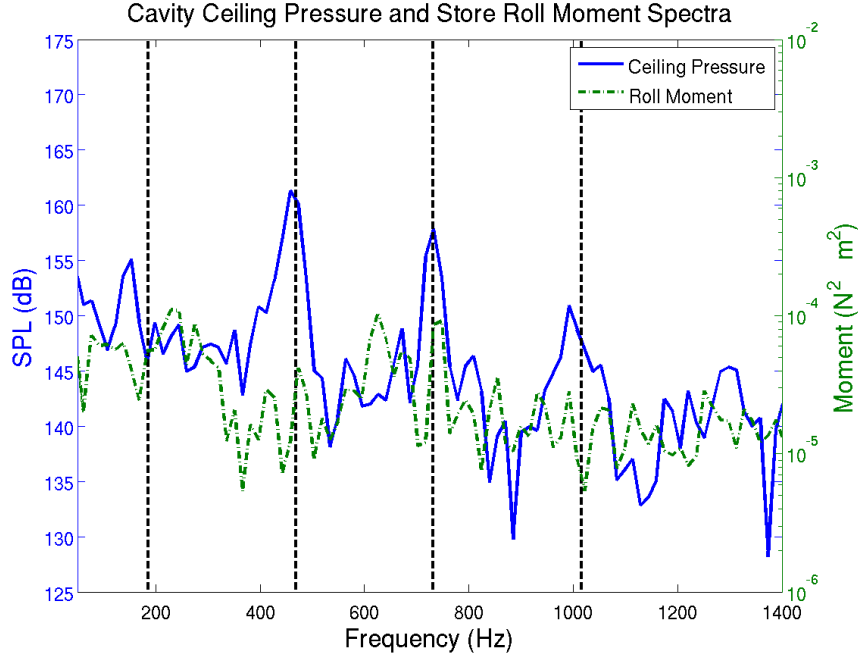


Figure 54: Store roll moment frequency spectrum (right axis) and K16 transducer SPL spectrum (left axis) for carriage configuration

The SPL spectra on the surface of the store are presented in Figs. 55 through 57. Each of the figures presents the SPL spectra at a given longitudinal position on the store. The pressure spectra at each longitudinal position correlate well with each other. At  $x/L = 0.25$ , the second, third, and fourth modes are clearly present with the second mode being the dominant frequency. This longitudinal position corresponds almost with the longitudinal position of the K12 transducer, so it is not surprising to see a lack of the first mode here. At  $x/L = 0.50$ , the first three modes are clearly evident, although here the second and third modes are roughly equivalent in amplitude. At the  $x/L = 0.75$  location, the only clear mode present is the third mode.

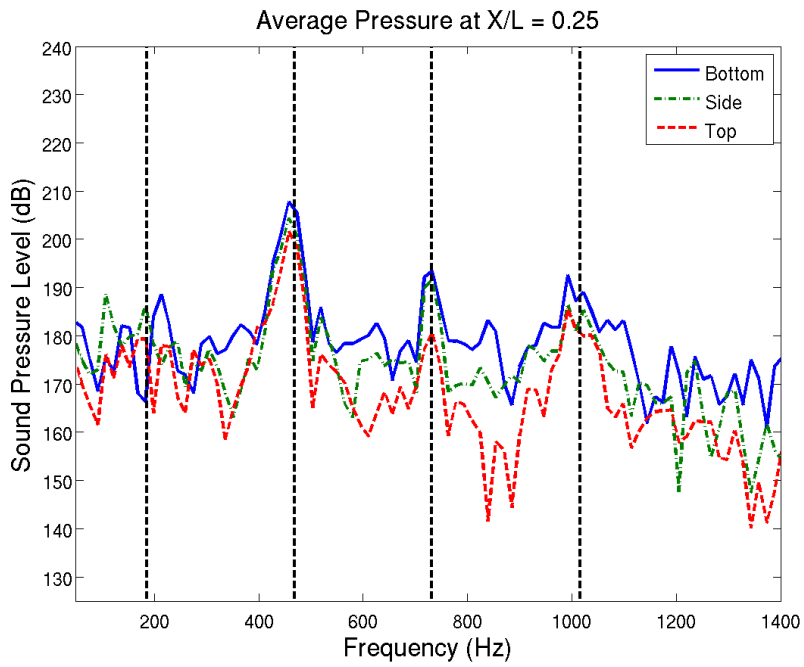


Figure 55: SPL spectra on store body at  $x/L = 0.25$  for carriage configuration

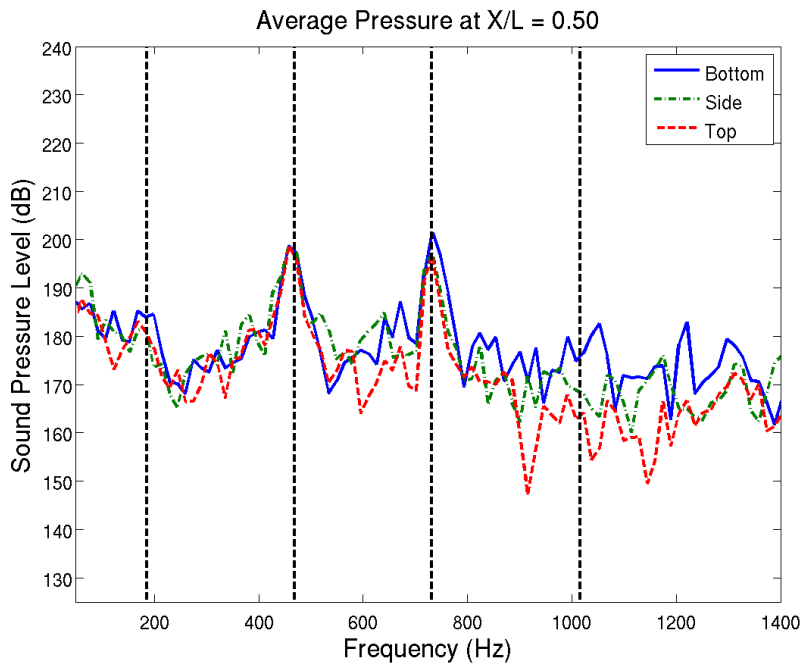


Figure 56: SPL spectra on store body at  $x/L = 0.50$  for carriage configuration

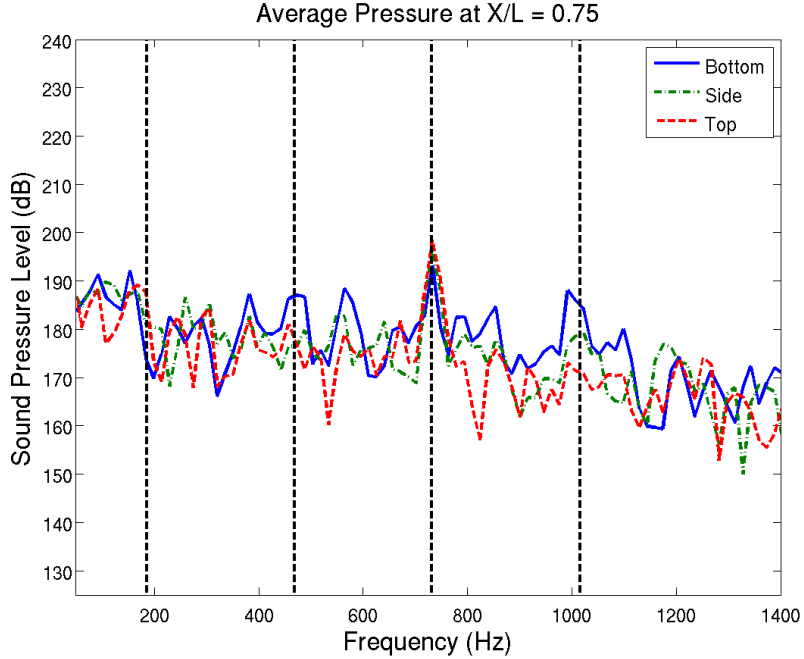


Figure 57: SPL spectra on store body at  $x/L = 0.75$  for carriage configuration

The same vibrational modes which are observed in the empty cavity are also present for the cavity with a store in carriage. Previous observations that small (relative to the cavity) stores located in the cavity do not affect the acoustic response of the cavity are confirmed here. A comparison of the cavity surface pressure fluctuations and the store force and moment loadings shows correlation between the longitudinal force, vertical force, and pitch moment with the cavity vibrational modes. The dominant moment on the store in the carriage location is a pitch-up moment. The pressure fluctuations on the store in the cavity vary by longitudinal position and correlate between circumferential position at a given longitudinal position.

#### 4.3 Cavity with Store in Shear Configuration

The results for the shear configuration are presented here. It is shown that the flow characteristics in the shear configuration differ greatly from the carriage configuration. It is expected that these fundamental differences will influence the

behavior of a cavity-released store as it transitions between the two positions during a separation event.

The time averaged velocity vectors along the cavity centerline are shown in Fig. 58. They are colored by Mach number. The presence of the store prevents the shear layer from spreading as in the empty cavity and the carriage configuration. Instead, the shear layer splits as two thinner layers travel around the top and bottom of the store, reforming behind the store. Once it has reformed, however, it behaves similarly as in the previous configurations, with part of the shear layer flowing upward and out of the cavity at the aft wall and the rest stagnating and then circulating inside the cavity.

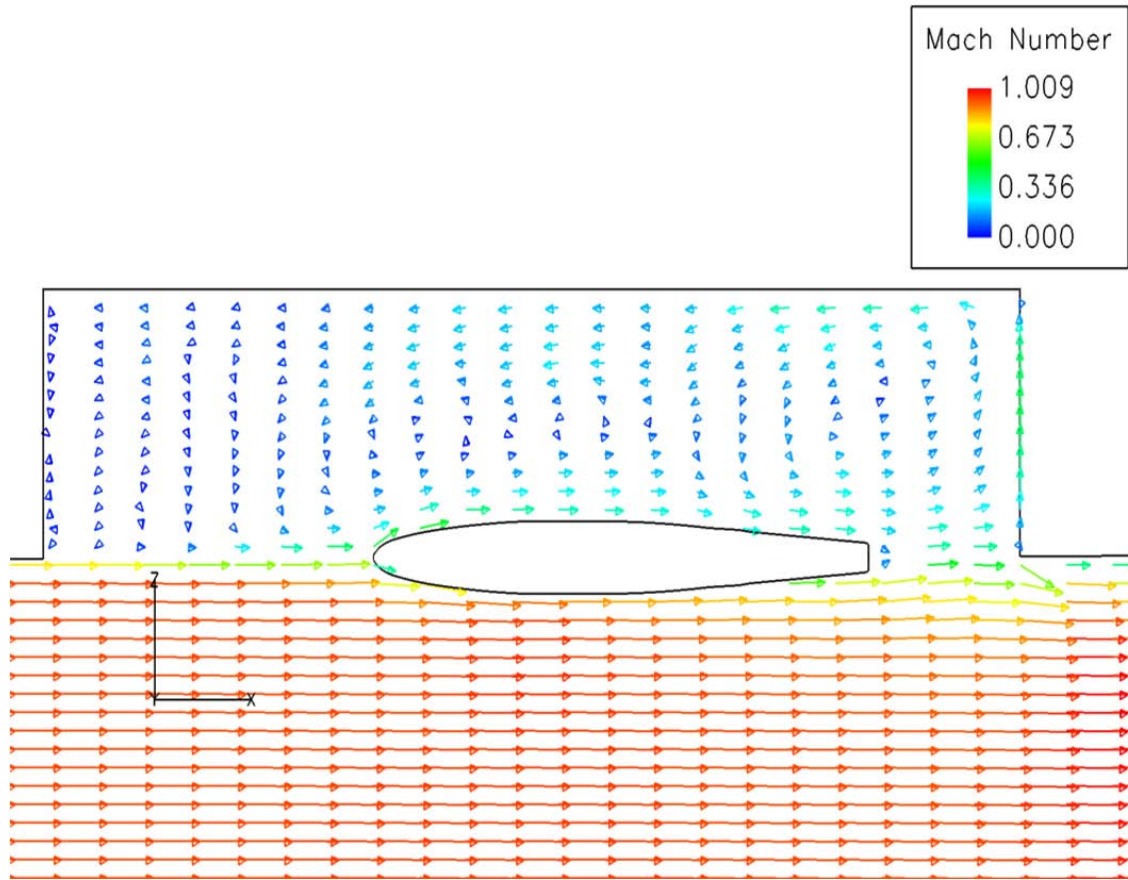


Figure 58: Time averaged velocity vectors for the shear configuration (colored by Mach number)

The SPL spectra for the four transducer locations are plotted against the empty cavity results in Figs. 59 through 62. The vertical dashed lines correspond to the frequencies of the first four modes as predicted by the Rossiter equation. Generally speaking, the shear configuration shows good agreement with the empty cavity data in frequency and amplitude prediction at all four transducer locations. As with the carriage configuration, the shear configuration shows a peak at 732 Hz for the third mode, which corresponds with the location of the third peak in the WICS data. Also, the fourth mode at the K12 location is much more clearly defined in the shear configuration than the empty cavity. Additionally, the overall noise levels and the amplitude of the first mode are lower in the shear configuration than the empty cavity. This slight suppression of sound levels is possibly the result of the store acting as a spoiler.

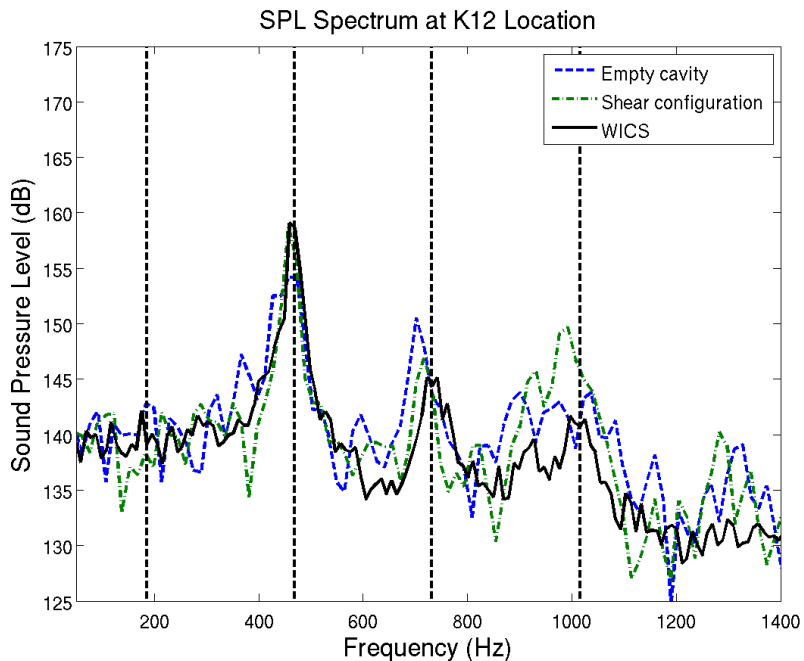


Figure 59: SPL spectrum at the K12 transducer location for the shear configuration

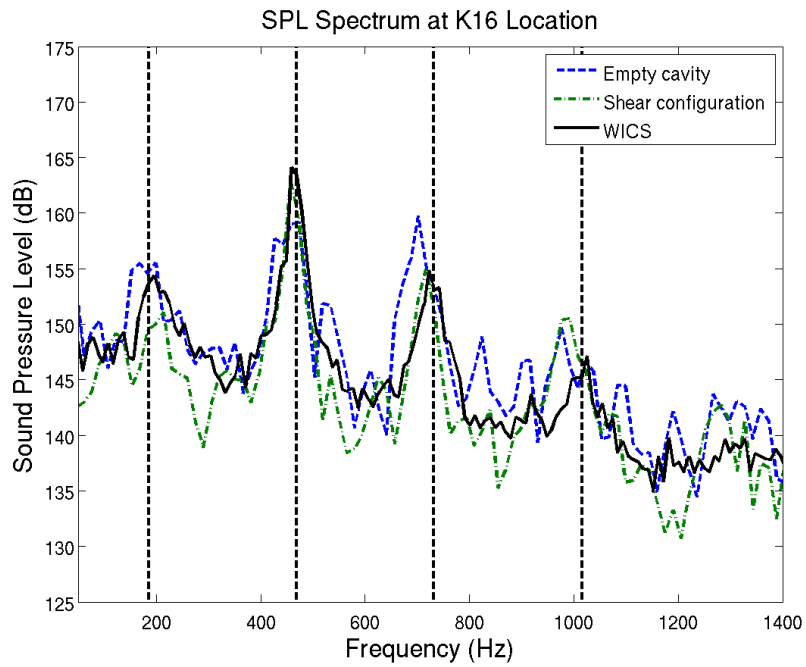


Figure 60: SPL spectrum at the K16 transducer location for the shear configuration

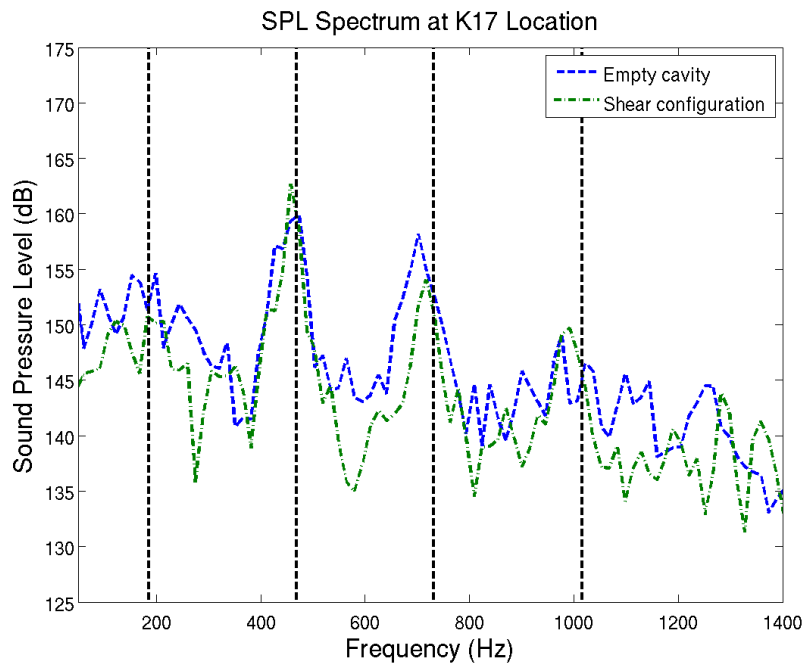


Figure 61: SPL spectrum at the K17 transducer location for the shear configuration

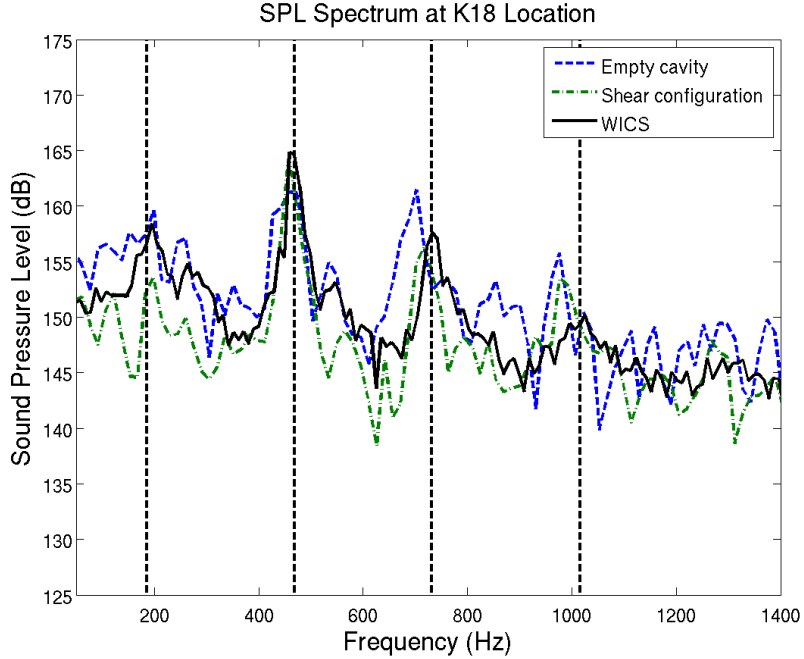


Figure 62: SPL spectrum at the K18 transducer location for the shear configuration

Pseudo-Schlieren images from the centerline of the empty cavity are shown in Fig. 63. The images are taken starting at an arbitrary time  $t$  with snapshots at  $4.8 \times 10^{-4}$  s intervals, representing one-quarter of a cycle for the predominant cavity mode of 460 Hz. Here the store clearly interacts with the shear layer. The shear layer is forced to flow around the store, although the vortical structures generally remain intact and continue to flow downstream where they eventually stagnate at the aft cavity wall. The vortex shedding/cavity response cycle is largely unimpeded despite the presence of the store in the shear layer. This observation supports the findings that the pressure spectra are relatively unchanged from the empty cavity configuration. There does appear to be some deflection of the shear layer in snapshot (d), wherein the store causes the shear layer to flow down and out of the cavity on an intermittent basis. This deflection of the flow would explain the slightly lower cavity noise levels observed at the K18 transducer at low frequencies.

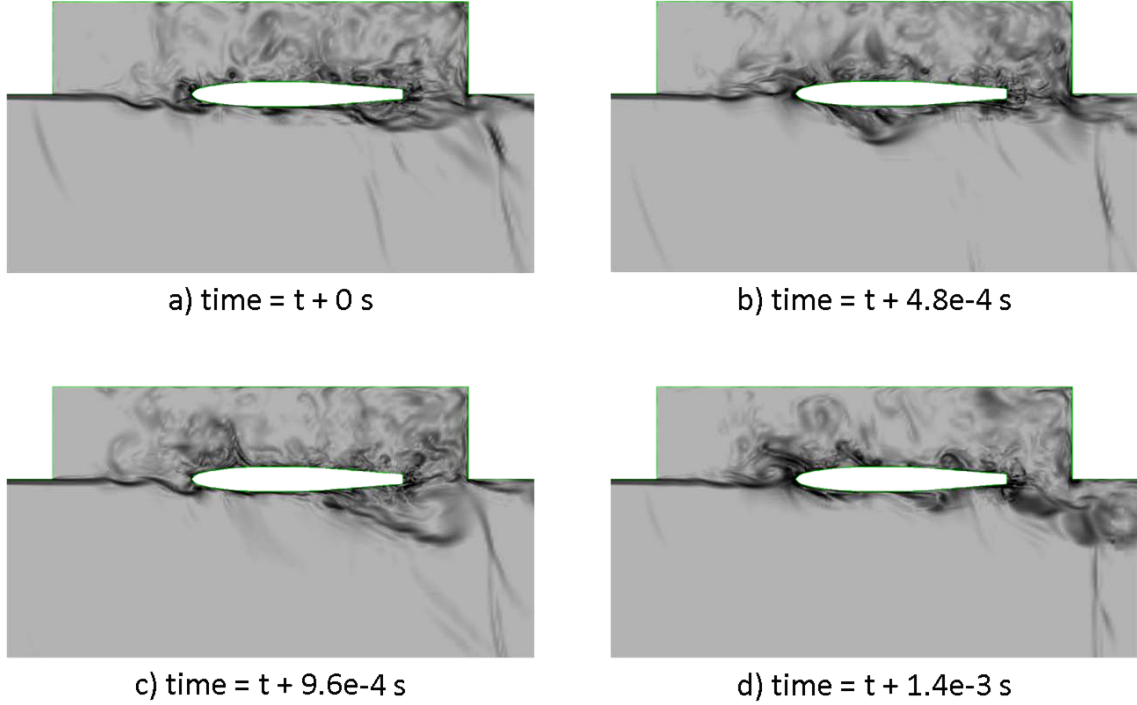


Figure 63: Pseudo-Schlieren images of shear configuration

The SPL spectra for the sidewall locations are plotted in Figs. 64 and 65. Again, these results are plotted against the spectra from the empty cavity. As with the four transducer locations, these spectra show good correlation with the empty cavity and exhibit the same trends. Namely, the third mode for the shear configuration better corresponds to the observed frequency from the WICS experimental data than the empty cavity, the fourth mode at the L01 location is more clearly defined in the shear configuration, and the amplitude of the first peak at the L02 location is predicted to be lower in the shear configuration than the empty cavity.

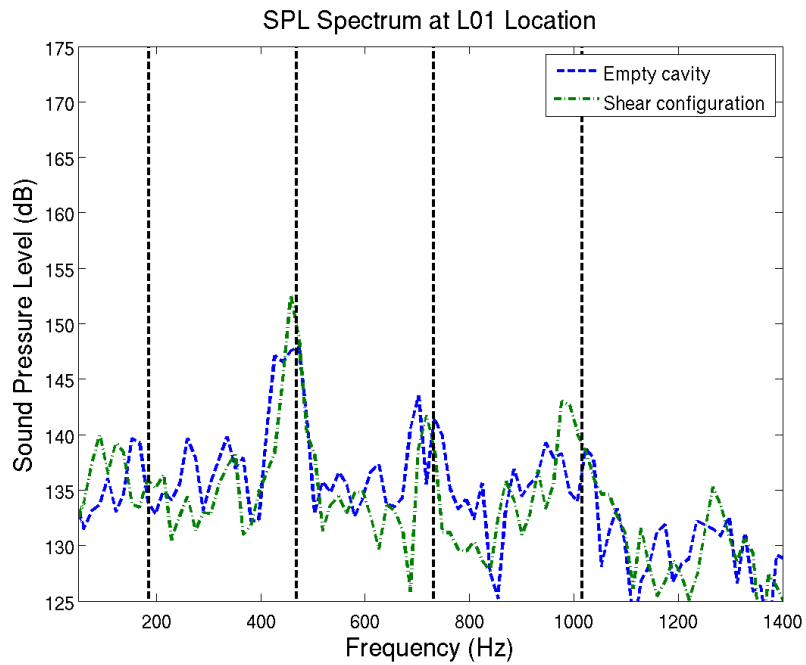


Figure 64: SPL spectrum at the L01 location for the shear configuration

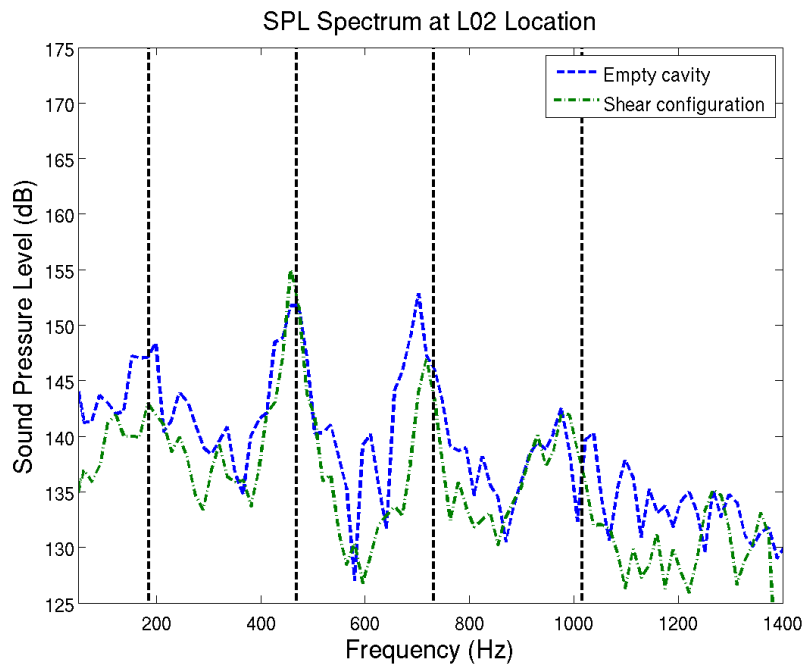


Figure 65: SPL spectrum at the L02 transducer location for the shear configuration

The force and moment histories on the store are plotted against time in Figs. 66 and 67. These time histories exhibit the same general characteristics as those for the carriage configuration. The mean and standard deviation for each of the forces and moments are summarized in Table 9. The dominant force on the store is the longitudinal force imposed on the store. There is also a significant force in the vertical direction. There is essentially no lateral force on the store. The dominant moment is a pitch up moment and there is also a fluctuating roll moment, although this is centered about the x-axis. There is effectively no yaw moment present on the store.

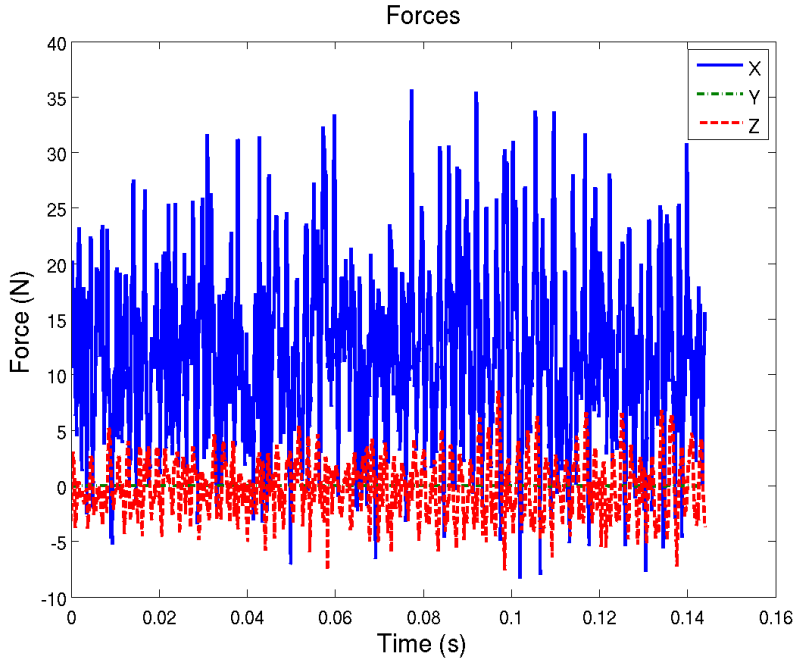


Figure 66: Force time history for the store in the shear configuration

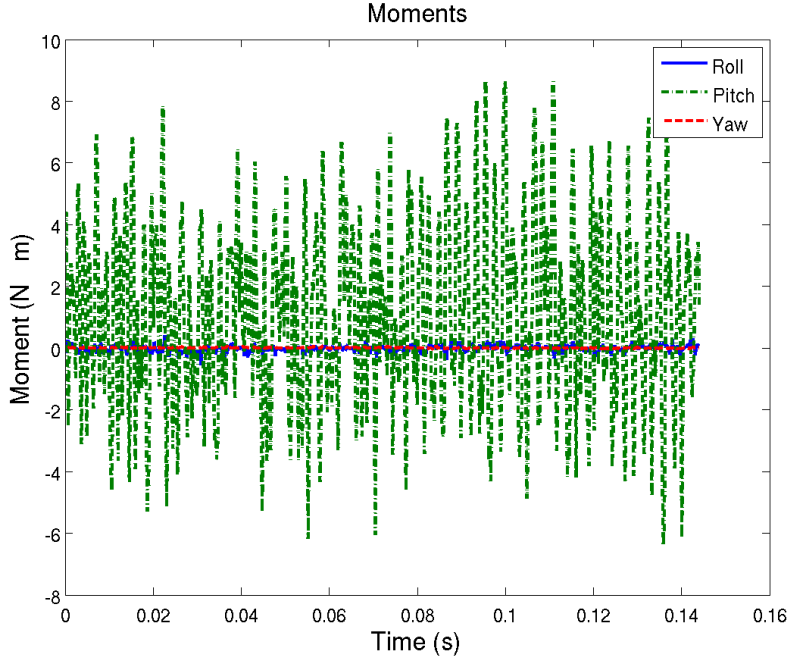


Figure 67: Moment time history for the store in the shear configuration

Table 9: Summary of store forces and moments in shear configuration

|                    | Mean Value | Standard Deviation |
|--------------------|------------|--------------------|
| Longitudinal force | 11.19 N    | 7.67 N             |
| Lateral force      | 0.00 N     | 0.01 N             |
| Vertical force     | -0.37 N    | 2.52 N             |
| Roll moment        | -0.02 N·m  | 0.10 N·m           |
| Pitch moment       | 0.73 N·m   | 2.87 N·m           |
| Yaw moment         | 0.00 N·m   | 0.01 N·m           |

The time-averaged pressure coefficient along the top and bottom of the store are presented in Fig. 68. The pressures at the top and bottom of the store are almost equal along the entire length of the store. This distribution is a consequence of the symmetry of the store and both surfaces essentially seeing the same flow. There is a high pressure at the nose of the store from the approaching shear layer, but the pressures over most of the store are almost equal to the freestream. This is markedly different from the pressure distribution seen on the store in the carriage position. Table 10 summarizes the average pressure coefficient differential, the center of pressure, and the store's

center of mass. As with the store in the carriage configuration, a pitch-up moment is observed, although the mechanism here is different. There is a net upward force acting at a point ahead of the center of mass that creates the pitch-up moment. Note that with the center of pressure ahead of the center of gravity, the store is unstable here.

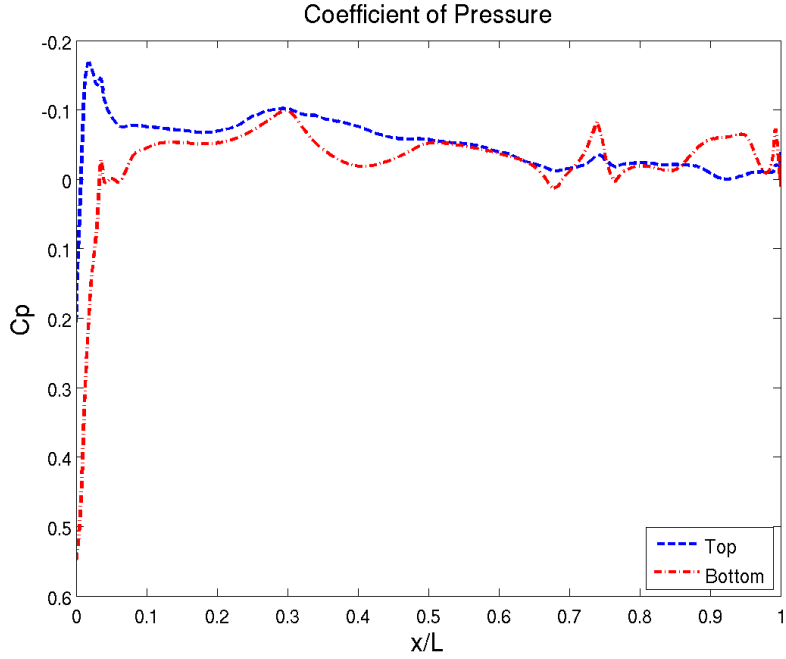


Figure 68: Pressure coefficient on top and bottom of store in shear configuration

Table 10: Average pressure differential, center of pressure, and center of mass for the store in shear configuration

| Average Pressure Differential<br>$C_{P,top} - C_{P,bottom}$ | Center of Pressure<br>$x/L$ | Center of Mass<br>$x/L$ |
|---|-----------------------------|-------------------------|
| -0.047  | -0.078                      | 0.459                   |

The mean and standard deviation of the longitudinal force and pitch moment between the carriage and shear configurations are compared in Table 11. The forces and moments on the store are greater in the carriage position than in the shear layer. The carriage configuration data is also more variant, indicating a wider range of fluctuations. This observation initially seems counter-intuitive since greater pitch-up

behavior has typically been observed to occur as a released store approaches the shear layer. However, this can be explained when the store's stability is taken into consideration. As the store travels downward in the cavity, it transitions from a stable to an unstable configuration as the center of pressure moves forward. Although the store experiences higher moments early in the trajectory, its stable configuration makes it more resistant to pitching. As the store transitions to an unstable configuration, however, the store is less able to self-correct and the pitching moment may be more readily observed in the trajectory of the store.

Table 11: Comparison of store forces and moments between carriage and shear configurations

|                    | Carriage configuration |                    | Shear configuration |                    |
|--------------------|------------------------|--------------------|---------------------|--------------------|
|                    | Mean                   | Standard Deviation | Mean                | Standard Deviation |
| Longitudinal force | 14.00 N                | 9.33 N             | 11.19 N             | 7.67 N             |
| Vertical force     | -0.55 N                | 2.23 N             | -0.37 N             | 2.52 N             |
| Pitch moment       | 1.16 N-m               | 2.98 N-m           | 0.73 N-m            | 2.87 N-m           |

The longitudinal and vertical force spectra are plotted alongside the K16 transducer spectrum in Figs. 69 and 70. The force spectra are plotted on a logarithmic scale in order to match the scaling with the cavity ceiling SPL. The force spectra show a strong correlation to the pressure fluctuations on the cavity ceiling and similar trends that were observed in the carriage configuration are present here, although the correlation with the longitudinal force spectrum is not as strong here as in the carriage configuration. The first four modes as observed on the cavity ceiling are also apparent in the store forces. The relative amplitudes of the peaks from the broadband noise levels also correlate. The pitch and roll moment spectra are also plotted alongside the K16 transducer spectrum in Figs. 71 and 72. As with the force spectra, the moment spectra are plotted on a logarithmic scale. Again, note that the pitch and roll moments are plotted on different scales and differ by about three orders of magnitude. The pitch moment spectrum shows a very strong correlation to the K16

SPL spectrum. The modal frequencies and the peak relative amplitudes match very well with the K16 SPL. The roll moment spectrum does not show any correlation to the K16 spectrum. None of the cavity modes are present in the roll moment data.

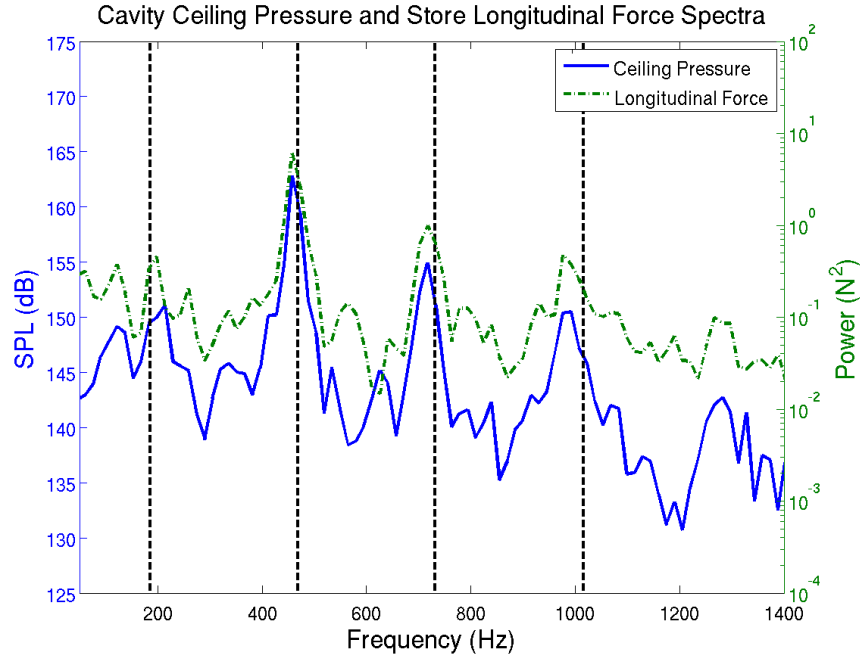


Figure 69: Store longitudinal force frequency spectrum (right axis) and K16 transducer SPL spectrum (left axis) for shear configuration

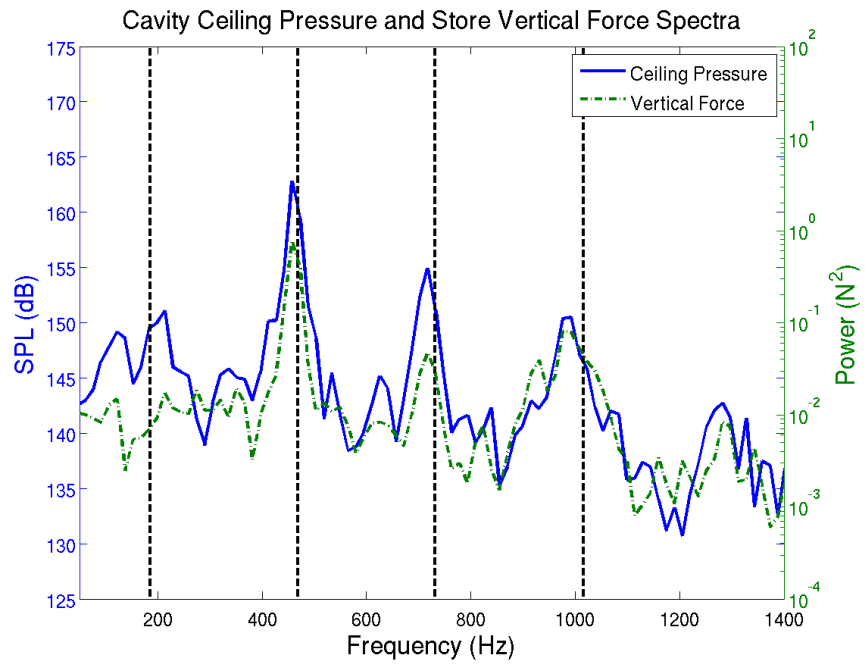


Figure 70: Store vertical force frequency spectrum (right axis) and K16 transducer SPL spectrum (left axis) for shear configuration

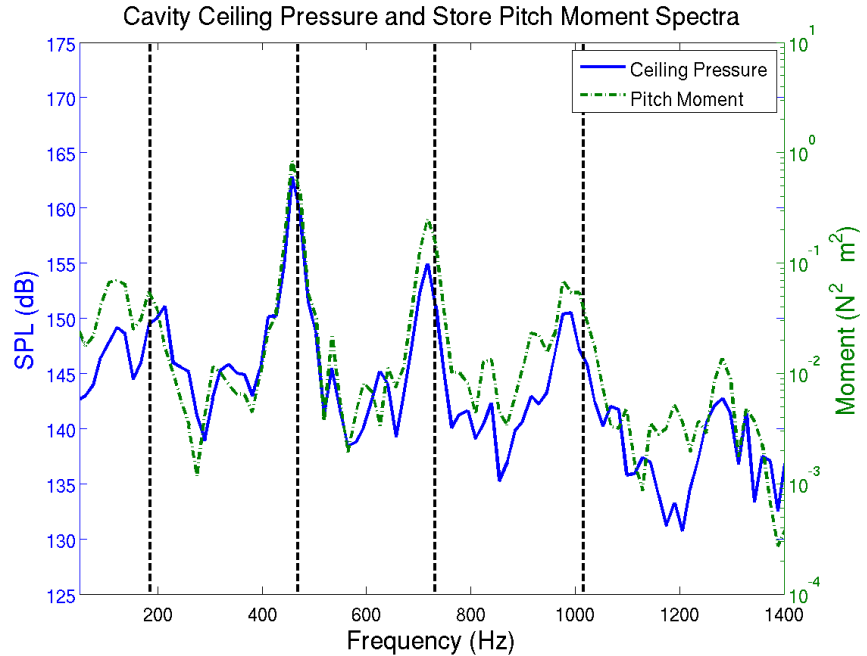


Figure 71: Store pitch moment frequency spectrum (right axis) and K16 transducer SPL spectrum (left axis) for shear configuration

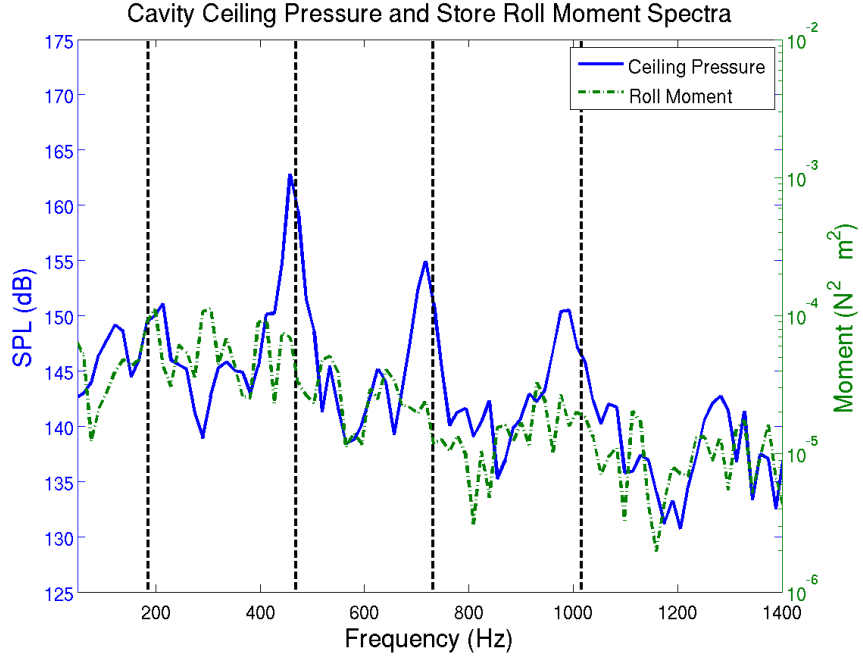


Figure 72: Store roll moment frequency spectrum (right axis) and K16 transducer SPL spectrum (left axis) for shear configuration

The SPL spectra on the surface of the store are presented in Figs. 73 through 75. Each of the figures presents the SPL spectra at a given longitudinal position on the store. The pressure spectra at each longitudinal position correlate well with each other. At  $x/L = 0.25$ , the second, third, and fourth modes are clearly present with the second mode being the dominant frequency. The first mode is present, although it is located at 122 Hz, which is lower than the first mode observed on the cavity ceiling. At  $x/L = 0.50$ , the second and third modes are clearly evident, although here the second and third modes are roughly equivalent in amplitude. At the  $x/L = 0.75$  location, the first, third, and fourth modes are present. As with the  $x/L = 0.25$  location, the first mode is predicted at a frequency lower than observed on the cavity ceiling. These are essentially the same trends that were observed in the carriage configuration. While the characteristics of the mean flow are seen to differ between the two positions, the characteristics of the turbulence in these locations correspond very well, as they are driven by the vortex shedding and cavity fluid response which defines the flow throughout the entire cavity.

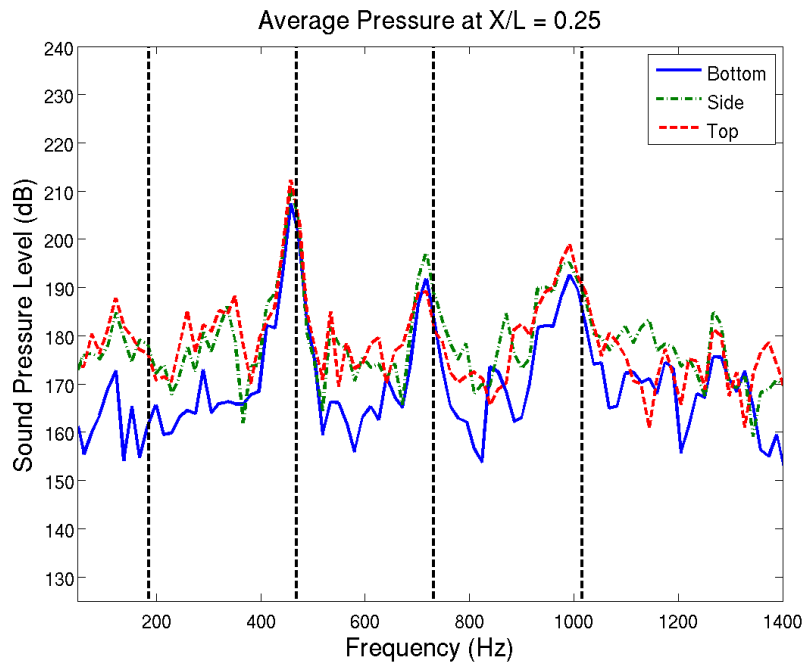


Figure 73: SPL spectra on store body at  $x/L = 0.25$  for shear configuration

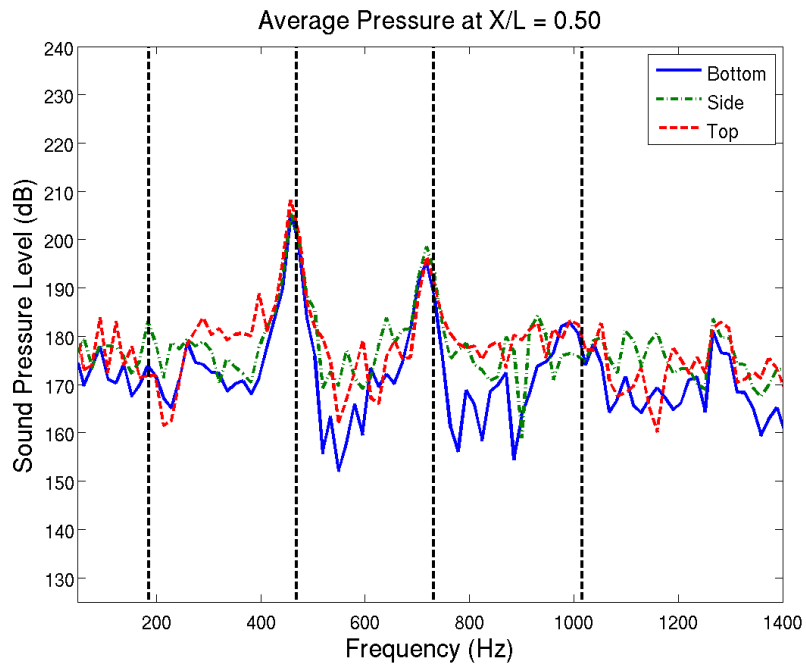


Figure 74: SPL spectra on store body at  $x/L = 0.50$  for shear configuration

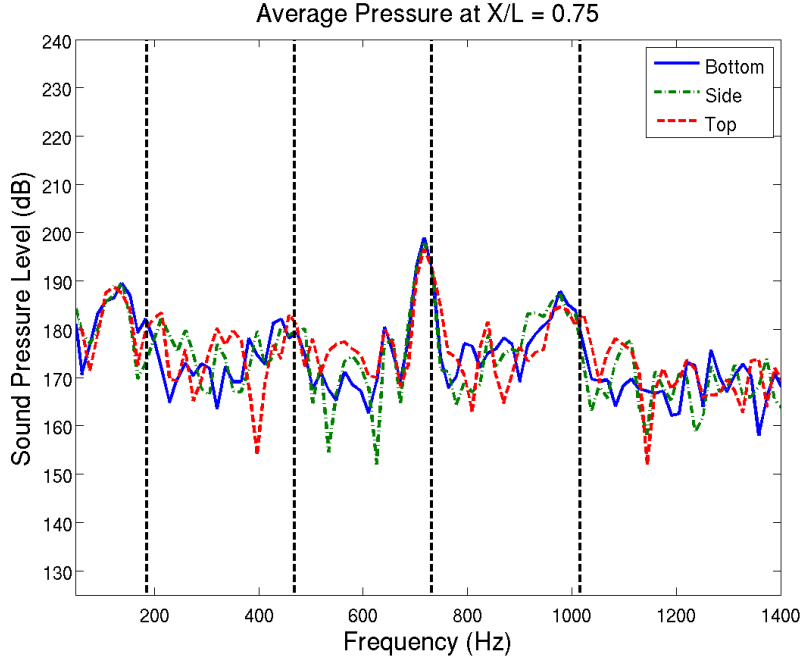


Figure 75: SPL spectra on store body at  $x/L = 0.75$  for shear configuration

The same vibrational modes which are observed in the empty cavity are also present for the cavity with a store in the shear layer. Although previous experiments have shown that a store located close to the cavity leading edge can act as a suppressor, it is shown here that if the weapon is sufficiently far from the cavity leading edge, it will not have an effect on the acoustic response of the cavity. A comparison of the cavity surface pressure fluctuations and the store force and moment loadings shows correlation between the longitudinal force, vertical force, and pitch moment with the cavity vibrational modes. The dominant moment on the store in the shear location is a pitch-up moment. The pressure fluctuations on the store in the cavity vary by longitudinal position and correlate between circumferential position at a given longitudinal position. The cavity response and store force/moment loading for this configuration are consistent with what was observed for the carriage configuration.

#### 4.4 Cavity with Store in Forward Shear Configuration

The results for the forward shear configuration are presented here. The overall characteristics of the flow are not greatly different from the two configurations presented earlier, although there are notable differences.

The time averaged velocity vectors along the cavity centerline are shown in Fig. 76. They are colored by Mach number. As with the shear configuration, the presence of the store forces the shear layer to split as the flow travels around the top and bottom of the store, reforming behind the store. Unlike in the shear configuration, however, the store is upstream far enough such that the shear layer is still able to spread out before reaching the aft cavity wall. In this way, the time-averaged flow much resembles that of the empty cavity and the carriage configuration.

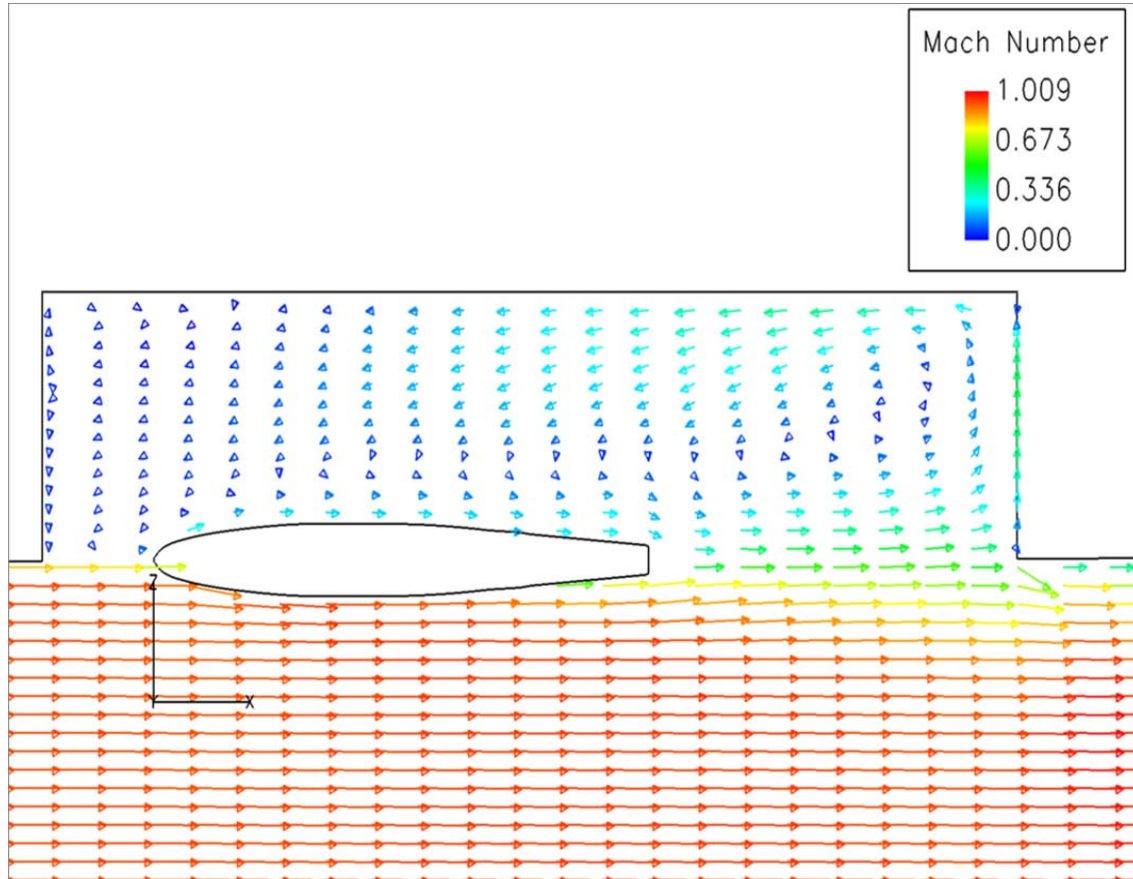


Figure 76: Time averaged velocity vectors for the forward shear configuration (colored by Mach number)

The SPL spectra for the four transducer locations are plotted against the empty cavity results in Figs. 77 through 80. The vertical dashed lines correspond to the frequencies of the first four modes as predicted by the Rossiter equation. Generally speaking, the forward shear configuration shows good agreement with the empty cavity data in frequency and amplitude prediction at all four transducer locations. As with the carriage and shear configurations, the forward shear configuration shows a peak at 732 Hz for the third mode, which corresponds with the location of the third peak in the WICS data. This configuration shows better matching with the WICS empty cavity data in the amplitude of the second and third modes at all transducer locations; specifically the amplitude of the second mode is predicted higher and the amplitude of the third mode is predicted lower than the empty cavity solution. One significant difference is that the amplitude of the fourth mode is greatly increased at the K12, K16, and K17 locations. Also, in the K12 location, there is now a distinct peak at the first mode. The overall noise levels are in agreement with the empty cavity solution across all transducer locations, which indicates that the store is not acting as a suppressor in this situation.

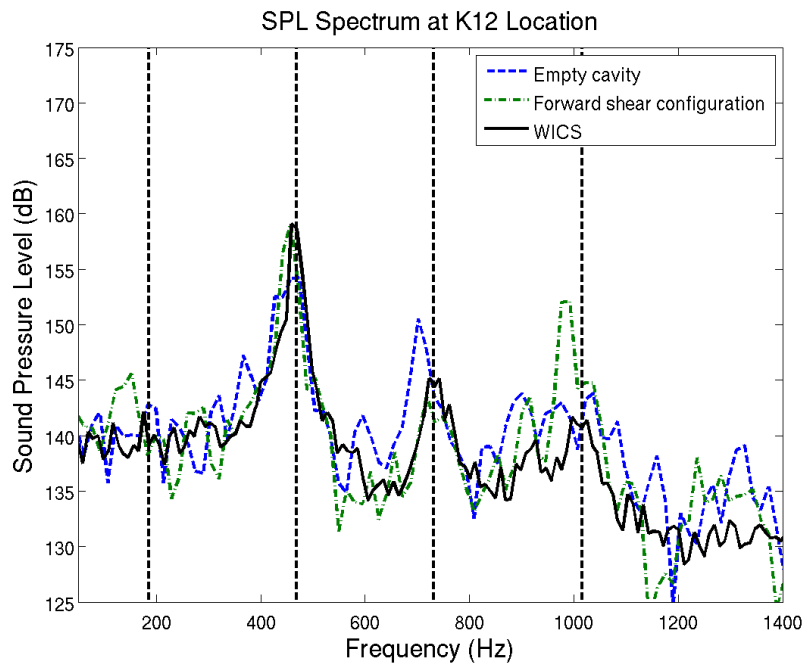


Figure 77: SPL spectrum at the K12 transducer location for the forward shear configuration

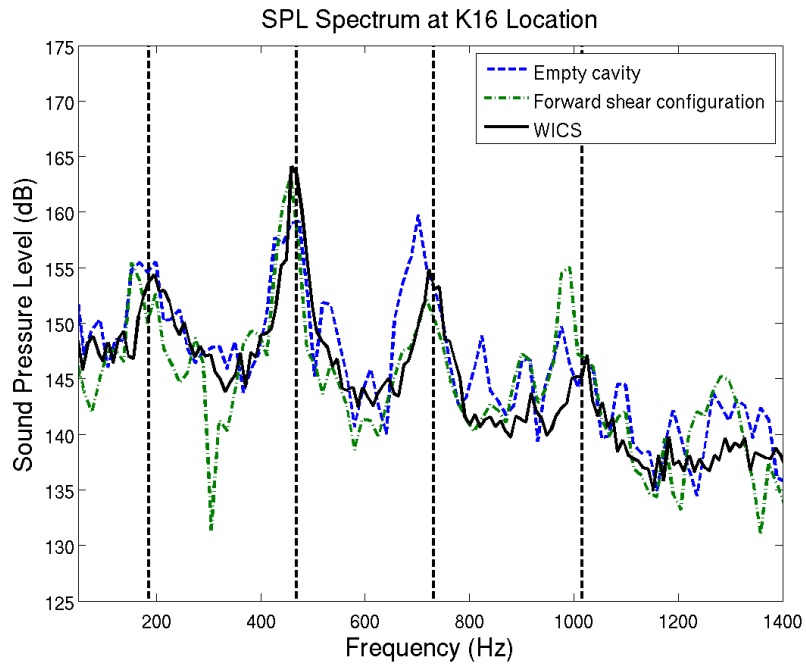


Figure 78: SPL spectrum at the K16 transducer location for the forward shear configuration

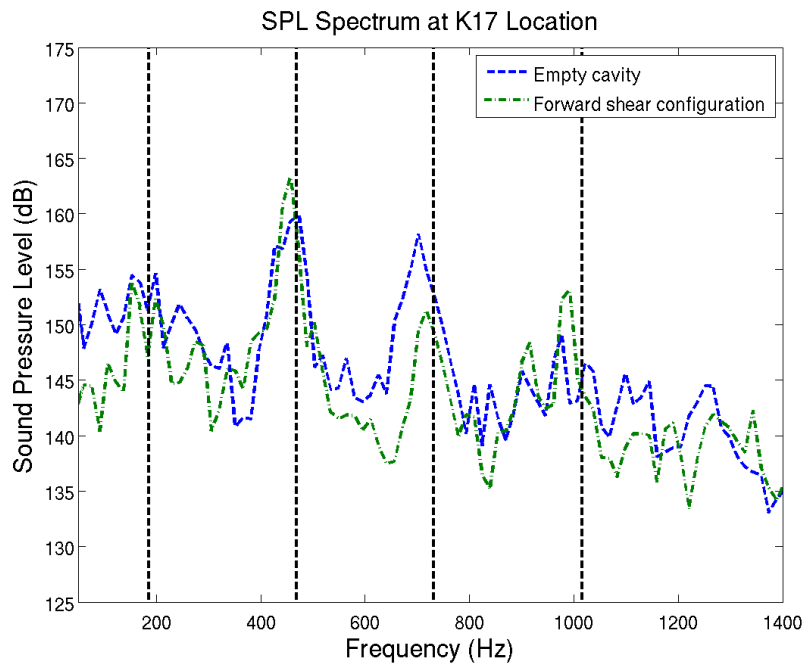


Figure 79: SPL spectrum at the K17 transducer location for the forward shear configuration

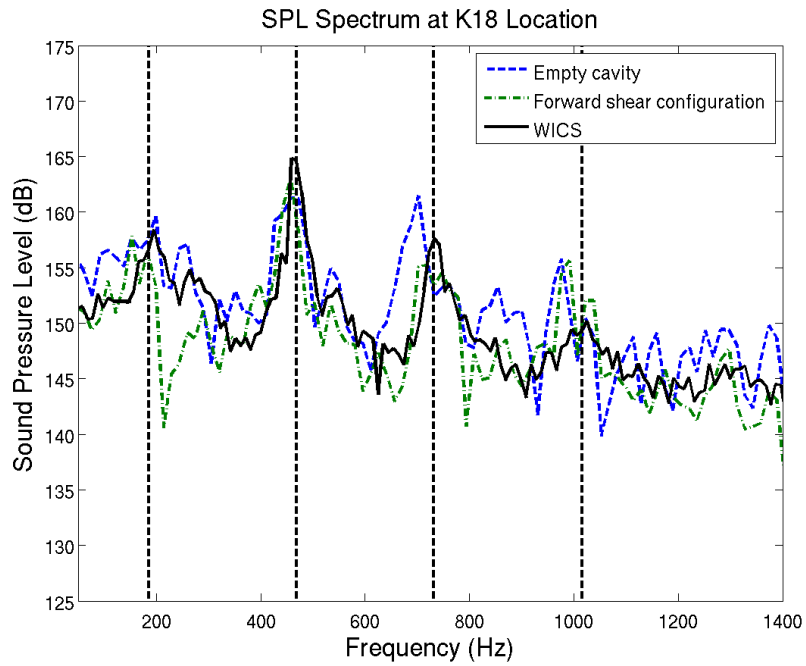


Figure 80: SPL spectrum at the K18 transducer location for the forward shear configuration

Pseudo-Schlieren images from the centerline of the empty cavity are shown in Fig. 81. The images are taken starting at an arbitrary time  $t$  with snapshots at  $4.8 \times 10^{-4}$  s intervals, representing one-quarter of a cycle for the predominant cavity mode of 460 Hz. Here, as with the shear configuration, the store clearly interacts with the shear layer. The shear layer is forced to flow around the store, although the vortical structures generally remain intact and continue to flow downstream where they eventually stagnate at the aft cavity wall. With the store located sufficiently upstream, there is ample time for the shear layer to reform behind the store, and the vortex shedding/cavity response cycle is largely unimpeded despite the presence of the store in the shear layer. This further supports the findings that the pressure spectra are relatively unchanged from the empty cavity configuration. It also fails to support earlier observations that a store located in the shear layer acts to suppress the vortex shedding/acoustic response cycle [5]. The stores used in the AFFDL experiment were cylindrical with an ogive nosecone and were longer relative to the overall cavity length than the store model used here. Furthermore, the exact configurations for which a suppressive effect was observed, including positioning of the store, are not detailed. Just as different spoiler designs have been shown to have different effectiveness in the suppression of vibrations, the exact store shape, size, and positioning would be expected to have differing effects on the fluid cavity response studied here.

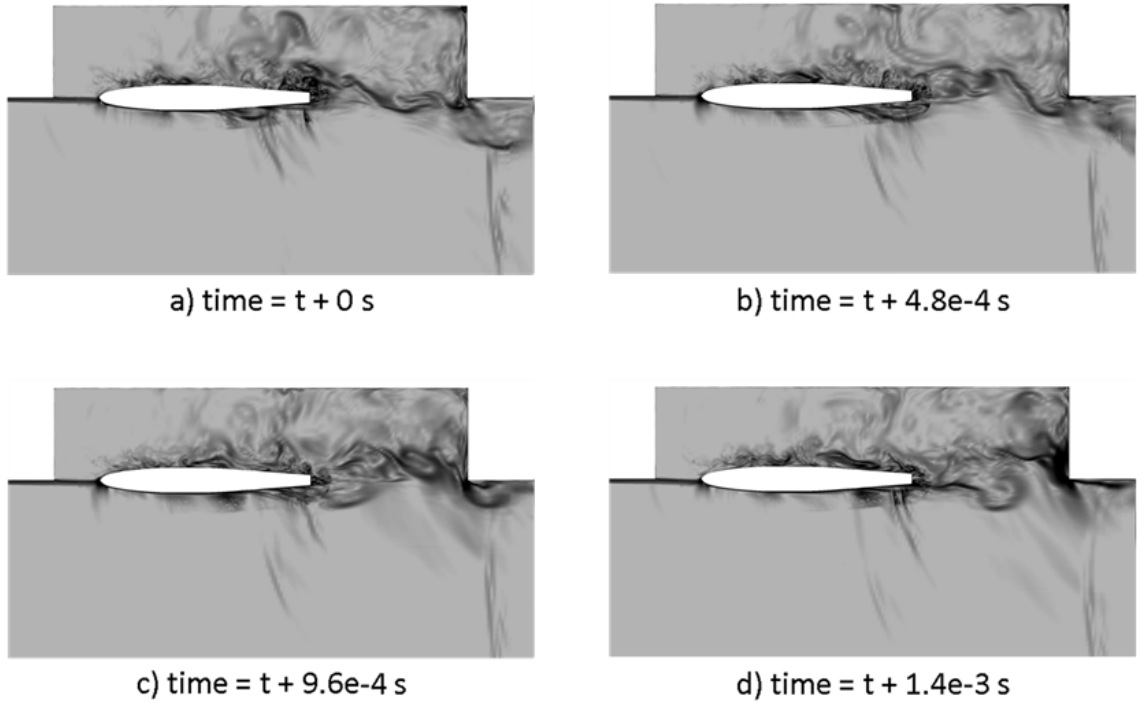


Figure 81: Pseudo-Schlieren images of forward shear configuration

The SPL spectra for the sidewall locations are plotted in Figs. 82 and 83. Again, these results are plotted against the spectra from the empty cavity. Similar trends as were observed with the four transducer locations are observed in these spectra. Namely, the amplitude of the second mode is predicted higher than the empty cavity, the amplitude of the third mode is predicted lower than the empty cavity, and the amplitude of the fourth mode is predicted to increase from the empty cavity solution. As with the empty cavity solution, there appears to be no discernable first mode at the L02 location.

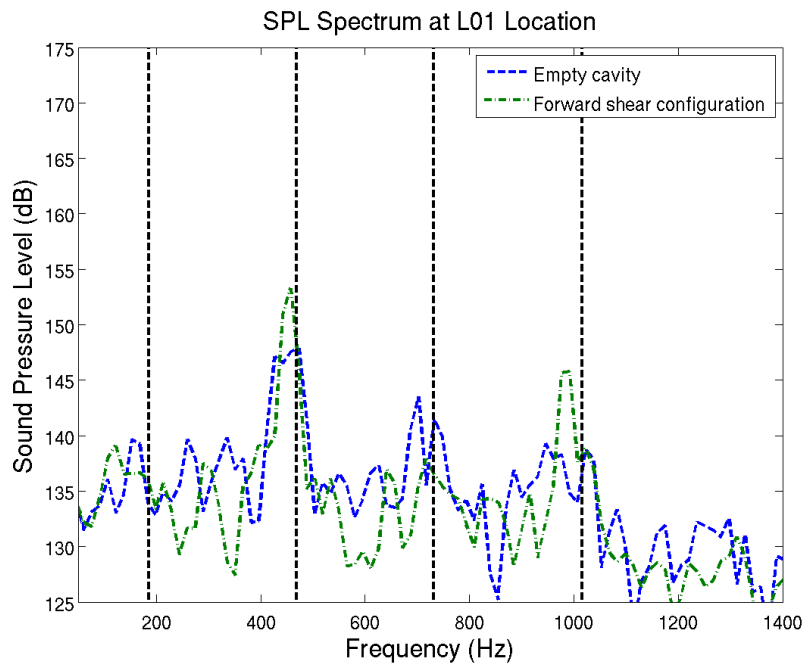


Figure 82: SPL spectrum at the L01 location for the forward shear configuration

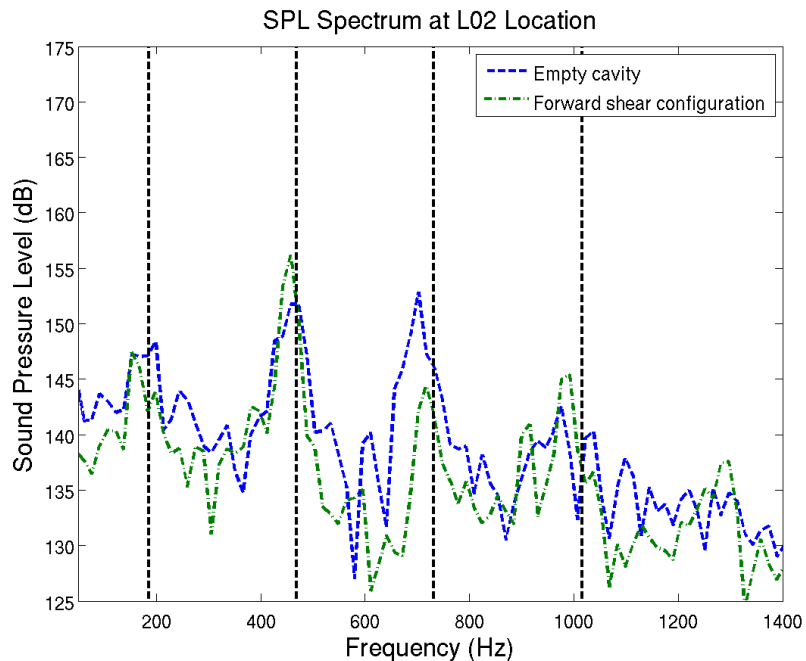


Figure 83: SPL spectrum at the L02 transducer location for the forward shear configuration

The force and moment histories on the store are plotted against time in Figs. 84 and 85. These time histories exhibit the same general characteristics as those for the carriage and shear configurations. The mean and standard deviation for each of the forces and moments are summarized in Table 12. The dominant force on the store is the longitudinal force imposed on the store. There is also a significant force in the vertical direction. There is essentially no lateral force on the store. The dominant moment is a pitch up moment and there is also a fluctuating roll moment, although this is centered about the x-axis. There is effectively no yaw moment present on the store.

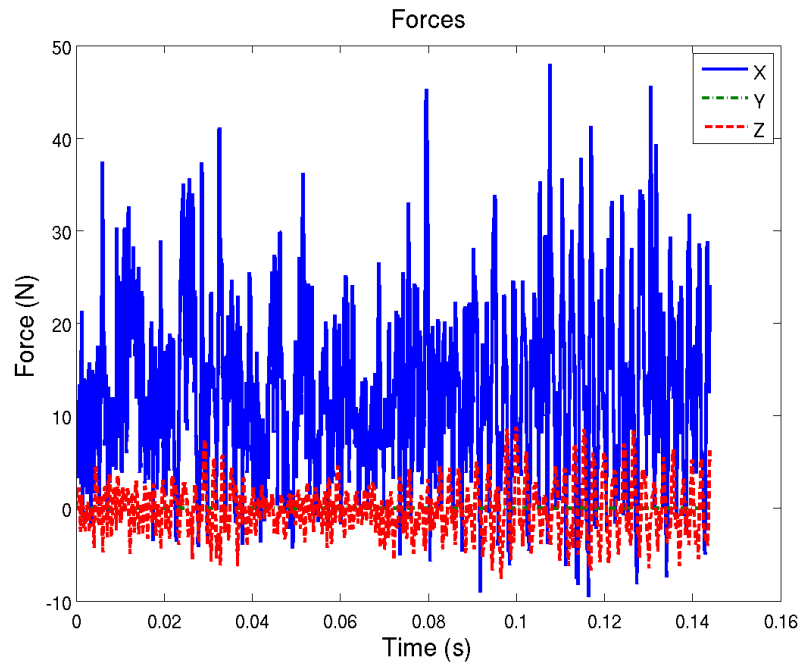


Figure 84: Force time history for the store in the forward shear configuration

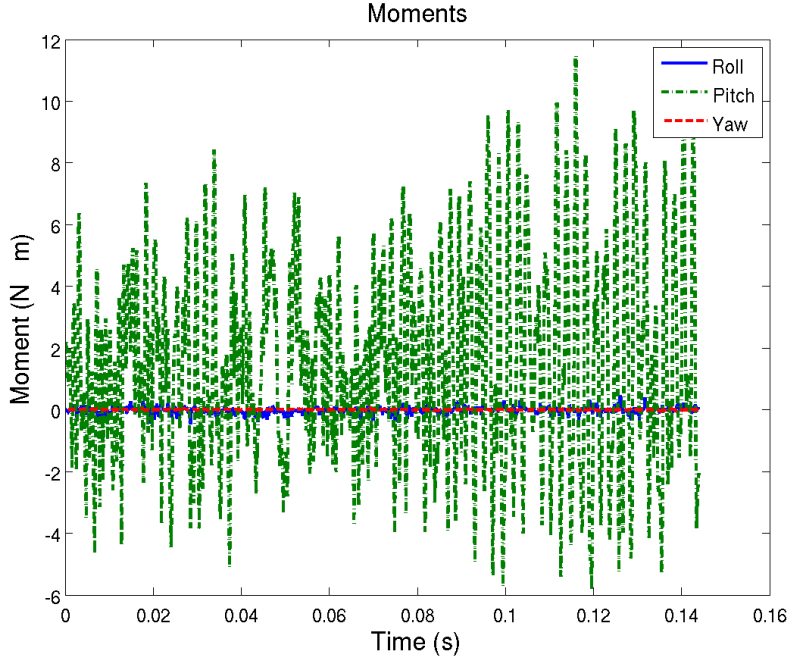


Figure 85: Moment time history for the store in the forward shear configuration

Table 12: Summary of store forces and moments in forward shear configuration

|                    | Mean Value | Standard Deviation |
|--------------------|------------|--------------------|
| Longitudinal force | 11.64 N    | 9.01 N             |
| Lateral force      | 0.00 N     | 0.01 N             |
| Vertical force     | -0.38 N    | 2.68 N             |
| Roll moment        | -0.02 N·m  | 0.10 N·m           |
| Pitch moment       | 1.14 N·m   | 3.17 N·m           |
| Yaw moment         | 0.00 N·m   | 0.01 N·m           |

The time-averaged pressure coefficient along the top and bottom of the store are presented in Fig. 86. It looks remarkably similar to the shear configuration. The pressures at the top and bottom of the store are almost equal along the entire length of the store. The pressure coefficient along the bottom of the store shows the same fluctuations at the same longitudinal positions on the store as the solution from the shear configuration. One distinguishing difference is that here the coefficients of pressure increase slightly as distance towards the tail of the store increases, whereas in the shear configuration they showed a slightly decreasing trend. Table 13 sum-

marizes the average pressure coefficient differential, the center of pressure, and the store's center of mass. The pitch-up mechanism here is similar to that of the shear configuration, although here the pressure differential is greater, resulting in a higher pitch-up moment.

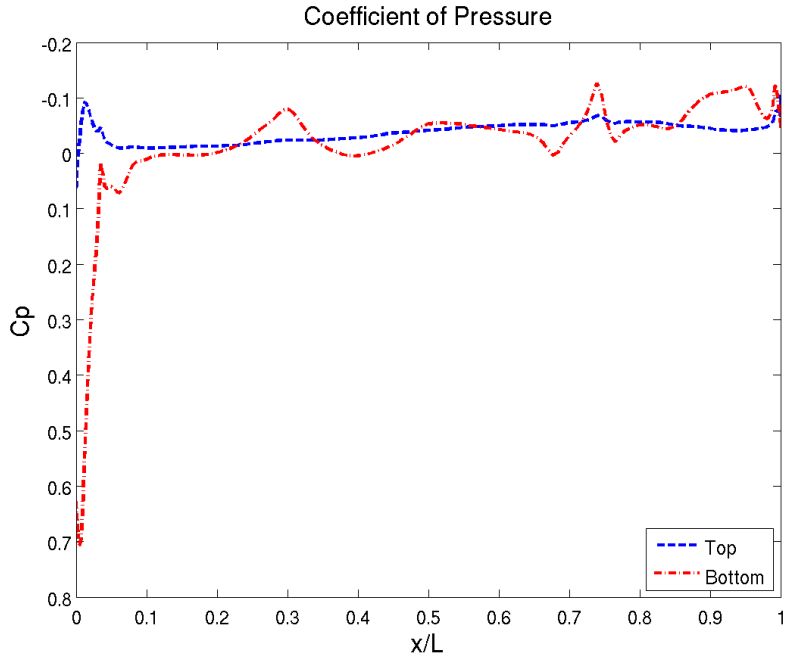


Figure 86: Pressure coefficient on top and bottom of store in forward shear configuration

Table 13: Average pressure differential, center of pressure, and center of mass for the store in forward shear configuration

| Average Pressure Differential<br>$C_{P,top} - C_{P,bottom}$ | Center of Pressure<br>x/L | Center of Mass<br>x/L |
|---|---------------------------|-----------------------|
| -0.136  | -0.055                    | 0.459                 |

The mean and standard deviation of the longitudinal force and pitch moment between the two shear configurations are compared in Table 14. The forces on the store are about equivalent in both cases, although the forward shear configuration experiences a greater pitch up moment.

Table 14: Comparison of store forces and moments between shear configurations

|                    | Shear configuration |                    | Forward shear configuration |                    |
|--------------------|---------------------|--------------------|-----------------------------|--------------------|
|                    | Mean                | Standard Deviation | Mean                        | Standard Deviation |
| Longitudinal force | 11.19 N             | 7.67 N             | 11.64 N                     | 9.01 N             |
| Vertical force     | -0.37 N             | 2.52 N             | -0.38 N                     | 2.68 N             |
| Pitch moment       | 0.73 N-m            | 2.87 N-m           | 1.14 N-m                    | 3.17 N-m           |

The longitudinal and vertical force spectra are plotted alongside the K16 transducer spectrum in Figs. 87 and 88. The force spectra are plotted on a logarithmic scale in order to match the scaling with the cavity ceiling SPL. The force spectra show a strong correlation to the pressure fluctuations on the cavity ceiling. The solutions here show about the same correlation to the ceiling fluctuations as were observed in the shear configuration. The first four modes as observed on the cavity ceiling are apparent in the store forces. The relative amplitudes of the peaks from the broadband noise levels also correlate. The pitch and roll moment spectra are also plotted alongside the K16 transducer spectrum in Figs. 89 and 90. As with the force spectra, the moment spectra are plotted on a logarithmic scale. Again, note that the pitch and roll moments are plotted on different scales and differ by about three orders of magnitude. As was observed in the carriage and shear configurations, the pitch moment spectrum shows a very strong correlation to the K16 SPL spectrum. The modal

frequencies and the peak relative amplitudes match very well with the K16 SPL. The roll moment spectrum does not show any correlation to the K16 spectrum. None of the cavity modes are present in the roll moment data.

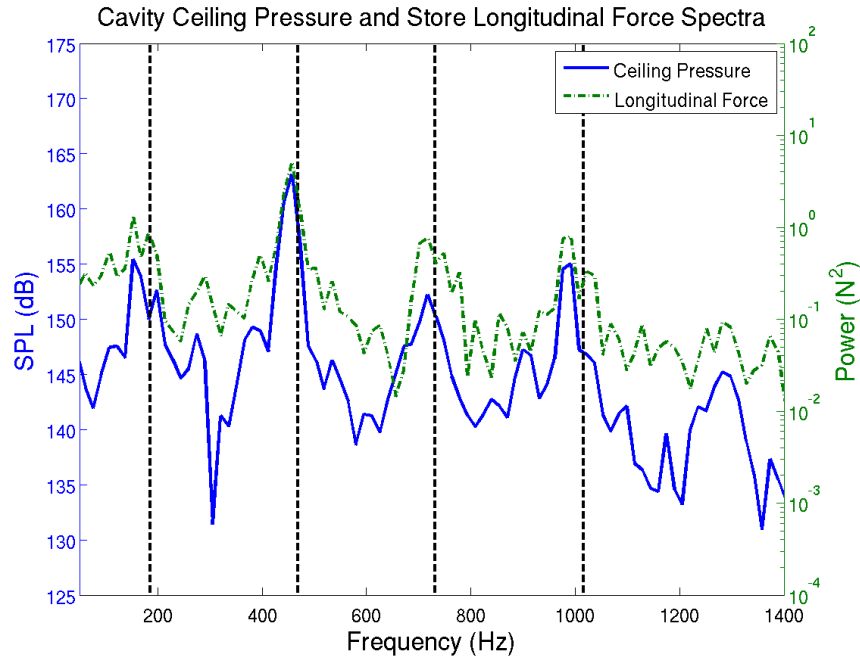


Figure 87: Store longitudinal force frequency spectrum (right axis) and K16 transducer SPL spectrum (left axis) for forward shear configuration

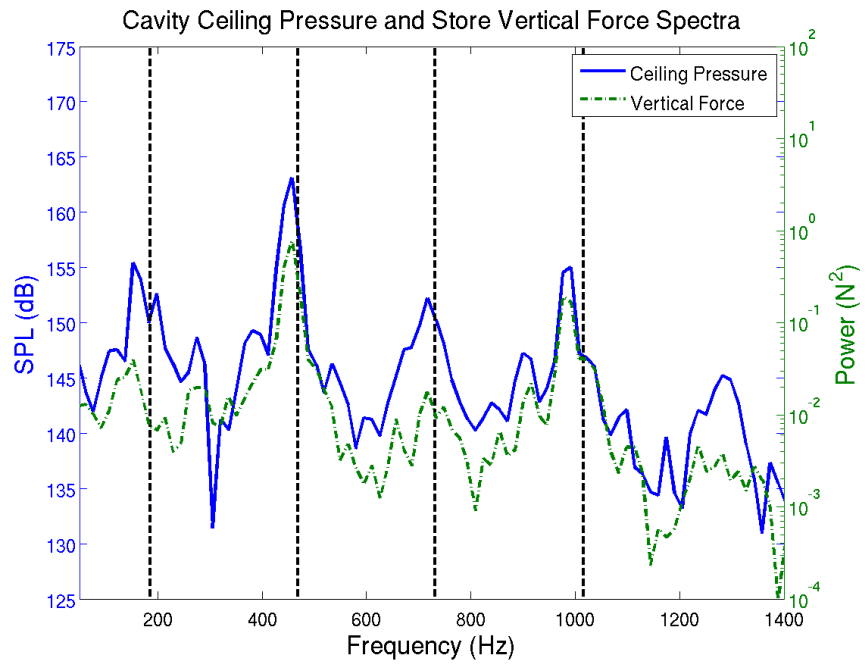


Figure 88: Store vertical force frequency spectrum (right axis) and K16 transducer SPL spectrum (left axis) for forward shear configuration

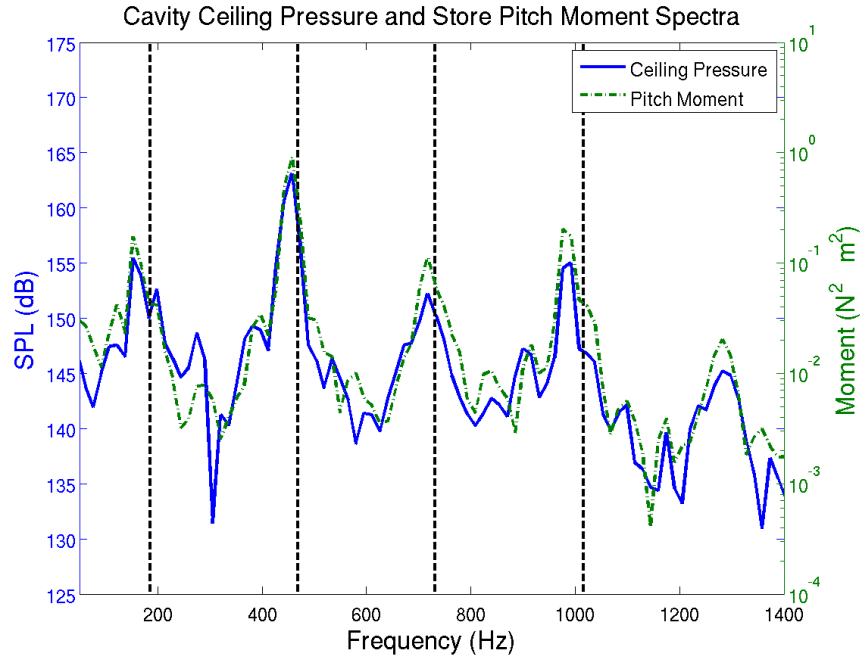


Figure 89: Store pitch moment frequency spectrum (right axis) and K16 transducer SPL spectrum (left axis) for forward shear configuration

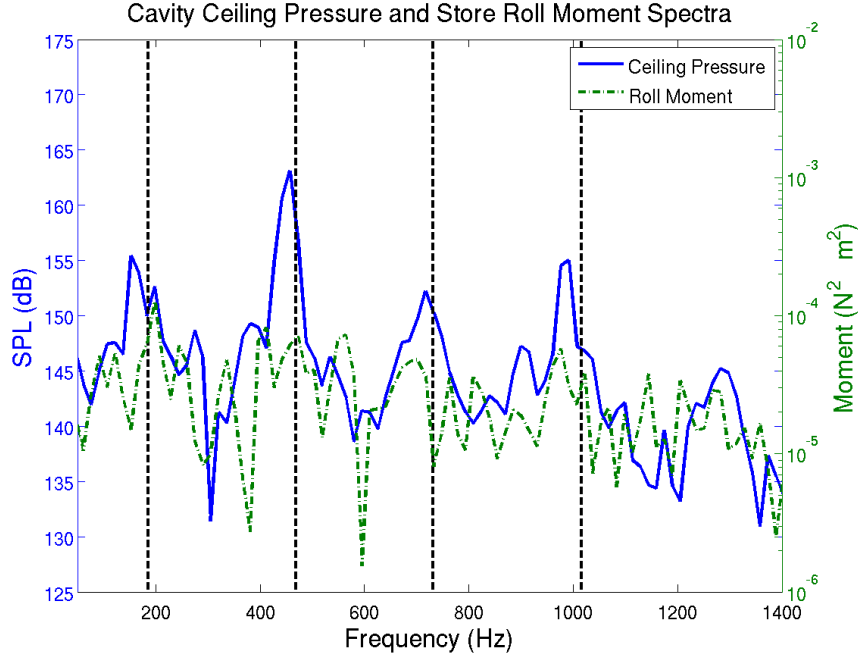


Figure 90: Store roll moment frequency spectrum (right axis) and K16 transducer SPL spectrum (left axis) for forward shear configuration

The SPL spectra on the surface of the store are presented in Figs. 91 through 93. Each of the figures presents the SPL spectra at a given longitudinal position on the store. The pressure spectra at each longitudinal position correlate well with each other. At  $x/L = 0.25$ , all four modes are clearly present with the fourth mode being the dominant frequency. At  $x/L = 0.50$ , all four modes are still clearly evident, although here the second, third, and fourth modes are roughly equivalent in amplitude. At the  $x/L = 0.75$  location, the first, third, and fourth modes are present, although the third mode is greatly diminished here and the second mode is the dominant mode. The first mode here is not observable. It is also of note that at all three positions, the bottom and side pressure data correspond well in overall sound levels, however only at  $x/L = 0.75$  does the SPL at the top of the store corresponds with the other two locations. Here, though, all three positions correspond very well with each other. Note that the carriage and shear configurations showed similar trends in the pressure loading across the store. These same trends are not observed here. This observation

suggests that the turbulent characteristics of the flow vary mainly with longitudinal, rather than vertical, position in the cavity.

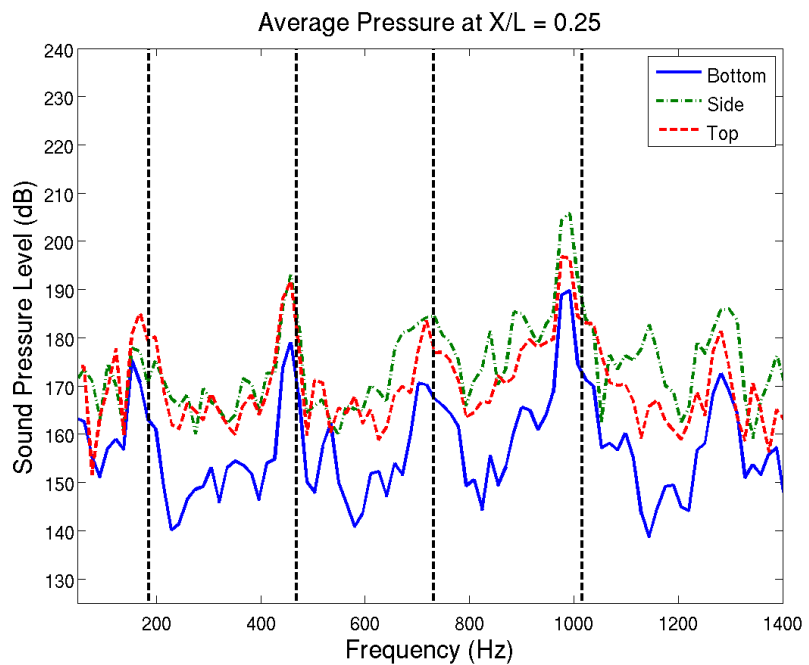


Figure 91: SPL spectra on store body at  $x/L = 0.25$  for forward shear configuration

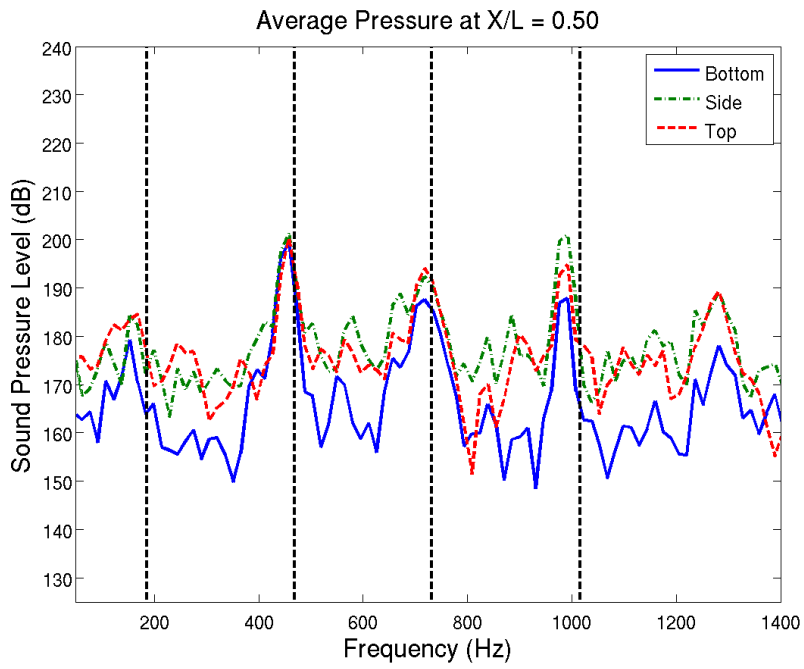


Figure 92: SPL spectra on store body at  $x/L = 0.50$  for forward shear configuration

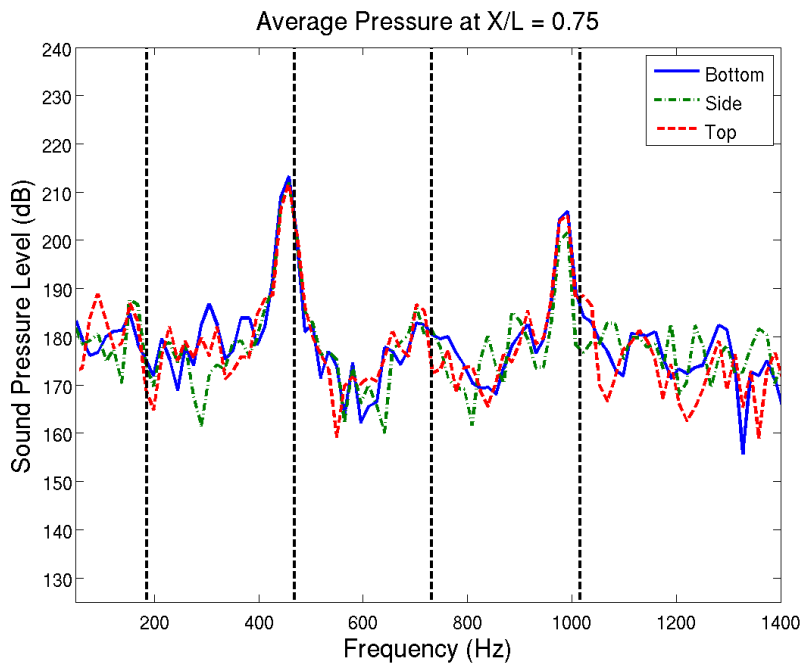


Figure 93: SPL spectra on store body at  $x/L = 0.75$  for forward shear configuration

The same vibrational modes which are observed in the empty cavity are also present for the cavity with a store located upstream in the shear layer. Although previous experiments have shown that a store located close to the cavity leading edge can act as a suppressor, such an effect was not observed here. In fact, the response at higher frequency modes was observed to increase in this configuration. The suppression effect previously observed is likely reliant on the store overall shape, size, and position. A comparison of the cavity surface pressure fluctuations and the store force and moment loadings shows correlation between the longitudinal force, vertical force, and pitch moment with the cavity vibrational modes. The dominant moment on the store in the forward shear location is a pitch-up moment. The pressure fluctuations on the store in the cavity vary by longitudinal position and correlate between circumferential position at a given longitudinal position. The cavity response and store force/moment loading for this configuration are consistent with what was observed for the previous two configurations.

## V. Conclusions

A computational investigation was completed in order to investigate the relationship between the acoustic modes of a cavity in grazing flow and the relationship of these modes to the force and moment loading of a store located in the cavity. A cavity of  $L/D = 4.5$  with freestream flow at  $M = 0.95$  was investigated. Three configurations with a store present were investigated and compared to an empty cavity: one configuration with the store located in the carriage position and two configurations with the store located in the shear layer. Several conclusions can be drawn from the results of this study.

First and foremost, it was demonstrated that the force and moment loading on the store correlate to the pressure fluctuations on the cavity surface. Specifically, the longitudinal force, vertical force, and pitch moment exhibited fluctuations at the same frequencies as the cavity resonant modes and showed peaks at similar noise levels relative to the broadband noise as the cavity ceiling and wall pressure fluctuations. The other forces and moments were essentially zero-valued and showed random fluctuations. This correlation holds for the store regardless of position within the cavity. The turbulent fluctuations observed throughout the cavity are consistent. A variation in turbulent fluctuations was not observed with a change in vertical position when longitudinal position was kept constant, and the same fluctuations were observed in the shear layer as well as within the cavity itself. Essentially, the store integrated unsteady loads correlate to the acoustic modes of the cavity.

For the cases observed here, the presence of the store in the cavity did not fundamentally alter the acoustic response that was observed in the cavity. In the three configurations investigated here, the vortex shedding process and the cavity fluid response were largely unimpeded by the presence of the store. This observation further aids the store separation engineer since it implies that the characterization of an empty cavity can be used for the analysis of the separation of entire classes of stores from that cavity. There is some evidence, though, that the presence of the store may have deflected some of the flow down and out of the cavity, which affected the

low-frequency response at the aft wall. A suppression of cavity vibrations due to the presence of a store in the shear layer was not observed here. Even in the forward shear configuration, the overall noise levels and the peak amplitudes were not diminished. It is expected that this effect depends greatly on specific store geometry and position.

Previous studies measured pressure data only along the cavity centerline with the intent of measuring the longitudinal modes of the cavity. Here, data was taken on the sidewalls as well. These data did not provide any evidence of any significant lateral modes for this geometry. The frequency spectra on the sidewalls showed the same acoustic modes as those on the cavity ceiling and aft wall. Additionally, the frequency content on the sidewall locations correspond well to the corresponding longitudinal locations on the cavity ceiling and to the pressure fluctuations along the store. Higher overall sound levels and more low frequency oscillations are observed at downstream locations compared to upstream locations. The observed modes are dependent on cavity geometry, but for deep cavities with the characteristic length in the direction of the flow, the longitudinal modes dominate the acoustic response in the cavity.

Finally, it was shown that the overall force and moment loading on a store in a cavity are a total cavity phenomenon. In other words, the same forces and moments which are significant in the carriage position are also significant in the shear layer. Most significantly, it was observed here that the released store is subjected to a pitch-up moment from the instant it is released from carriage. This moment loading is a result of the mean flow in the cavity; the pitch-up moment is not merely a result of the store penetrating the shear layer. However, since the mean flow throughout the cavity is not uniform, the mechanisms which create the force and moment loading are not consistent throughout the cavity. There is evidence to suggest that the center of pressure of the store shifts forward as it moves downward through the cavity, and the store transitions from a stable configuration to an unstable one as a result. The behavior of a store as it is released from a cavity may be better explained not by a change in the overall force and moment loading on the store as it enters the shear

layer, but rather a change in response to the store loading brought on by a change in aerodynamic stability.

### **5.1 Future Work**

The results and conclusions presented here open the door for future areas of research.

The configurations investigated here are representative of only one cavity geometry with one store loadout. Additional studies are necessary to fully characterize the many different configurations which exist. A store which is relatively larger compared to the cavity might create a situation where the store's presence affects the cavity's native response. Asymmetric weapon loadouts could also significantly affect the flow within the cavity. It was also observed that the turbulence levels and frequencies vary within the cavity based upon longitudinal position. A further investigation into the cavity response and store force and moment loading for different cavity geometry/store combinations is necessary to fully understand this problem. An in-depth study investigating the effect of varying store sizes, shapes, and position within the cavity is warranted.

A more robust study of store stability within the cavity needs to be conducted. The observations from this research indicate that the flow conditions within a cavity can cause a store which is initially stable to become unstable as it exits the cavity. A better understanding of this transition is necessary in order to be able to properly predict its effect on a store's trajectory. A store stability analysis can be accomplished through a combination of static solutions where the position of the store is varied as well as with dynamic cases where a trajectory is simulated and the pressure distributions and center of pressure are calculated throughout the trajectory. Fully understanding this phenomenon is crucial in order to develop techniques to maintain safe and acceptable separation of cavity-released stores.

It has been demonstrated that the force and moment loading on a store in a cavity correlate to the acoustic modes of the cavity. The effects of this relationship on a released store's separation characteristics need to be examined. This would be done by investigating the change in a store's trajectory as various parameters are altered, including time of release and store mass and inertial properties. As the effects of the store loading/acoustic mode relationship are better understood, a predictive capability can be better developed.

Investigation into realistic aircraft cavity geometries need to be conducted. Although much can be learned from generalized geometries about the fundamental processes at work, geometries which are representative for operational aircraft need to be studied in order for this knowledge to be transferable to real-world applications.

## *Appendix A. OVERFLOW Namelist Parameters*

This appendix tabulates the significant OVERFLOW namelist parameters that were used for this research. These are provided as a reference so that the solutions here can be easily recreated for future research. The inputs are divided into sections that mimic the same groupings of variables as the OVERFLOW 2.1 User's Guide [18]. For any variable not listed in Tables 15 through 23, the OVERFLOW 2.1 default value is used.

Table 15: Summary of Global OVERFLOW (\$GLOBAL) inputs

| Parameter   | Value    |
|-------------|----------|
| NSTEPS      | 10000    |
| RESTRT      | .F.      |
| NSAVE       | 200      |
| ISTART_QAVG | 1000     |
| NQT         | 205      |
| NQC         | 0        |
| MULTIG      | .F.      |
| FMG         | .T.      |
| FMGCYC      | 150, 150 |
| NITNWT      | 5        |
| FSONWT      | 2        |
| DTPHYS      | 1.93     |

Table 16: Summary of Global OVERFLOW-D (\$OMIGLB) inputs

| Parameter | Value |
|-----------|-------|
| DYNMCS    | .F.   |
| I6DOF     | 2     |
| IRUN      | 0     |
| NADAPT    | 0     |
| LFRINGE   | 3     |

Table 17: Summary of OVERFLOW DCF (\$DCFGLB) inputs

| Parameter | Value |
|-----------|-------|
| DQUAL     | 0.2   |
| MORFAN    | 1     |
| NORFAN    | 13    |

Table 18: Summary of load balance (\$GROUPS) inputs

| Parameter | Value  |
|-----------|--------|
| WGHTNB    | 2.0    |
| IGSIZE    | 500000 |
| MAXNB     | 0      |
| MAXGRD    | 0      |

Table 19: Summary of flow parameter (\$FLOINP) inputs

| Parameter | Value   |
|-----------|---------|
| ALPHA     | 0.0     |
| BETA      | 0.0     |
| FSMACH    | 0.95    |
| GAMINF    | 1.4     |
| REY       | 20833.3 |
| PR        | 0.72    |
| PRT       | 0.9     |
| TINF      | 518.67  |

Table 20: Summary of numerical method selection (\$METPRM) inputs

| Parameter | Value |
|-----------|-------|
| ILHS      | 6     |
| IRHS      | 5     |
| ILIMIT    | 4     |

Table 21: Summary of time accuracy (\$TIMACU) inputs

| Parameter | Value |
|-----------|-------|
| ITIME     | 0     |
| DT        | 0.0   |
| TFOSO     | 1.0   |

Table 22: Summary of smoothing parameter (\$SMOACU) inputs

| Parameter | Value |
|-----------|-------|
| DELTA     | 1.1   |
| FSO       | 5     |

Table 23: Summary of viscous and turbulence modeling (\$VISINP) inputs

| Parameter | Value |
|-----------|-------|
| VISC      | .T.   |
| IDES      | 2     |
| IRC       | 0     |
| WALLFUN   | .T.   |

## *Appendix B. Summary of Computational Expense of Solutions*

This appendix summarizes the computational expense for the OVERFLOW 2.1 solutions conducted during this research. In cases where solutions were computed on differing computer systems, the system used is also noted. Additional commentary is also provided.

An overview of the computational expense of the main solutions are presented in Table 24. These solutions were all computed on the AFIT local cluster.

Table 24: Computational Cost of Cavity Simulations

|                             | Number of cells | Cores Used | Wall Time (hrs) | CPU Time (cpu · hrs) |
|-----------------------------|-----------------|------------|-----------------|----------------------|
| Empty cavity                | 5,172,360       | 50         | 53.5            | 2677                 |
| Carriage configuration      | 9,357,596       | 28         | 156             | 4368                 |
| Shear configuration         | 9,357,596       | 30         | 165             | 4950                 |
| Forward shear configuration | 9,357,596       | 50         | 96.1            | 4804                 |

The computational expense for each of the solutions computed for the Newton subiteration study are displayed in Table 25. The percent change is calculated using zero subiterations as the baseline. There is a slight decrease in cost when using one subiteration compared to zero subiterations. Using five subiterations increases the computational cost by almost 5 times and using 10 subiterations increases the computational cost by almost 10 times from the baseline. This increased expense makes it critical to use the fewest number of subiterations necessary for an accurate answer in order to minimize the computational cost of computing the solutions.

Table 25: Comparison of Computational Cost for Varying Number of Subiterations

|                  | Cores Used | Wall Time (hrs) | CPU Time (cpu · hrs) | % Change |
|------------------|------------|-----------------|----------------------|----------|
| 0 subiterations  | 30         | 14.4            | 431                  | —        |
| 1 subiteration   | 50         | 7.0             | 351                  | -18.6%   |
| 5 subiterations  | 30         | 78.4            | 2352                 | 446%     |
| 10 subiterations | 50         | 92.7            | 4637                 | 976%     |

The computational expense for each of the solutions computed for the grid resolution study are displayed in Table 26. The percent change is calculated using

the medium grid as the baseline. The medium grid actually took more computational time to run than the fine grid, despite having fewer grid points. The additional run time is likely due to the fact that the medium grid solution was run on the AFIT local cluster whereas the coarse and fine grid solutions were run on the Air Force Research Laboratory Department of Defense Supercomputing Resource Center (AFRL DSRC) system, which means the comparison between these solutions is not direct. The AFRL DSRC system is faster than the AFIT cluster, which is why the fine grid solution was able to be completed in less computational time than the medium grid solution even though it had more points overall.

Table 26: Comparison of Computational Cost for Grid Resolution Study

|             | Number of cells | Cores Used | Wall Time (hrs) | CPU Time (cpu · hrs) | % Change | System |
|-------------|-----------------|------------|-----------------|----------------------|----------|--------|
| Coarse grid | 4,650,360       | 50         | 35.4            | 1771                 | -33.8%   | DSRC   |
| Medium grid | 5,172,360       | 50         | 53.5            | 2677                 | —        | AFIT   |
| Fine grid   | 6,476,760       | 50         | 50.2            | 2508                 | -6.3%    | DSRC   |

The computational expense for each of the solutions computed for the grid resolution study are displayed in Table 27. The percent change is calculated using  $dt = 1.6 \times 10^{-5}$  s as the baseline. As with the grid sensitivity solution, a direct comparison between the cost of these solutions cannot be made. The smaller and larger time steps were run on the AFRL DSRC, whereas the medium time step was run on the AFIT cluster. A comparison between the small and large time step shows, however, that the choice of time step does not affect the computational cost of the solution.

Table 27: Comparison of Computational Cost for Time Step Sensitivity Study

| dt (s)               | Cores Used | Wall Time (hrs) | CPU Time (cpu · hrs) | % Change | System |
|----------------------|------------|-----------------|----------------------|----------|--------|
| $8.0 \times 10^{-6}$ | 50         | 38.9            | 1943                 | -27.5%   | DSRC   |
| $1.6 \times 10^{-5}$ | 50         | 53.5            | 2677                 | —        | AFIT   |
| $4.0 \times 10^{-5}$ | 50         | 39.0            | 1951                 | -27.1%   | DSRC   |

## Bibliography

1. Cattafesta, L., Williams, D., Rowley, C., and Alvi, F., "Review of Active Control of Flow-Induced Cavity Resonance," *33rd AIAA Fluid Dynamics Conference*, June 2003, AIAA 2003-3567.
2. Cenko, A., Deslandes, R., Dillenius, M., and Stanek, M., "Unsteady Weapon Bay Aerodynamics—Urban Legend or Flight Clearance Nightmare," *46th AIAA Aerospace Sciences Meeting and Exhibit*, January 2008, AIAA 2008-0189.
3. Westmoreland, W., "Trajectory Variation Due to an Unsteady Flow-Field," *47th AIAA Aerospace Sciences Meeting Including the New Horizons Forum and Aerospace Exposition*, January 2009, AIAA 2009-550.
4. Nelson, C. and Cain, A., "Prediction of Store Trajectory Response to Unsteady Aerodynamic Loads," *47th AIAA Aerospace Sciences Meeting Including the New Horizons Forum and Aerospace Exposition*, January 2009, AIAA 2009-548.
5. Heller, H., Holmes, G., and Covert, E., "Flow-Induced Pressure Oscillations in Shallow Cavities," Tech. rep., Air Force Flight Dynamics Laboratory, 1970, Technical Report AFFDL-TR-70-104.
6. Dix, R. and Dobson, T., "Database for Internal Store Carriage and Jettison," Tech. rep., Arnold Engineering Development Center, 1990, Technical Report AEDC-TR-90-23, Vol. 1.
7. Rockwell, D. and Naudasher, E., "Review—Self-Sustaining Oscillations of Flow Past Cavities," June 1978.
8. Rossiter, J., "Wind-Tunnel Experiments on the Flow Over Rectangular Cavities at Subsonic and Transonic Speeds," *Aeronautical Research Council Reports and Memoranda*, October 1964, Technical Report 3438.
9. Grace, S., "An Overview of Computational Aeroacoustic Techniques Applied to Cavity Noise Prediction," *39th AIAA Aerospace Sciences Meeting and Exhibit*, January 2001, AIAA 2001-0510.
10. Plentovich, E., "Three-dimensional Cavity Flow Fields at Subsonic and Transonic Speeds," Tech. rep., NASA Langley Research Center, 1992, Tech. Rep. TM 4209.
11. Dix, R. and Bauer, R., "Experimental and Predicted Acoustic Amplitudes in a Rectangular Cavity," *38th Aerospace Sciences Meeting and Exhibit*, January 2000, AIAA 2000-0472.
12. Srinivasan, S. and Baysal, O., "Navier-Stokes Calculations of Transonic Flows Past Cavities," *Journal of Fluids Engineering*, Vol. 113, September 1991, pp. 368–376.

13. Peng, S., "Unsteady RANS Simulation of Turbulent Cavity Flow: Summary of 2D Baseline Computations," Tech. rep., Systems Technology, 2005, ISSN-1650-1942.
14. Nichols, R., "Comparison of Hybrid Turbulence Models for a Circular Cylinder and a Cavity," *AIAA Journal*, Vol. 44, No. 6, 2006, pp. 1207–1219.
15. Tramel, R., Nichols, R., and Buning, P., "Addition of Improved Shock-Capturing Schemes to OVERFLOW 2.1," *19th AIAA Computational Fluid Dynamics Conference*, June 2009, AIAA 2009-3988.
16. Nichols, R., "A Comparison of Hybrid RANS/LES Turbulence Models for a Generic Weapons Bay With and Without a Spoiler," *26th AIAA Applied Aerodynamics Conference*, 2008, AIAA 2008-6229.
17. Nichols, R., Tramel, R., and Buning, P., "Solver and Turbulence Model Upgrades to OVERFLOW2 for Unsteady and High-Speed Applications," *25th AIAA Applied Aerodynamics Conference*, June 2006, AIAA 2006-2824.
18. Buning, P. and Nichols, R., *User's Manual for OVERFLOW 2.1*, August 2008.
19. Harris, F., "On the Use of Windows for Harmonic Analysis with the Discrete Fourier Transform," *Proceedings of the IEEE*, Vol. 66, January 1978.
20. Welch, P., "The Use of Fast Fourier Transform for the Estimation of Power Spectra: A Method Based on Time Averaging Over Short, Modified Periodograms," *IEEE Transactions on Audio and Electroacoustics*, Vol. AU-15, June 1967.

## *Vita*

Captain Christopher J. Coley graduated from Highlands Ranch High School in Highlands Ranch, Colorado. He entered undergraduate studies at the University of Colorado in Boulder, where he graduated with a Bachelor of Science degree in Aerospace Engineering in May 2006. He was commissioned through AFROTC Detachment 105 where he was recognized as a Distinguished Graduate.

In July 2006 he was assigned to the Air Force SEEK EAGLE Office (AFSEO) at Eglin AFB, FL. There he spent two and a half years as a Store Separation Engineer, performing aircraft-store compatibility analysis primarily on the F-15A/B/C/D and F-15E. While at AFSEO he also spent six months as the Executive Officer to the Commander.

In August 2009 he entered the Graduate School of Engineering and Management at the Air Force Institute of Technology. Upon graduation he will be assigned to the United States Air Force Academy, where he will serve as an instructor in the Department of Aeronautics.

# REPORT DOCUMENTATION PAGE

*Form Approved  
OMB No. 0704-0188*

The public reporting burden for this collection of information is estimated to average 1 hour per response, including the time for reviewing instructions, searching existing data sources, gathering and maintaining the data needed, and completing and reviewing the collection of information. Send comments regarding this burden estimate or any other aspect of this collection of information, including suggestions for reducing this burden to Department of Defense, Washington Headquarters Services, Directorate for Information Operations and Reports (0704-0188), 1215 Jefferson Davis Highway, Suite 1204, Arlington, VA 22202-4302. Respondents should be aware that notwithstanding any other provision of law, no person shall be subject to any penalty for failing to comply with a collection of information if it does not display a currently valid OMB control number. PLEASE DO NOT RETURN YOUR FORM TO THE ABOVE ADDRESS.

|  |                     |   |
|--|---------------------|---|
| 1. REPORT DATE (DD-MM-YYYY)  | 2. REPORT TYPE      | 3. DATES COVERED (From — To)                  |
| 24-03-2011   | Master's Thesis     | Aug 2009 — Mar 2011                           |
| 4. TITLE AND SUBTITLE  |                     | 5a. CONTRACT NUMBER                           |
| An Investigation of Cavity Resonance and its Relationship to Store Force and Moment Loading  |                     | 5b. GRANT NUMBER                              |
|  |                     | 5c. PROGRAM ELEMENT NUMBER                    |
|  |                     | 5d. PROJECT NUMBER                            |
|  |                     | 5e. TASK NUMBER                               |
|  |                     | 5f. WORK UNIT NUMBER                          |
| 7. PERFORMING ORGANIZATION NAME(S) AND ADDRESS(ES)   |                     |   |
| Air Force Institute of Technology<br>Graduate School of Engineering and Management (AFIT/EN)<br>2950 Hobson Way<br>Wright-Patterson AFB, OH 45433-7765   |                     |   |
| 8. PERFORMING ORGANIZATION REPORT NUMBER   |                     |   |
| AFIT/GAE/ENY/11-M05  |                     |   |
| 9. SPONSORING / MONITORING AGENCY NAME(S) AND ADDRESS(ES)  |                     |   |
| Air Force SEEK EAGLE Office<br>205 West D Ave Bldg 350<br>Eglin AFB, FL 32452<br>POC: Capt Darrell Crowe<br>COMM: (850)882-4694<br>E-MAIL: darrell.crowe@eglin.af.mil  |                     |   |
| 10. SPONSOR/MONITOR'S ACRONYM(S)   |                     |   |
| AFSEO  |                     |   |
| 11. SPONSOR/MONITOR'S REPORT NUMBER(S)   |                     |   |
| 12. DISTRIBUTION / AVAILABILITY STATEMENT  |                     |   |
| APPROVED FOR PUBLIC RELEASE; DISTRIBUTION IS UNLIMITED.  |                     |   |
| 13. SUPPLEMENTARY NOTES  |                     |   |
| This material is declared a work of the U.S. Government and is not subject to copyright protection in the United States.   |                     |   |
| 14. ABSTRACT   |                     |   |
| A store which is released from an internal bay is subjected to a highly unsteady flowfield which influences the release characteristics for the store. Pressure transducer information is often used to estimate store loading, although no direct correlation between the observed frequencies from the pressure transducers and the store loading has been developed. The relationship between the acoustic modes present in the cavity and the force and moment loading on a store released from a bay are investigated through a CFD study using the OVERFLOW 2.1 solver. The acoustic modes of the cavity are calculated from the pressure fluctuation histories along the cavity ceiling and walls. Empty cavity solutions are compared to the frequencies predicted by the Rossiter equation and to experimental data from the WICS database. Additionally, the cavity pressure fluctuation spectra are compared to the force and moment loading spectra for a store located in the cavity in both the carriage position and the shear layer. It is determined that the presence of a store in the cavity does not alter the fundamental acoustic modes in the cavity. Also, the store force and moment loadings are observed to correlate with the cavity pressure fluctuations. |                     |   |
| 15. SUBJECT TERMS  |                     |   |
| Computational Fluid Dynamics, Cavity Flow, Store Separation, Acoustic Resonance  |                     |   |
| 16. SECURITY CLASSIFICATION OF:  |                     | 17. LIMITATION OF ABSTRACT                    |
| a. REPORT  | b. ABSTRACT         | c. THIS PAGE                                  |
| U  | U                   | U   |
| UU   | 18. NUMBER OF PAGES | 19a. NAME OF RESPONSIBLE PERSON               |
| 125  |                     | Andrew Lofthouse, Maj, USAF (ENY)             |
|  |                     | 19b. TELEPHONE NUMBER (include area code)     |
|  |                     | (937)255-3636x4537; andrew.lofthouse@afit.edu |